

## Table of Contents

List of Figures	iv
1 Introduction	1
1.1 Outline of Thesis	3
1.2 Evidence for Dark Matter	4
1.2.1 Galactic Rotation Curves	5
1.2.2 BBN	7
1.2.3 CMB	8
1.2.4 BAO	11
1.2.5 Gravitational Lensing	13
1.3 Dark Matter Candidates	14
1.3.1 AXIONS	15
1.3.2 WIMPs	17
1.4 WIMP Dark Matter Searches	19
1.4.1 Direct Detection	21
1.4.2 WIMP Detection Experiments	26
List of Abbreviations	1
2 The LUX Detector	28
2.1 Introduction	28
2.2 The LUX TPC	29
2.2.1 Target Xenon	31
2.2.2 Background Rejection	32
2.2.3 The Drift Field inside the LUX TPC	35
2.3 Light and Charge Signals in Liquid Xenon	37
2.3.1 Electronic Recoils (ER)	38
2.3.2 Nuclear Recoils (NR)	40
2.3.3 Energy and Position Reconstruction	41
2.4 Identifying S1, S2	42
2.5 LUX Science Result (WIMP limit)	46

3	Spacial Dependent Correction of the S1 and S2 Signals	53
3.1	$^{83m}\text{Kr}$ Calibration . . . . .	53
3.2	S2 Electron Lifetime and x,y Correction . . . . .	57
3.3	S1 x,y,z Correction . . . . .	60
3.4	Application to x,y,z Corrections in Data Processing . . . . .	64
4	Energy Scale Calibration	67
4.1	Calibrating the Combined Energy Scale . . . . .	67
4.1.1	Anti-Correlation Space . . . . .	69
4.1.2	Refitting in Combined Energy Space . . . . .	71
4.1.3	Finding Errors with MCMC . . . . .	76
4.1.4	Combined Energy Space . . . . .	78
4.1.5	Light Collection and Electron extraction . . . . .	78
4.2	Modeling Intrinsic Detector Resolution . . . . .	80
4.3	Measuring Recombination Fluctuations . . . . .	85
4.3.1	Measuring Recombination Fluctuations with Mono-Energetic Sources . . . . .	85
4.3.2	Results with Mono Energetic Calibration Sources . . . . .	89
4.3.3	Measuring Recombination Fluctuations in Desecrate Energy Bins . . . . .	91
4.3.4	Measuring the Fano Factor in Bins of Energy . . . . .	96
4.3.5	Application to $^{83}\text{Kr}$ . . . . .	97
4.3.6	Application to Tritium Data (any continuus spectrum) . . . . .	100
4.3.7	Centriod Subtraction . . . . .	102
4.4	Correcting the Tritium Spectral Shape for Finite Resolution . . . . .	107
4.4.1	Calculating the Observed Energy . . . . .	109
4.4.2	Smearing a Toy Spectrum . . . . .	111
4.5	Measuring LY, QY and Recombination, Uncorrected for Spectral shape	113
4.5.1	Tritium S1 Mean and NEST . . . . .	113
4.5.2	Tritium S2 Mean and NEST . . . . .	114
4.5.3	Tritium Energy Spectrum . . . . .	116
4.5.4	LY, QY, $\sigma R$ Result . . . . .	120
4.6	Measuring LY, QY, Recombination, Corrected for Spectral shape . . . . .	122
4.6.1	Tritium S1 Correction . . . . .	124
4.6.2	Tritium S2 Correction . . . . .	124
4.7	Thresholds . . . . .	126
4.8	Ionization and Scintillation Yield and Recombination After Correction	127
4.9	The Standard Candle. Light Yield from $^{83m}\text{Kr}$ . . . . .	129
4.9.1	Field dependence of light yield from the 32.1 keV gamma of $^{83m}\text{Kr}$ . . . . .	132
	Bibliography	133

## List of Figures

1.1	Kepler explains the elliptical orbit of Mars, held fixed by a resident angel guiding its orbit. . . . .	2
1.2	$\Lambda$ CDM parameters depicted on a unicorn by the LUX detector. The magic component which comprise the horn has yet to be directly detected, however it provides the backbone for the model. Note, the parameters in the diagram may not be representative of the specific universe in which this thesis is published. . . . .	3
1.3	Measured rotational velocities vs. radius in the Milky Way galaxy. The velocity distribution is consistent with a halo of mass surrounding the galaxy well beyond the observed luminous disk [1]. . . . .	6
1.4	Maru the cat explains the cosmic microwave background. Consider that Maru is a photon and the box size represents local energy densities of the universe. The scale of the the box size is inversely proportional to the local energy density and temperature. At the time of last scatter all boxes containing Marus cease to exist, to the horror of the cats! The Marus are now left to propagate freely through the universe, with their configurations unchanged (the cats are too lazy to move and are content napping for 13.7 billion years). Figures a-d show Maru the cat contained within increasing box sizes corresponding to decreasing energy densities. . . . .	10
1.5	Improvement of resolution from COBE, first to discover anisotropies in the CMB, to WMAP and Planck which have set stringent limits on cosmological parameters by mapping variations in temperature of 1 part in 100,000. Image credit: NASA/JPL-Caltech/ESA. . . . .	11
1.6	BAO peak obtained from BOSS [2] . . . . .	12
1.7	The concentration of mass in the bullet-cluster as observed from X-rays, emitted by baryonic matter, in pink and the concentration of mass from gravitational lensing in blue. [Composite image credit: X-ray: NASA/CXC/CfA/M.Markevitch et al.; Optical: NASA/STScI; Magellan/U.Arizona/D.Clowe et al.; Lensing Map: NASA/STScI; ESO WFI; Magellan/U.Arizona/D.Clowe et al.] . . . . .	14

1.8	Illustration of the CP problem and the axion solution. “Analogy for the CP problem and the axion solution. In a room (the Standard Model), there is a table (QCD) sitting on an uneven floor (CP). A billiard ball (nEDM) placed on top of the table is expected to rapidly move across the uneven surface. However, the billiard ball is observed to stand still and the horizontal angle of the table is measured to be $\theta < 10^{-11}$ . The solution to this puzzling observation is the existence a new degree of freedom (manifested in the axion) that levels the table (drives $\theta = 0$ )”, [Carlos’ Thesis] . . . . .	17
1.9	Methods for detecting WIMPs from interactions of q, standard model particles, and dark matter particles $\chi$ . WIMPs can be detected through the annihilation of dark matter particles into standard model particles, $\chi\chi \rightarrow qq$ . WIMPs can be produced by colliding standard model particles, $qq \rightarrow \chi\chi$ . Or one can look for the scatter of a dark matter particle off a standard model particle, $\chi q \rightarrow \chi q$ . . . . .	20
1.10	Dark matter density vs. distance from the galactic center, calculated from galactic rotation curves of the Milky Way galaxy. The Earth is located at 8.3 kpc. Figure from [1]. . . . .	22
1.11	Plot of WIMP event rate per kg/day/keV vs. Nuclear recoil energy (keV) for several target nuclei, using parameters from [3]. At low detection threshold xenon is the most attractive target nuclei. The drop off in the xenon spectral shape is due to decoherence described by the Helm factor [4]. . . . .	25
2.1	Photo of the outer vessel of the LUX detector from inside the water tank. . . . .	29
2.2	Illustration of the LUX detector’s internals. The detector contains two arrays of PMTs on the top and bottom housing 61 PMTs each. Teflon panels on the edges of the active region are used to reflect scintillation signals. The vertical distance between the two PMT arrays is 60 cm, and the diameter to the outer edge of the teflon panels is 50 cm. . . . .	30
2.3	Simulation of expected gamma background events inside the LUX detector, using the single scatter cut requirement[5]. There is an additional factor of 1000 background rejection within the fiducial volume where the WIMP search is conducted (inside the black dashed lines) .	33
2.4	The ER type and NR type bands from a) AmBe and $^{252}\text{Cf}$ (Red) and b) tritium calibration (Blue). The band means are solid lines and the 10-90% CL are shown as dashed lines. The ER to NR discrimination by using the charge to light ratio was measured to $99.6 \pm 0.1$ % at 50% NR acceptance. . . . .	35

2.5	Field grids in the LUX detector during the 2013 science run. T,A,G,C,B are biassed to -1,+3.5,-1.5,-10,-2 (all in kV), respectively. The PMTs are biased to -1.2 kV on average. The figure on the right shows the electric field model in the drift region between the cathode and gate for drift distance z vs. detector radius r. On average the drift field is 170 V/cm with variation from 140 V/cm to 200 V/cm from cathode to gate. Electric field model from [6]. . . . .	36
2.6	An electronic recoil (ER) event in xenon. The energy deposited is converted primarily to ionization and roughly one tenth for excitation. Only several percent is lost to heat. Xenon excitons and recombining electron ion pairs for xenon dimers which de-excite producing very ultra violet (VUV) scintillation light at 175nm producing the primary scintillation signal (S1). Electrons that do not recombine are drifted by an electric field into the gas phase where they are accelerated producing the secondary scintillation (S2) signal. . . . .	39
2.7	A nuclear recoil (NR) event in xenon. The energy deposited goes mainly towards heat (phonons), the remaining energy is split evenly between ionization and excitation. Xenon excitons and recombining electron ion pairs for xenon dimers which de-excite producing very ultra violet (VUV) scintillation light at 175nm producing the primary scintillation signal (S1). Electrons that do not recombine are drifted by an electric field into the gas phase where they are accelerated producing the secondary scintillation (S2) signal. . . . .	40
2.8	Event diagram. . . . .	42
2.9	2keV ER event as seen by each PMT channel of the LUX detector. The S1 signal summed across all channels is overlaid on the top left, and the S2 signal summed across all channels is overlaid on the top right. . . . .	43
2.10	Density plot of prompt fraction vs. Pulse Area. Top: $^{83m}\text{Kr}$ data set. Bottom: Tritium data set. Populations of single electrons, single photons and the S1 S2 pairs associated with $\gamma$ , $\beta$ and $\alpha$ are highlighted as rectangles. . . . .	45
2.11	All single scatter events seen in the active region of the LUX detector over the course of the first science run passing all cuts listed in table 2.3 excluding the fiducial cut. The dashed cyan box indicates the fiducial volume. . . . .	47
2.12	The remaining events passing the quality cuts listed in table 2.3. The charge to light ratio (S2/S1) is plotted vs. S1 (proportional to energy) to show the separation of ER and NR type events. The 10-90% CF limits of the ER and NR band are plotted as the dashed blue and red curves, respectively. The band means are solid. S2 <sub>b</sub> stands for the S2 signal on the bottom PMT array. . . . .	49

2.13 LUX detector is consistent with a P value of 0.35 of the background only hypothesis. The 90% upper C.L. cross section for various spin independent masses are shown in figure 2.13 in blue. Also shows are limits from Xenon100 (red), CDMS II (green), ZEPLIN III (magenta), and one sigma signal claimed for DAMA/LIBRA (shaded grey), CDMS II Silicone (shaded green), CRESST II (shaded yellow).	51
3.1 A simplified decay diagram of $^{83}\text{Rb}$ and $^{83\text{m}}\text{Kr}$ , from [7]. . . . .	54
3.2 The S1 and S2 of two $^{83\text{m}}\text{Kr}$ events. Top Figures (a): Show a $^{83\text{m}}\text{Kr}$ event in which the two x-rays have overlapped within 60 ns, the S2 arrives about 93 $\mu\text{s}$ later. Bottom Figures (b): Show a $^{83\text{m}}\text{Kr}$ event in which the two x-rays have overlapped within 220 ns, the S2 arrives about 205 $\mu\text{s}$ later. The LUX pulse finder classifies events within a 1 $\mu\text{s}$ window as a single S1. The S2 pulses are insensitive to the timing separation of the dual decay as electron diffusion smears the pulses two together as the electrons drift. . . . .	55
3.3 Distribution of $^{83\text{m}}\text{Kr}$ events 10 minutes after the injection. The source readily mixed uniformly throughout the liquid xenon illuminating all regions of the active volume. The solid black lines represent the fiducial volume used for the WIMP search. . . . .	56
3.4 Left: Fits to the mean of $S_{2b}$ in several z slices. Right, the exponential fit to the means of $S_{2b}$ vs. drift time used to extract electron lifetime $\lambda$ . . . . .	58
3.5 Left: Response of $S_{2b}$ vs. x,y normalized to the response at the center ( $x=y=0$ ). Right: Response of $S_{2b}$ vs. x,y after flat fielding the data using $\mathcal{N}\mathcal{F}_{S_{2b}}$ . . . . .	59
3.6 Improvement of resolution in $S_{2b}$ after applying the z and x,y,z correction. . . . .	60
3.7 S1 x,y,z response normalized to the center of the detector. The interpolated map represents the inverse of the normalization factor $\mathcal{N}\mathcal{F}$ . . . . .	62
3.8 S1 x,y,z response normalized to the center of each z slice. There are greater variations near the very top and bottom 4 z slices as the solid angle for light hitting the PMT arrays are increased. For the central slices the x,y response is uniform due to increased scattering off the teflon panels. . . . .	63
3.9 S1 x,y,z response normalized to the center of the detector after the data has been flat fielded and normalized to the detector center. The remaining fluctuations in the fiducial volumes ( $r < 18\text{cm}$ ) are less than 1%, near the top and bottom edges the deviation increases to as much as 3% due to the interpolation of the correction breaking down. . . . .	64
3.10 Improvement of resolution in S1 after applying the z and x,y,z correction. . . . .	65
3.11 Electron lifetime measured using $^{83\text{m}}\text{Kr}$ calibrations over the course of the LUX science run in 2013. . . . .	66

3.12	Measured response of to light from $^{83m}\text{Kr}$ calibrations at the center of the LUX detector over the corse of the LUX science run in 2013. . . . .	66
4.1	LUX data in anti correlation space (S1 vs. S2), the black lines indicate the initial cuts by eye used to isolate populations of constant energy. In both figures diagonals represent lines of constant energy with a slope depending on the local recombination probability. The centroids found by an unbind maximum likelihood analysis are shows as a black X, for sources show in table 4.1. . . . .	71
4.2	Doke plot showing the best fit for the energy calibration parameters g1 and g2 using S1 and S2 means extracted from anti-correlation space. The first three blue points, from the left, are from $^{83}\text{Kr}$ calibrations at 50, 105 and 180 V/cm respectively. The open circle was from the K-shell xenon X-ray and was not used for the fit as it's absolute energy and origin from the skin of the detector is uncertain. . . . .	72
4.3	Doke plot showing the best fit for the energy calibration parameters g1 and g2 using S1 and S2 extracted from a combined energy space. The first three blue points, from the left, are from $^{83}\text{Kr}$ calibrations at 50, 105 and 180 V/cm respectively. The open circle was from the K-shell xenon X-ray and was not used for the fit as it's absolute energy and origin from the skin of the detector is uncertain. . . . .	73
4.4	S1 fits to sources at nominal field of 180 [V/cm] unless otherwise noted. Source and energy in keV from top left to bottom right: a) $^{131}\text{Xe}$ : 163, b) $^{127}\text{Xe}$ : 207, c) $^{127}\text{Xe} \& ^{129m}\text{Xe}$ : 236.8, d) $^{127}\text{Xe}$ : 410, e) $^{214}\text{Bi}$ : 609, f) $^{137}\text{Cs}$ : 661.6, g) $^{83m}\text{Kr}$ : 41.5 - at 50 [V/cm], h) $^{83m}\text{Kr}$ 41.5 - at 105 [V/cm], i) $^{83m}\text{Kr}$ 41.5 . . . . .	74
4.5	S2 fits to sources at nominal field of 180 [V/cm] unless otherwise noted. Source and energy in keV from top left to bottom right: a) $^{131}\text{Xe}$ : 163, b) $^{127}\text{Xe}$ : 207, c) $^{127}\text{Xe} \& ^{129m}\text{Xe}$ : 236.8, d) $^{127}\text{Xe}$ : 410, e) $^{214}\text{Bi}$ : 609, f) $^{137}\text{Cs}$ : 661.6, g) $^{83m}\text{Kr}$ : 41.5 - at 50 [V/cm], h) $^{83m}\text{Kr}$ 41.5 - at 105 [V/cm], i) $^{83m}\text{Kr}$ 41.5 . . . . .	75
4.6	Doke plot of the data showing the light yield vs. charge yield. Only solid circles are used for the fit, the open circle is the Xe K shell X-ray from the detector edge. . . . .	76
4.7	MCMC for the linear fit to the Doke plot. There is a strong negative correlation between the slope m and intercept b which results from the degeneracy between gains g1 and g2. . . . .	77
4.8	Combined energy scale. a) The xenon activation lines from early in the run. b) $^{137}\text{Cs}$ calibration data. c) All calibration data including the $^{83m}\text{Kr}$ calibration. d) Xenon X-ray. . . . .	79

4.9	Single electron distribution as seen by the bottom PMT array fitted with a skew Gaussian model to account for the underling Poisson statistics of observing between 9 and 10 photo electrons (PE) for each electron leaving the liquid and entering to the gas phase at a higher field causing electro-luminescence. The $\mu$ of the fit represents the true mean of the skew Gaussian distribution. . . . .	81
4.10	Populations of calibration sources in discrimination space $\log\left(\frac{n_e}{n_\gamma}\right)$ vs. combined energy [keV <sub>ee</sub> ]. The ovals represent the combination of $\sigma R$ , $\sigma n_{\gamma_{\text{Det}}}$ , $\sigma n_{e_{\text{Det}}}$ in black, white, red respectively. . . . .	90
4.11	Measured values of $\sigma R$ , $\sigma n_{\gamma_{\text{Det}}}$ , $\sigma n_{e_{\text{Det}}}$ vs. Energy on the left and vs. Quanta on the right. Measured using sources listed in Table 4.1. . . . .	90
4.12	Top: Illustration of statistical variance, recombination fluctuations are set to 0. The spread in number of photons moves vertically and the spread in number of electrons moves horizontally. In black, a line of constant energy along the mean of combined energy with a width $\Delta E$ . Bottom left: Dominated by recombination fluctuations which move 45° to statistical variances. Bottom Right: Typical values for recombination and S1, S2 Stat for Kr <sup>83</sup> . . . . .	93
4.13	Illustration of statistical variance for the tritium beta spectrum, recombination fluctuations are set to 0. This plot is analogous to Figure 4.12 which illustrates the case for the mono energetic <sup>83m</sup> Kr decay. Recombination fluctuation move along lines of constant energy, S1 statistical fluctuation move vertically and S2 statistical fluctuations move horizontally. . . . .	103
4.14	Light yield (left) and Charge yield (right) of a simulated tritium spectrum, with the fit to the centroid show in black. The variance in number of photon and electrons per energy bin is used to extract recombination fluctuations. . . . .	104
4.15	Simulated tritium spectrum with the detector resolution of the LUX detector, $\sigma_{S1_{\text{Det}}}$ and $\sigma_{S2_{\text{Det}}}$ , and an arbitrary recombination fluctuation $\sigma R$ (magenta). After centroid subtraction we apply the methodology described in the previous section to extract $\sigma R$ (black and blue) through the light and charge channel using our knowledge of detector resolution per each energy bin $\chi_{\text{Det}}$ (green), $S1_{\text{Det}}$ (red) and $S2_{\text{Det}}$ (yellow). The plots show cases for various bin widths in [KeV]: a) $\Delta E = 0.1$ b) $\Delta E = 0.25$ c) $\Delta E = 0.5$ d) $\Delta E = 1$ . . . . .	106
4.16	. . . . .	108

4.17 Top Left: A linearly decaying spectrum, in blue. The black curve represents the sum of the Gaussians assuming a constant resolution. Top Right: A linearly decaying spectrum, in blue. The black curve represents the sum of the Gaussians with a $\sqrt{E}$ dependent resolution. Bottom: The observed mean, with finite resolution, compared to the real mean with infinite resolution. The black points are for the case with linear resolution and the red points represent the case with $\sqrt{E}$ dependent resolution. . . . .	112
4.18 Left: In Black S1 tritium spectrum extracted from the data. In blue, The NEST light yield curve. In red, the NEST light yield curve with recombination fluctuations. Dashed magenta is NEST light yield with smearing from equations 4.40. Right: The ratio of the real mean to the observed mean vs. the observed mean for a tritium photon spectrum. Note the S1 threshold at about 3 Phe in S1. . . . .	115
4.19 Left: In Black S2 tritium spectrum extracted from the data. In blue, The NEST light yield curve. In red, the NEST light yield curve with recombination fluctuations. Dashed magenta is NEST light yield with smearing from equations 4.41. Right: The ratio of the real mean to the observed mean vs. the observed mean for a tritium photon spectrum. Note the S2 threshold at about 400 Phe in S2. . . . .	117
4.20 The tritium energy spectrum reconstructed from the data using both Pulse Area and Spike count for S1. Along with LUX SIM, the true tritium beta spectrum and a tritium spectrum smeared with detector resolution. . . . .	119
4.21 Left, mapping from real Monte Carlo energy to observed energy after applying a finite resolution using LUXSIM. Right, comparing the correction determined from the Monte Carlo (Red) to the detector smearing model (black) given in equation 4.47. The dashed lines represent the uncertainty in the measured value of $F(E)$ . The agreement is within errors from 1 to 18 keVee. The Energy threshold is near 1.0 keV <sub>ee</sub> . . . . .	119
4.22 Number of photons (left) and electrons (right) vs. energy from tritium data without spectral shape correction. The spread in quanta per energy bin is used to measure recombination fluctuations. . . . .	121
4.23 Top: Extracted recombination fluctuation from the tritium data from fluctuations in photons and electrons (Black and Red receptively). Bottom right: mean number of quanta in photons, electrons, ions, exitons vs. energy [keV] for the tritium calibrations. Bottom left: Recombination fraction and the one sigma (shaded) vs. energy [keV].	122
4.24 Light yield and charge yield from tritium data without spectral shape correction at 180 [V/cm] in black, the shaded region represents the one sigma uncertainty on g1 and g2. The NEST yield prediction and it's corresponding 1 sigma is shaded in blue. NEST interpolation in show in magenta to energies where the model is not vetted. . . . .	123

4.25 Left: In Black, tritium data. In red, the spectrum after applying measured recombination fluctuations. In dashed blue is after applying recombination and finite detector resolution of equation. Left: Mapping of the observed mean, with finite resolution, to the mean with infinite resolution for a tritium photon spectrum. Bottom Right: The ratio of the real mean to the observed mean vs. the observed mean for a tritium photon spectrum. Note the S1 threshold at about 3 Phe in S1. . . . .	125
4.26 Left: In Black, tritium data. In red, the spectrum after applying measured recombination fluctuations. In dashed blue is after applying recombination and finite detector resolution of equation. Left: Mapping of the observed mean, with finite resolution, to the mean with infinite resolution for a tritium photon spectrum. Bottom Right: The ratio of the real mean to the observed mean vs. the observed mean for a tritium photon spectrum. Note the S2 threshold at about 400 Phe. . . . .	126
4.27 Threshold calculated from difference of simulated Tritium S1, S2 and energy spectra. a) S1 b) S2 <sub>b</sub> , c) E . . . . .	127
4.28 After spectral shape correction. Top: Extracted recombination fluctuation from the tritium data from fluctuations in photons and electrons (Black and Red receptively). Bottom right: mean number of quanta in photons, electrons, ions, exitons vs. energy [keV] for the tritium calibrations. Bottom left: Recombination fraction and the one sigma (shaded) vs. energy [keV]. . . . .	128
4.29 Extracting LY and QY from data corrected for spectral shape. . . . .	129
4.30 LY and QY from tritium data corrected for spectral shape along with the 1 sigma band of g1/g2. The blue and magenta curve are NEST extrapolation and interpolation, respectively. . . . .	130
4.31 Left: <sup>83m</sup> Kr peaks at zero field. ** The 9.4 keV peak is fit only for events with a decay time separation greater than 1000 [ns]. Right: shows the timing separation between the 32.1 and 9.4 [keV] decays plotted above. . . . .	131

## Chapter 1: Introduction

A few centuries ago one of the greatest strides in astronomy was made by Kepler working off Tyco Brahe's data in understanding planetary orbits. Kepler discovered that planets move along elliptical orbits with the sun at one of the foci and thus developed the laws of planetary motion, along with the fact that it's useful to share data. In 1609 the concept was revolutionary yet it raised a more interesting question, why do planets move in elliptical orbits? Kepler explanation was that each planet was guided in its elliptical orbit by a resident angel, illustrated in figure 1.1.

Two hundred and fifty years later, another significant discovery was made on the nature of light by James Maxwell. Apparently, the light from mars shining into Tyco Brahe's eye (unaided by a telescope) had propagated through space as an electro magnetic wave. The propagation of light through a vacuum would require electric fields without the presence of charge, thus it was proposed that the universe is filled with aether through which electromagnetic waves could propagate.

Fast forward to the era of the standard model, and precision cosmology . The standard model provides as a nearly perfect framework to understand the interactions of particles we know of. Precision cosmological measurements are now constraining parameters deemed impossible several decades ago (Plank is a huge

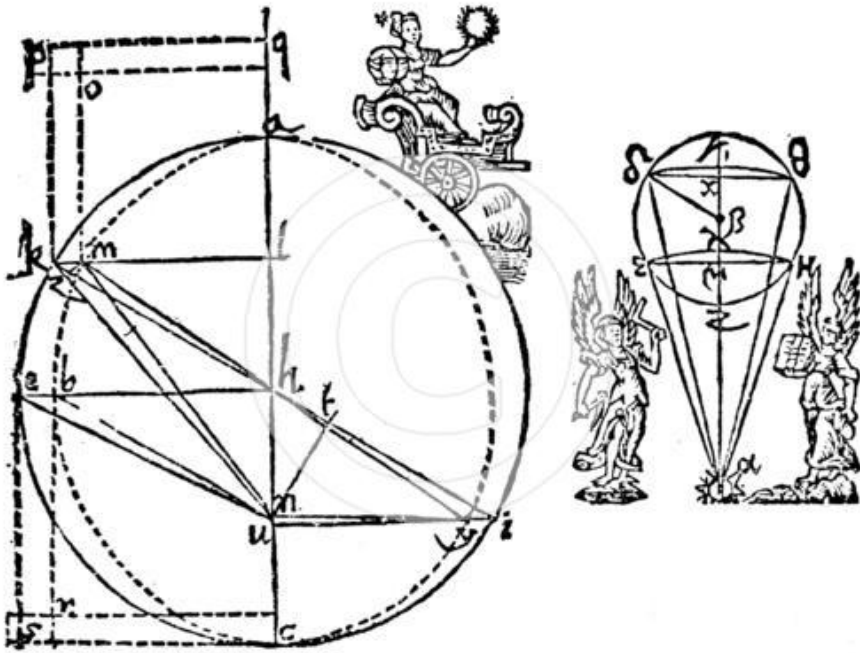


Figure 1.1: Kepler explains the elliptical orbit of Mars, held fixed by a resident angel guiding its orbit.

step up from Tyco’s eye ball). These measurements have provided the basis for the concordance cosmological model ( $\Lambda$ CDM). Apart from knowing that planets move in elliptical orbits we also know that the universe is primarily composed of dark energy (69.2%) and dark matter (25.8%). Ordinary particles described by the standard model which compose our current understanding of ‘everything’ only constitute 4.82% of the universe. See figure 1.2 for a diagram of the concordance cosmological model.



Figure 1.2:  $\Lambda$ CDM parameters depicted on a unicorn by the LUX detector. The magic component which comprise the horn has yet to be directly detected, however it provides the backbone for the model. Note, the parameters in the diagram may not be representative of the specific universe in which this thesis is published.

## 1.1 Outline of Thesis

In this section we review current cosmological evidence for the existence of dark matter, and give an overview of dark matter candidates along with the WIMP model. We also review if WIMPs exist and how they could be detected and the scattering off a nuclei would look.

In Chap. 2, We overview the LUX detector, a liquid xenon time projection

chamber (TPC), and how it searches for WIMPs. We conclude the chapter with the most recent LUX science results which holds the worlds leading limit for spin independent WIMP nucleon scattering cross section.

In Chap. 3, the position dependent corrections of energy deposition in the LUX detector are discussed.

In Chap. 4, the absolute energy scale calibration of the LUX detector is discussed.

Chapter 5 ... (more to come) provides the conclusion to the thesis.

## 1.2 Evidence for Dark Matter

Astronomical observations hinting at the existence of dark matter were first observed in 1932 by Oort [8] and more precisely in 1937 by Zwicky [9]. Both noted discrepancies in galactic mass measurements when comparing the luminous mass to the required to support galactic rotational velocities measured by red shifts. Oort had noted up to a factor of ten more mass than luminous mass in the Sombrero Galaxy and Zwicky found a factor of 500 for the Coma cluster. Both the observations were far to large to be accounted for by light absorption, indicating the existence of dark matter to account for the missing mass. Since then more evidence for the existence of dark matter has been compiled, including big bang nucleosynthesis (BBN), anisotropies in the cosmic microwave background (CMB), baryonic acoustic oscillations (BAO), formation of large structures, galactic ration curves, and gravitational lensing. All independent techniques leading to a unified conclusion for the existence

of non baryonic and non luminous matter. Individually some pieces of evidence, such as galactic rotation curves, can be explained by modifications to general relativity (GR), but not all simultaneously. The existence of non relativistic, dark matter particles are required in order to unify the current observations. This dark matter does not couple to the electromagnetic force and is thus able to avoid our standard detection techniques, making its presence felt on large scales via gravity. In the last thirty years significant progress has been made in the direct detection of such a particle, the forefront of which will be presented in this thesis.

### 1.2.1 Galactic Rotation Curves

There are two common methods for measuring the mass of a galaxy or cluster of galaxies. First, one can use the total luminosity and the known distance to the galaxy to determine the luminous mass, that is the mass corresponding to the visible light. Second, the rotational velocities of stars orbiting the galactic center can be mapped and used to determine the mass distribution as a function of galactic radius. Rotational velocities of stars around galactic centers at large distances can be measured with Doppler shift, with more recent measurement relying on the 21 cm H<sub>1</sub> line from hydrogen as the standard candle. The rotational velocities of objects orbiting galaxies are highly non relativistic moving at speeds on the order 100 km/s. At the outer edges of the luminous galactic centers, typically past 5 kpc the velocity distribution is expected to fall off as redacted by Newtonian mechanics  $\sim 1/r$ . Yet observations from as early as 1932 indicate that velocity distributions tend to remain

constant with radius suggesting that the objects are not rotating around the central luminous mass, rather they are rotating inside a solid body of dark matter [8] [9] [10] [1]. The velocity distributions measured for the Milky Way galaxy are show in 1.3.

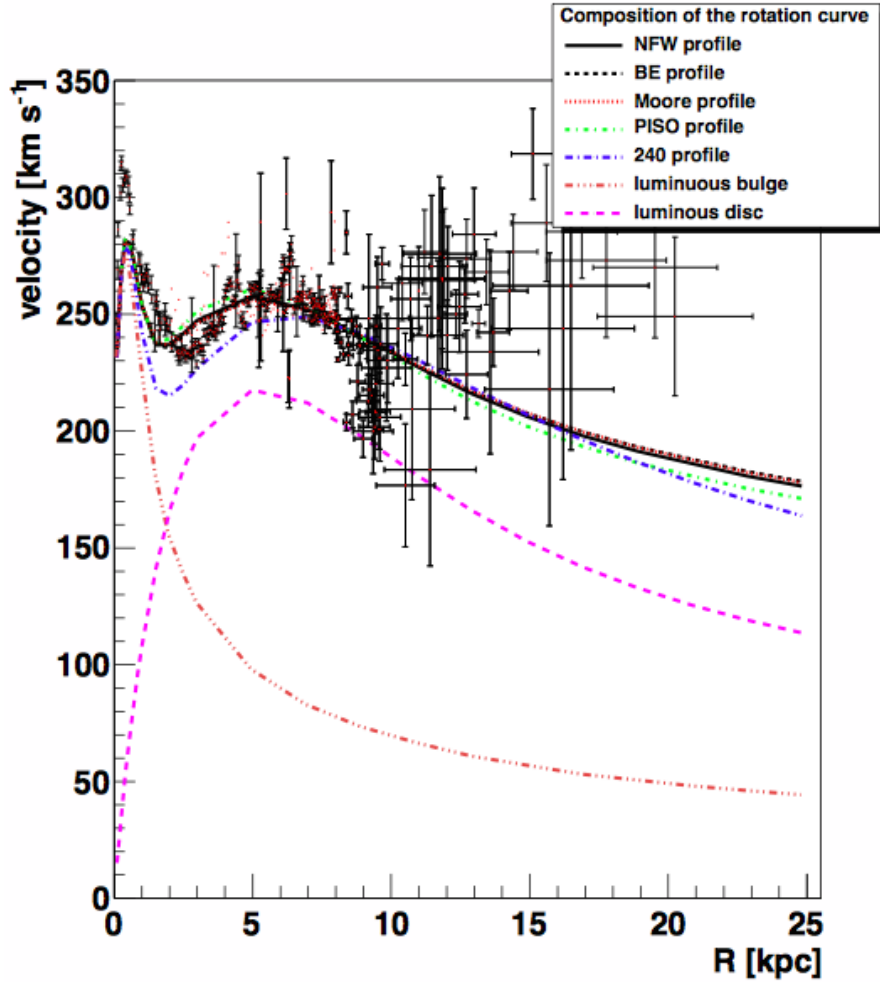


Figure 1.3: Measured rotational velocities vs. radius in the Milky Way galaxy. The velocity distribution is consistent with a halo of mass surrounding the galaxy well beyond the observed luminous disk [1].

### 1.2.2 BBN

Big band nucleosynthesis (BBN) accounts for the relative abundances of light elements in the universe today, including H, D, He<sup>3</sup>, He<sup>4</sup> and Li<sup>7</sup> [11]. BBN took place in a relatively short time window several seconds after the big bang when the universe cooled below 10<sup>11</sup>K (10 MeV) and seized as the temperature cooled below 10<sup>9</sup>K (100 keV). Under the temperature conditions of BBN it was energetically favorable for free protons and neutrons to undergo nuclear fusion and is the only mechanism to produce light elements we see today. The heavier elements were later fused together in stars and ejected upon the star's death into the cosmos. Nuclear cross sections of protons, neutrons and light elements have been measured to high person and can be combined with the expansion rate of the universe to precisely predict the relic abundances of baryonic matter. Observations constrain the abundances of the light elements to be H~ 75%, D~ 25%, He<sup>4</sup> ~ 0.01%, Li<sup>7</sup> ~ 10<sup>-10</sup> %. The ratio of D/H has been used to constrain the relic density of baryonic matter to be  $\Omega_b h^2 = 0.02202 \pm 0.00046$  [12].

$$\Omega_b h^2 = \frac{p_b}{p_c} \quad (1.1)$$

Where h is the Hubble constant H dividend by 100 ( $H_0/100$ ),  $p_b$  is the baryonic density and  $p_c$  is the critical density required for a flat universe (verified by the CMB). We can write the i<sup>th</sup> density component as:

$$\Omega_i \equiv \frac{p_b}{p_c} = \frac{8\pi G \rho_i}{3H^2} \quad (1.2)$$

Where G is the gravitational constant, H is the Hubble constant (found in table 1.1). The baryon density measured using BBN is constrained to within 1% and in agreement with the latest constraints from Plank's CMB data,  $\Omega_b h^2 = 0.02205 \pm 0.00028$  [13].

### 1.2.3 CMB

The early universe consisted of a plasma making the universe opaque to photons as they scattered off free electrons. As the temperature fell below the binding energy of hydrogen 13.6 eV, electrons neutral atoms allowing photons to decouple from the plasma making the universe became transparent. The mean temperature of decoupling was actually at 0.25 eV ( $\sim$ 4000 K) as photons still scatter frequently near the binding energy of hydrogen [11]. The cosmic microwave background (CMB) emanated from this time after making a final scatter photons decoupled from electrons effectively attaining a mean free path on the scale of the universe. The photons from the CMB observed today at the red shift temperature of  $2.72548 \pm 0.00057$  K [14] have not interacted from the time of last scatter 379,000 years after the big bang. The CMB has encoded within it a wealth of information about the universe as it was at the time of decoupling. The concept of the information encoding is illustrated in figure using Maru the cat in various boxes. Consider that Maru is a photon and the box size represents local energy densities of the universe. The smaller boxes represent areas of higher energy density and temperature. At the time of last scatter all boxes containing Marus cease to exist, to the horror of of

the cats. The cats now begging to propagate freely through the universe with their configuration unchanged (the cats are too lazy to move and are content napping while propagating though space). It should be noted, that as the universe expands so will the cats. When the Marus finally reach our telescopes, 13 billion years latter, the shape and squeezing of each Maru informs us of the box size (temperature) from which each Maru has emanated. Using this information from multiple Marus the distribution of box sizes at the time of last scatter can be mapped, reveling areas of slightly larger boxes and areas of slightly smaller boxes. This is roughly the idea behind measuring anisotropies in the cosmic microwave background using microwave telescopes.

.Ever more increasing measurements from COBE, WMAP and Planck have been able to probe slight temperature variations to 1 part in 100,000 as seen in figure 1.5. Table 1.1 shows the constraints on cosmological parameters set by Planck. The results are in good agreement with baryonic density derived from BBN and predict a dark matter component of 25.8%.

Parameter	Value	Definition
$\Omega_b h^2$	$0.2214 \pm 0.00024$	Baryon energy density
$\Omega_c h^2$	$0.1187 \pm 0.0017$	Cold dark matter energy density
$\Omega_m h^2$	$0.1423 \pm 0.0029$ *	Total matter energy density
$\Omega_\Lambda$	$0.692 \pm 0.010$	Dark energy density
$\Omega_K$	$-0.0005 \pm 0.0065$ (95%)	Curvature
$\Sigma_{m_\nu}$	$< 0.230$	Sum of neutrino masses [eV]
$H_0$	$67.77 \pm 0.77$	Hubble Constant [ $\text{km s}^{-1} \text{Mpc}^{-1}$ ]

Table 1.1: Cosmological parameters from Planck+WP+highL+BAO [13]. \* Only Planck.

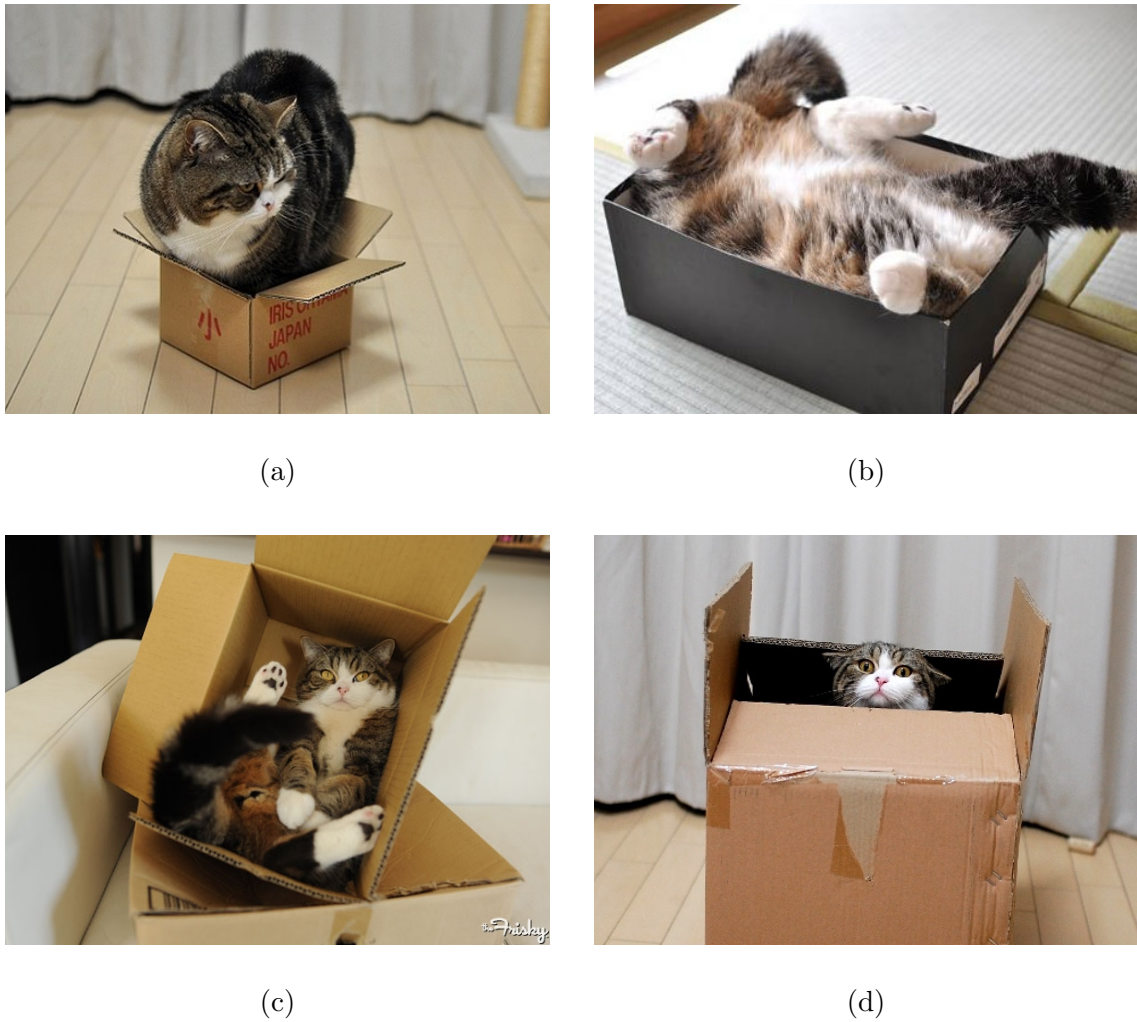


Figure 1.4: Maru the cat explains the cosmic microwave background. Consider that Maru is a photon and the box size represents local energy densities of the universe. The scale of the the box size is inversely proportional to the local energy density and temperature. At the time of last scatter all boxes containing Marus cease to exist, to the horror of the cats! The Marus are now left to propagate freely through the universe, with their configurations unchanged (the cats are too lazy to move and are content napping for 13.7 billion years). Figures a-d show Maru the cat contained within increasing box sizes corresponding to decreasing energy densities.

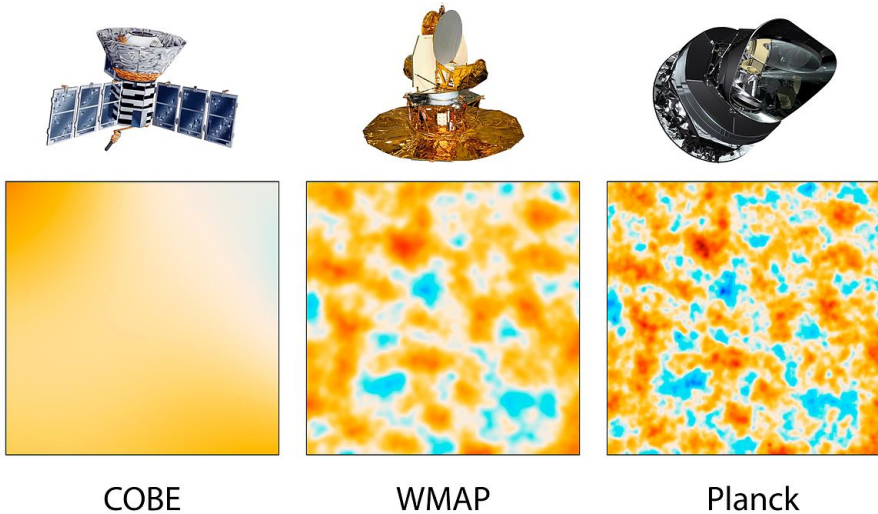


Figure 1.5: Improvement of resolution from COBE, first to discover anisotropies in the CMB, to WMAP and Planck which have set stringent limits on cosmological parameters by mapping variations in temperature of 1 part in 100,000. Image credit: NASA/JPL-Caltech/ESA.

#### 1.2.4 BAO

The universe 379,000 years after the big bang was uniformly distributed, with only small variations observed in the CMB temperature of 1/100,000 [15]. Before decoupling took place gravity pulled baryons and dark matter into high density regions resulting in an opposing outward force from photon pressure. The outward force from the photon pressure was only felt by the baryons whereas the dark matter component would not couple to photons. The competing attractive and repulsive forces gave rise to baryonic acoustic oscillations (BAO) with density regions propagating as spherical sound waves do. The amplitudes of the waves are separated by a characteristic radius called the sound horizon  $r$ , which is sensitive to

the initial dark matter and baryon densities [16]. Anisotropies in the CMB power spectrum probe these oscillations as discussed previously in 1.2.3. At the time of decoupling the photon pressure ceased providing the opposing force allowing the gravitational restoring force to dampen the oscillations. If the picture since the time of the CMB is propagated forward in time we expect that areas of the CMB that were denser would cluster, thus statistically the universe is expected to have large scale structures on the order of the sound horizon  $r$ . Measurements of BAO by the Sloan Digital Sky Survey [17] and BOSS [2] are consistent with the sound horizon expected from anisotropies in the CMB, with a preferred scale of  $100\text{hh}^{-1}$  Mpc ( $\sim 150$  Mpc) between large scale structures. Figure fig:BOSS shows the result from BOSS using Lyman- $\alpha$  absorption in quasar emission spectrum due to the presence of neutral hydrogen in the intergalactic medium [2].

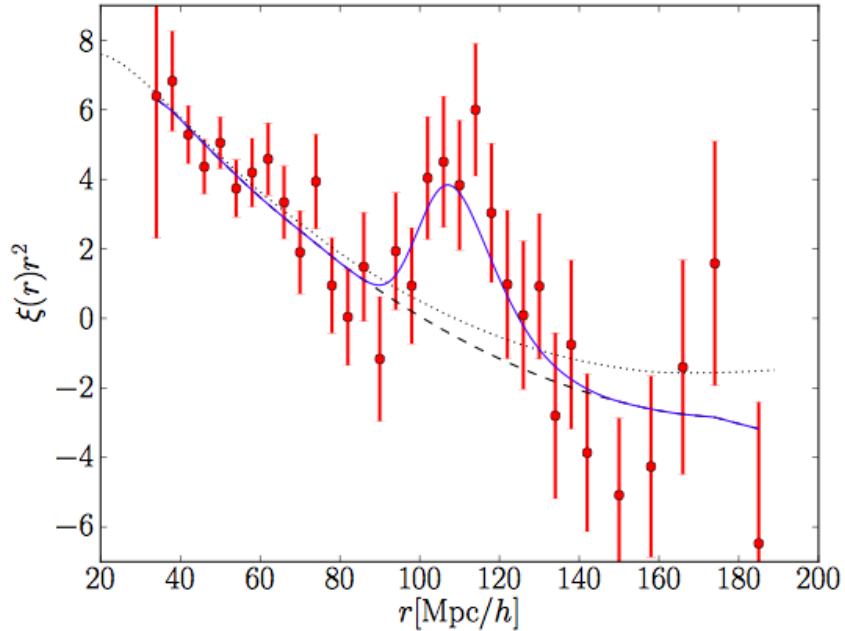


Figure 1.6: BAO peak obtained from BOSS [2]

### 1.2.5 Gravitational Lensing

Gravitational lensing can be used to map the focal points of gravitational mass in a galaxy or cluster. The idea is to look for repeating structures around a large central mass which have been bent around regions of large mass. These repeating structures are caused by light trajectories bending before reaching earth creating an optical illusion, appearing as if the light had emanated from multiple sources along a straight lines of sight. Observations of the Bullet cluster strongly support the existence of dark-matter. The Bullet cluster is made up of two galaxy clusters which have recently collided and passed through each other. The collision has caused the ordinary, baryonic matter to heat and emit X-rays that are observed and used to map the luminous mass distribution [18]. However, the observed concentration of mass is not consistent with the center of mass observed using gravitational lensing via GR [19]. The way light bends around the bullet-cluster would indicate the presence of a dark-matter shell which, unlike the ordinary matter, has passed through at a faster rate due to the lack of interactions. Figure 1.7 shows the concentration of mass in the bullet-cluster as observed from X-rays, emitted by baryonic matter, in pink and the concentration of mass from gravitational lensing in blue. The X-ray mapping from Chandra when compared with gravitational lensing studies of the Bullet cluster clearly demonstrate a decoupling of the dark matter center of mass from the baryonic center of mass induced by the cluster's recent collision.

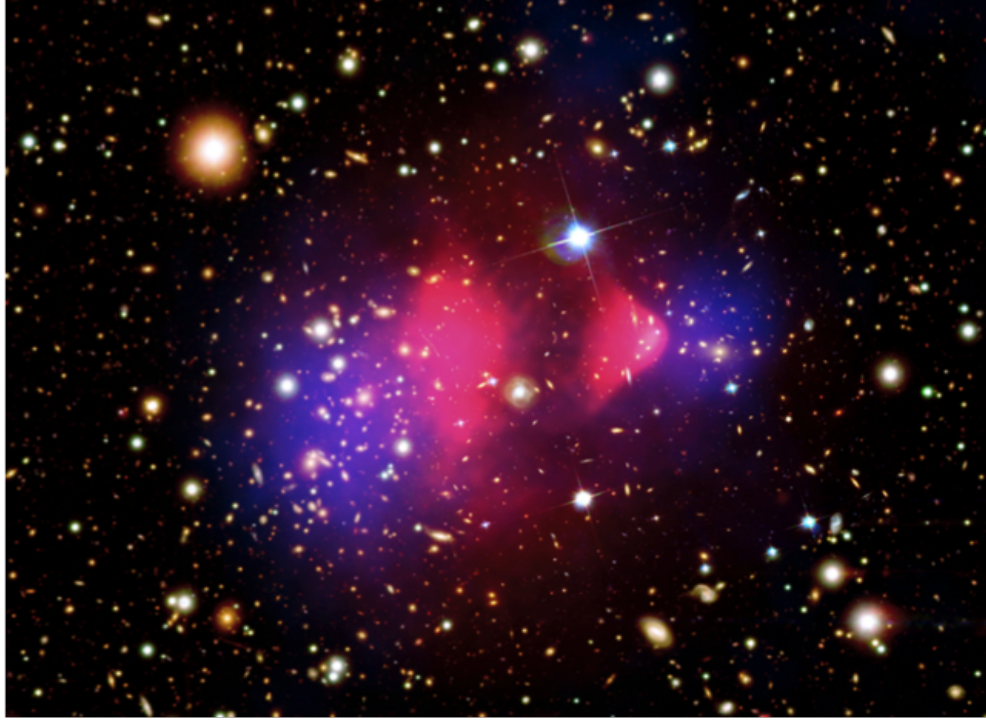


Figure 1.7: The concentration of mass in the bullet-cluster as observed from X-rays, emitted by baryonic matter, in pink and the concentration of mass from gravitational lensing in blue. [Composite image credit: X-ray: NASA/CXC/CfA/M.Markevitch et al.; Optical: NASA/STScI; Magellan/U.Arizona/D.Clowe et al.; Lensing Map: NASA/STScI; ESO WFI; Magellan/U.Arizona/D.Clowe et al.]

### 1.3 Dark Matter Candidates

The evidence for the existence of missing mass outlined in the previous section forces us to examine solutions to account for those cosmological phenomena. It is natural to at first try and solve the anomaly by using our understanding of standard model particles. The first candidate considered for dark matter is the existence of Massive Compact Halo Objects (MACHOs). However, the MACHO theory requires that

the extra mass be baryonic which is refuted by the precision measurements (BBN, CMB) that limit Baryonic mass to only 2.2% while the overall matter energy density required is 31.75% [20] [13] (see table 1.1). A non baryonic candidate drawn from the standard model are neutrinos, which are known to carry mass due to oscillations and only interact weakly [21]. However, large scale structure formation require that the universe have a ‘cold’ (non relativistic) dark matter component in order to become gravitationally bound to galaxies. With current constraints on the neutrinos masses to less than 0.23 eV [13], neutrinos are highly relativistic and would fail to reproduce structuring of the universe observed today [22].

### 1.3.1 AXIONS

“I named them after a laundry detergent, since they clean up a problem with an axial current”

Frank Wilczek

Axions were introduced to solve the strong CP problem. The Lagrangian allowed by gauge symmetry includes a term

$$\mathcal{L} = \Theta \frac{g_s^2}{32\pi^2} G_{\mu\nu}^a \tilde{G}^{\mu\nu a} \quad (1.3)$$

where  $g$  is the gluon QCD coupling constant,  $G_{\mu\nu}^a$  the gluon field strength and  $\Theta$  is a constant [23]. The Lagrangian breaks gauge symmetry which allows for CP violating and is expected to contribute to the electric dipole moment (NEDM). Measurements of the NEDM have been constrained to be much smaller than expected with CP violation. NEDM is constrained to be less than  $2.9 \times 10^{-26}$  e cm (90% CL) [24], resulting in  $\Theta$  of less than  $0.7 \times 10^{-11}$ .

An elegant solution for the lack of observe red electric dipole moment was introduced by Pecci and Quinn. The proposed idea is to promote  $\Theta$  to a dynamical field value through a new symmetry (PQ symmetry) which is spontaneously broken naturally leading to  $\Theta = 0$  by minimizing the potential [25] [26]. Such a solution to the strong CP problem leads to the existence of a light pseudo scalar particle, the Axion. The axion would be a light particle which could couple to the electromagnetic field, in the presence of a strong electromagnetic field,  $a \leftrightarrow \gamma\gamma$  [27].

Searches for axions involve looking for the rare electromagnetic interactions that convert axions into microwaves in resonating cavities with large magnetic fields here on earth. ADMX has been sensitive to mass scales of  $3.3 \mu\text{eV}$  to  $3.59 \mu\text{eV}$  with planned upgrades to explore more parameter space [28]. Coupling of photons to axions could also occur in the strong electromagnetic fields of our own sun. The CAST experiment searches for axions produced in the interior of the sun from thermal photons, with keV energies, which then arrive to the detector where they are converted back into X-rays within a large dipole magnet [27]. The axion solves the strong CP problem and is a potential dark matter candidate, there is still vast parameter space to explore with potential axion massed ranging from  $\mu\text{eV}$  to  $\text{eV}$  scales. Instruments are being upgraded to explore these regions and will require patience, since each potential axion mass requires tuning the cavity to a specific resonance and waiting.

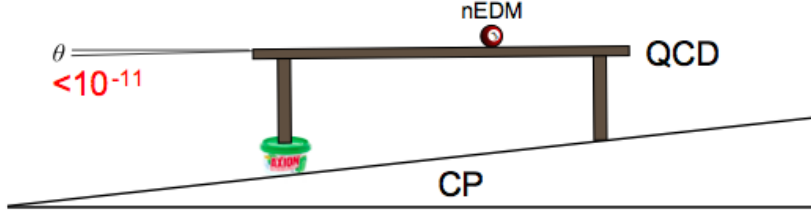


Figure 1.8: Illustration of the CP problem and the axion solution. “Analogy for the CP problem and the axion solution. In a room (the Standard Model), there is a table (QCD) sitting on an uneven floor (CP). A billiard ball (nEDM) placed on top of the table is expected to rapidly move across the uneven surface. However, the billiard ball is observed to stand still and the horizontal angle of the table is measured to be  $\theta < 10^{-11}$ . The solution to this puzzling observation is the existence a new degree of freedom (manifested in the axion) that levels the table (drives  $\theta = 0$ )”, [Carlos’ Thesis]

### 1.3.2 WIMPs

A leading candidate to explain the dark matter is weakly interacting massive particle (WIMP), as the name implies is a massive that only couples via the weak interaction and also gravity. The WIMP is theorized to have a mass and cross section on the order of the weak interaction. In the early universe the number density of WIMPs

and photons would have been roughly equation as there was sufficient thermal energy to keep the creation and annihilation in equilibrium.



$\chi$  represents WIMPs and q are standard model particles. The reaction can go back and forth in equilibrium as long as the thermal temperature of the universe is greater than WIMP mass  $T > m_\chi$ .

As the universe expanded and cooled production of WIMPs from standard model particles cease as the temperature of the universe dropped below the WIMP mass, leaving only WIMP annihilation into standard model particles. The annihilation process of WIMPs would have continued leaving only a small number density at the tail of an exponentially falling Boltzmann distribution today. However, if the universe's expansion is fast compared to the WIMP cross section then the WIMPs would have avoided finding each other and their number density could 'freeze out'. Thus, if the acceleration of the universe H is greater than the number density of WIMPs times the cross section.

$$H > \Gamma_A \equiv n_\chi \langle \sigma_A \nu \rangle \quad (1.5)$$

H is the Hubble constant ,  $n_\chi$  is the number density of WIMPs and  $\langle \sigma_A \nu \rangle$  is the thermally averaged annihilation cross-section. The annihilation process can be described by the Boltzmann equation

$$\frac{dn}{dt} = -3Hn_\chi - \langle \sigma_A \nu \rangle (n_\chi^2 - n_{\chi_{eq}}^2) \quad (1.6)$$

Where the first term represents the dilutions of WIMP number density with three

degrees of freedom.  $n_\chi^2$  is from the annihilation process,  $\chi\chi \rightarrow qq$  and  $n_{\chi_{eq}}^2$  is from the reverse process  $qq \rightarrow \chi\chi$ . Equation 1.6 does not have an analytic solution but has been solved numerically[29] , estimating the relic density within 10% to be:

$$\Omega_\chi h^2 = \frac{3 \times 10^{-27} \text{cm}^3 \text{s}^{-1}}{\langle \sigma_A \nu \rangle} \sim \frac{10^{-10} \text{GeV}^{-2}}{\langle \sigma_A \nu \rangle} \quad (1.7)$$

Using a typical weak scale cross-section in equation 1.7,

$$\langle \sigma_A \nu \rangle \sim \frac{\alpha^2}{m_{weak}^2} \sim 10^{-9} \text{GeV}^{-2} \quad (1.8)$$

We find that the relic WIMP density reduces to  $\Omega_\chi h^2 = 0.1$  for a particle with a weak scale interaction, referred to as the WIMP miracle. In good agreement with the expected cold dark matter component of the universe  $\Omega_c h^2 = 0.12029$ [13]

## 1.4 WIMP Dark Matter Searches

There are three methods for detecting WIMPs other than looking for its gravitational effects. First, we can look for the annihilation of dark matter particles into standard model particles using space telescope based experiments. Second, we could try to produce dark matter particles by colliding standard model particles in accelerators and look for a signature of missing energy. Or we can search for rare collisions of dark matter particles with ordinary matter. The first two options would constitute indirect observations as only a standard model particle or missing energy is detected to infer the existence of dark matter, this introduces significant systematics and potential fake signals. The third option is rather attractive as it involves directly observing a collision with a dark matter particle though it too come along

with significant challenges, mainly it requires a near zero background environment in order to observe the additional flux.

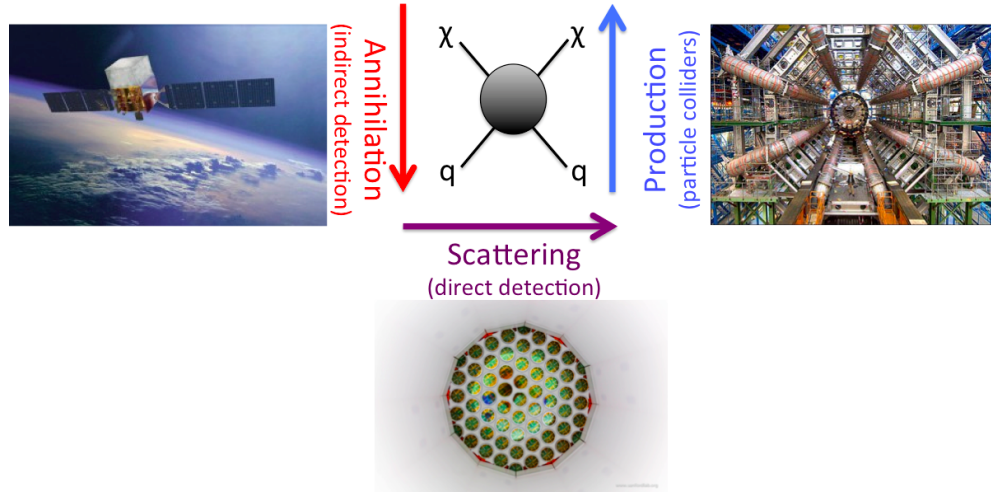


Figure 1.9: Methods for detecting WIMPs from interactions of  $q$ , standard model particles, and dark matter particles  $\chi$ . WIMPs can be detected through the annihilation of dark matter particles into standard model particles,  $\chi\chi \rightarrow qq$ . WIMPs can be produced by colliding standard model particles,  $qq \rightarrow \chi\chi$ . Or one can look for the scatter of a dark matter particle off a standard model particle,  $\chi q \rightarrow \chi q$ .

### 1.4.1 Direct Detection

WIMPS could have masses in the GeV to TeV range and would comprise a quarter of the total mass of the universe. The local density of WIMPs around the earth, at 8 kpc from the galactic center, is about 0.3 GeV/cm<sup>3</sup>, estimated from the galactic rotation curve of the Milky-Way with the assumption of a halo like distribution (figure 1.10 and [1]). Assuming that the WIMP mass is on the order of the weak scale, 100GeV, there are roughly three proton masses worth of WIMPs per liter of space. The velocity of WIMPs near the Earth is about the orbital velocity of objects about the galactic center 240km/s at 8.3 kpc, shown in figure 1.3. WIMPs being highly non-relativistic would scatter coherently off of target nuclei with a cross-section corresponding to  $\sim A^2$ .

WIMP scattering off of target nuclei can be expressed as a classical inelastic collision. The most common energy deposit can be expressed as

$$E_{\max} = r \cdot E_0 = \frac{r}{2} M_\chi v^2 \quad (1.9)$$

Where  $E_{\max}$  is the most frequent energy deposit,  $M_\chi$  is the WIMP mass and  $v$  is the WIMP velocity. The kinematic factor  $r$  for isotropic scattering off a target mass  $M_T$  in the laboratory frame is given by (using 1/2 as the average of 1-cosθ.):

$$r = \frac{4M_\chi M_T}{(M_\chi + M_T)^2} \quad (1.10)$$

Assuming classic billiard ball scattering we calculate expected energy deposits for various WIMPs with weak scale masses of 1 to 1000 GeV/c<sup>2</sup>. Using xenon as the

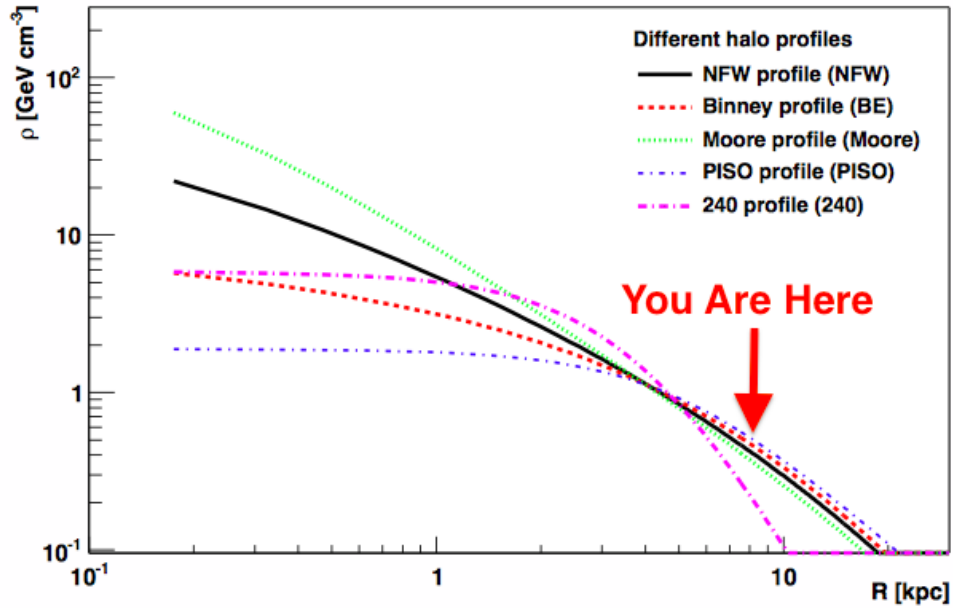


Figure 1.10: Dark matter density vs. distance from the galactic center, calculated from galactic rotation curves of the Milky Way galaxy. The Earth is located at 8.3 kpc. Figure from [1].

target mass ( $M_{Xe} = 122 \text{ GeV}/c^2$ ), and a WIMP velocity of 240 km/s ( $8 \times 10^{-4} c$  ).

$M_\chi [\text{GeV}/c^2]$	$r$	$E_{\max} [\text{keV}]$
1	0.032	0.01
10	0.28	0.90
100	0.99	31.7
10000	0.40	124

Table 1.2: The kinematic factor  $r$  and most common energy deposit  $E_{\max}$  for a WIMP of mass  $M_\chi$  scattering off a xenon nucleus.

To calculate the WIMP-target scattering event rate we follow the derivation given by Lewin and Smith [3]. The differential rate of the WIMP nuclear recoils will be an exponentially decaying spectrum.

$$\frac{dR}{dE_R} = \frac{R_0}{E_0 r} e^{-E_R/E_0 r} \quad (1.11)$$

$E_R$  is the recoil energy,  $E_0$  is the most probable WIMP kinetic energy,  $r$  is the kinematic factor,  $R$  is the event rate per unit mass and  $R_0$  is the total rate. The event rate  $dR$  scattering off a target size  $A$  can be written as

$$dR = \frac{N_0}{A} \sigma \nu dn \quad (1.12)$$

Where  $N_0$  is Avagadro's number,  $A$  is the atomic mass,  $\sigma$  is the cross-section,  $\nu$  is the WIMP velocity and  $dn$  is the differential number density of WIMPs given by:

$$dn = \frac{n_o}{k} \mathcal{F}(\nu, \nu_E) d^3\nu \quad (1.13)$$

Where  $k = (\pi \nu_0^2)^{3/2}$  as  $\nu_{esc} \rightarrow \infty$ , an approximation good to within 0.5% for the Milky Way.  $n_o$  is the particle number density ( $n_o = p_\chi/m_\chi$ ). The WIMP velocity distribution  $\mathcal{F}(\nu, \nu_E)$  is assumed to be ideal gas described by a Maxwellian distribution:

$$\mathcal{F}(\nu, \nu_E) = e^{-(\nu + \nu_E)^2/\nu_0^2} \quad (1.14)$$

Where  $\nu$  is the WIMP velocity,  $\nu_E$  is the earth velocity,  $\nu_0$  is the average velocity (about 230 km/s). We now rewrite equation 1.11 in terms of an integral over all possible velocities rather than energy and plug in the result for  $dR$  (1.12) and  $dn$  (1.13) leading to :

$$\frac{dR}{dE_R} = \frac{R_0}{E_0 r k} \frac{1}{2\pi\nu_0^2} \int_{\nu_{min}}^{\nu_{max}} \frac{1}{\nu} \mathcal{F}(\nu, \nu_E) d^3\nu \quad (1.15)$$

$R_0$  absorbs the constants  $R_0 = \frac{2}{\pi^{1/2}} \frac{N}{A} \frac{\rho_\chi}{M_\chi} \sigma_T \nu_o$ .

Having solved for the differential rate we now calculate the spin independent cross section for WIMPs scattering off nucleons of an atom ( $\sigma_T$ ). We write the cross section as a sum off scattering off protons and neutrons in the nucleus. We use the fact that nucleon coupling for protons and neutrons is approximately equal [30].

$$\sigma_T = \frac{4\mu^2 A}{\pi} [Z \cdot f_p + (A - Z)f_n] \approx \frac{4\mu^2 A^2}{\pi} \sigma_n \quad (1.16)$$

Where  $\mu$  is the reduced mass of the WIMP nucleon system given by:

$$\mu = \frac{M_\chi M_n}{M_\chi + M_n} \quad (1.17)$$

Finally we must add the specific nuclear form factor for the specific target atom to account for decoherence, described by the Helm factor [4]  $F(q)$ . The cross section for spin independent scattering off the target nucleus can be written as a product of the idealized cross section and Helm factor:

$$\sigma_T(q) = \sigma_T F^2(q) = \frac{4A^2}{\pi} \left( \frac{M_\chi M_n}{M_\chi + M_n} \right)^2 \sigma_n F^2(q) \quad (1.18)$$

The spin-independent cross section for WIMPs is found to be proportional to the atomic number squared ( $A^2$ ). The event rate per nuclear recoil energy is plotted for several potential WIMP search target nuclei in figure 1.11.

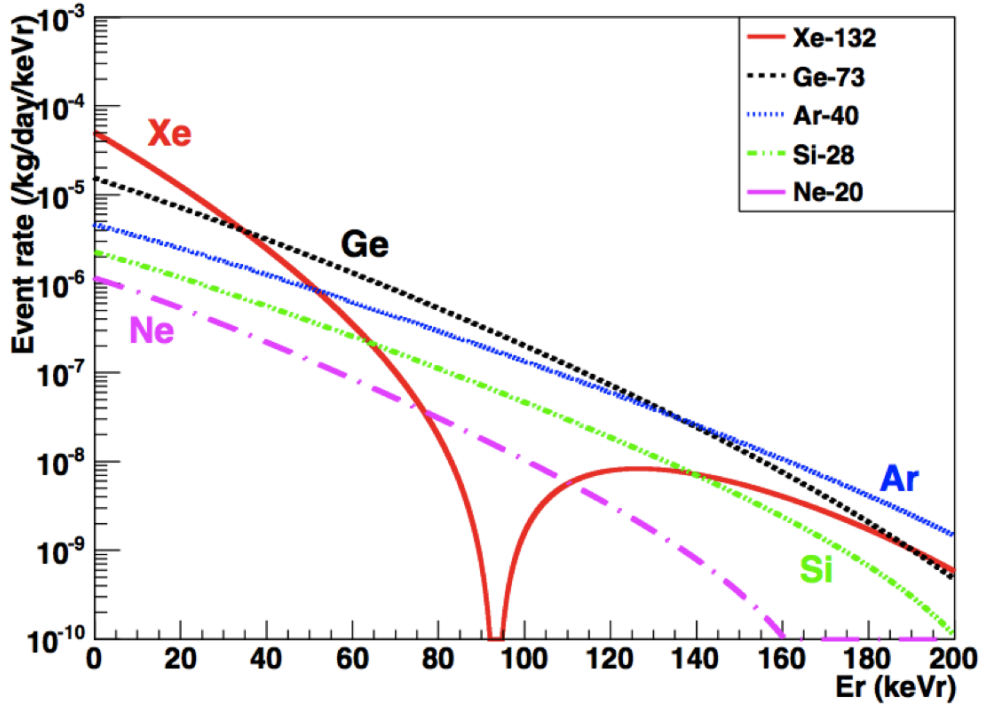


Figure 1.11: Plot of WIMP event rate per kg/day/keV vs. Nuclear recoil energy (keV) for several target nuclei, using parameters from [3]. At low detection threshold xenon is the most attractive target nuclei. The drop off in the xenon spectral shape is due to decoherence described by the Helm factor [4].

Xenon being a relatively heavy element,  $A=131$ , makes it an ideal candidate for a WIMP dark-matter search at low energy thresholds. Xenon detectors today have achieved thresholds as low as 3 keV<sub>nr</sub> [31]. Other common detection mediums are germanium, which is rather expensive on the ton scale, and argon which is inexpensive but contains a troublesome radioactive isotope  $^{39}\text{Ar}$ . To probe dark matter cross sections the next generation experiments must be bigger and contain less radioactive background contamination. With current limits on the WIMP cross section a ton scale xenon experiment may only detect a handful of events per year.

### 1.4.2 WIMP Detection Experiments

Several experiments are currently conducting WIMP dark matter searches using several target nuclei. We have found that the interaction rate for WIMPs with target nuclei is expected to be rare. In the event that a WIMP does strike a target in the detector it will primarily interact with the nucleus, deposit energy, and traverse throughout the detector without a second interaction. Neutrons could also interact with atomic nuclei and fake a WIMP signal, however after the initial energy deposit they are likely to interact again. Thus, neutrons can be rejected by cutting multiple scatters in detectors on the scale of the neutron mean free path at an energy required to fake a WIMP signal (order 10 cm). The most common source of backgrounds are electromagnetic in nature, gammas and betas from the rock surrounding the experiment, detector components, and internal to the xenon. Just like for the case of neutrons the likelihood of a single scatter within the detector is highly unlikely. Naked beta decays are the most troublesome, appearing as a single energy deposit in the detector medium. Fortunately, electronic recoil events can be discriminated from WIMP like nuclear recoil events by more than 1/100 using the ratio of charge to light or charge to phonons produced in the interaction. Xenon based experiments currently having the best limits on WIMP nucleon cross sections [31].

- Xenon experiments: LUX [31], Xenon100 [32] , PandaX [33], XMass [34].
- Argon experiments: Dark Side [35], MiniClean [36].
- Germanium experiments: CDMS [37], CoGeNT [38].

- Bubble chamber using fluorine: PICASSO [39] ( $^{19}\text{F}$ ), COUPP [40] ( $\text{CF}_3\text{I}$ ).

,

## Chapter 2: The LUX Detector

### 2.1 Introduction

The LUX experiment is located 4850 ft underground (4300 m w.e.) at the Sanford Underground Research Facility in Lead, South Dakota. After running for 85.3 live days in 2013, LUX has set the most sensitive limit for a spin-independent WIMP scattering cross section [31] and is expected to achieve five times the sensitivity after a 300 day run ending in 2015.

Nobel elements are promising candidates for WIMP detection. They are easy to purify and are transparent to their own scintillation light. Xenon is especially favorable due to its large atomic mass (131.3 amu) and high liquid phase density ( $\sim 2.9$  kg/l) which provides both an excellent target for coherent WIMP scattering while simultaneously providing excellent stopping power from external radioactivity. Xenon is also free of any long lived isotopes which contribute backgrounds for the WIMP search. There are well established techniques to remove and monitor the residual, troublesome radio isotopes of  $^{39}\text{Ar}$  and  $^{85}\text{Kr}$  found in the atmosphere from which the xenon is distilled [41] [42] [43] [44].

WIMPs, being electrically neutral, primarily interact with the xenon target nuclei producing nuclear recoil (NR) events whereas typical backgrounds in the

detector, gammas and betas, interact with the atomic electrons producing electronic recoils (ER). In liquid xenon ER events can be further discriminated from NR events a factor of 100 or more by measuring the charge to light ratio of the interaction, as explained in section 2.2.2.

## 2.2 The LUX TPC



Figure 2.1: Photo of the outer vessel of the LUX detector from inside the water tank.

Figures 2.1 shows the LUX detector held in place by a stainless steel frame and the water tank that surrounds it. The water tank provides shielding from gammas and neutrons emanating from the surrounding rock, the water tank PMTs used as an active veto are also pictured along the sides of the water tank. Figure 2.2 show a cross sector of the LUX detector's inner and outer vessel. The LUX detector is a two phase xenon time projection chamber (TPC) [31]. The detector contains two PMT

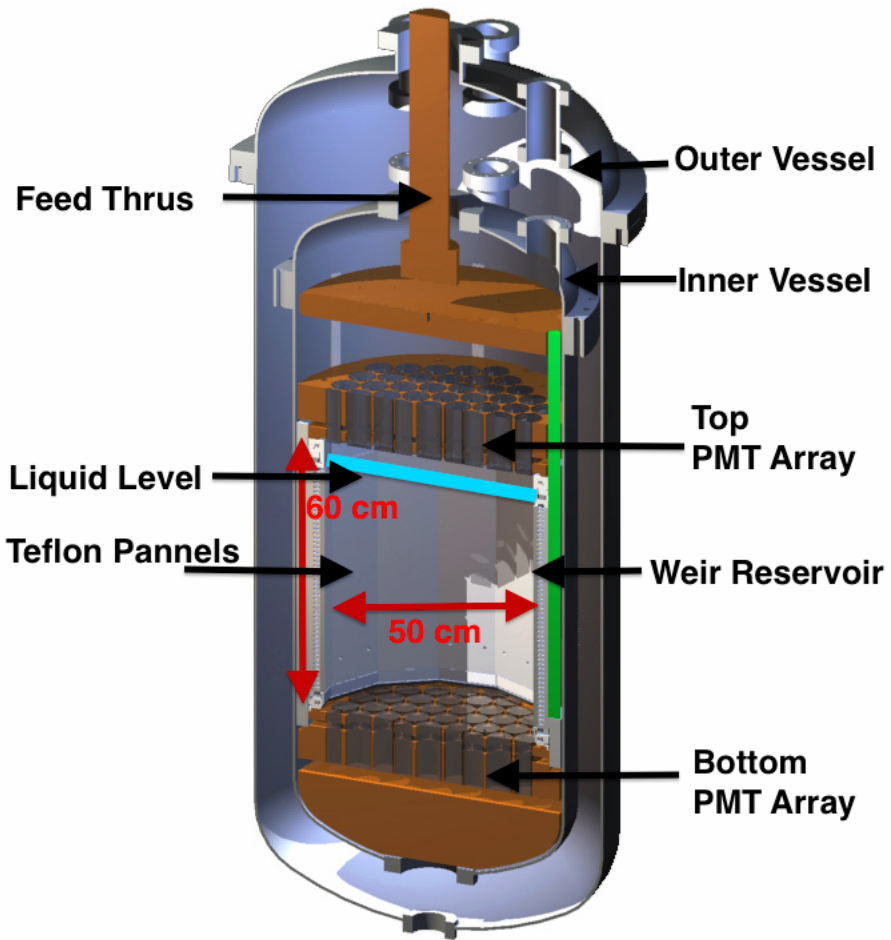


Figure 2.2: Illustration of the LUX detector’s internals. The detector contains two arrays of PMTs on the top and bottom housing 61 PMTs each. Teflon panels on the edges of the active region are used to reflect scintillation signals. The vertical distance between the two PMT arrays is 60 cm, and the diameter to the outer edge of the teflon panels is 50 cm.

arrays on the top and bottom with 61 PMTs each for a total of 122 PMTs, with quantum efficiencies ranging from 30-40%. The active region consists of a 49 cm length between the cathode and gate grid with a 47 cm diameter of the dodecagonal geometry. The drift field between the cathode and gate is 170 V/cm resulting in

an electron drift velocity of 1.51 mm/ $\mu$ s. The liquid level terminates 5-6mm above the gate grid. The liquid level is precisely maintained by a weir reservoir into which xenon between the anode and gate spills into. The anode grid is 1.0 cm above the gate grid and creates an extraction field of 6 [kV/cm] where electrons are removed from the liquid and accelerated causing electroluminescence in the gas phase. LUX contains a gross mass of 370 kg of xenon of which 250 kg are in the active region.

### 2.2.1 Target Xenon

The target xenon is commercially available natural xenon with standard isotopic abundances (table 2.1), initially distilled to  $\sim$  1 part per million (ppm) residual air contamination (N<sub>2</sub>, O<sub>2</sub>, Ar). The commercially available xenon also contained  $\sim$  100 parts per billion (ppb) of krypton which is far greater than the background allowance of 5 parts per trillion (ppt). Krypton contains trace amounts of a beta emitter <sup>85</sup>Kr and is a troublesome internal background dissolved uniformly directly in the detection medium (xenon). The unwanted krypton was removed from the bulk xenon using a gas chromatography technique [43], with the removal independently verified before the science run with a xenon gas analysis technique developed for EXO-200 and LUX [42]. The xenon purity was monitored daily throughout the 2013 science run by an in situ gas analysis system that will be described in detail in section [Sampling]. Just one standard liter of air contains enough krypton to raise the concentration in the LUX xenon above the background goals. Daily krypton monitoring ensured that the krypton content in the xenon remained constant at 4

parts per trillion over the 2013 science run[5].

Electronegative impurities such as N<sub>2</sub>, O<sub>2</sub> and H<sub>2</sub>O attenuate electrons drifting through the xenon and must be removed in order to properly reconstruct events originating deep in the detector. These impurities continuously emanate from detector components degrading the free electron attenuation length. The accumulation of electronegative impurities is countered by circulating the xenon at 26.5 SLPM through a heated zirconium getter. The gross mass of 370 kg has a turn over time of 1.65 days. The monitoring of several impurities using the in situ ahas analysis system is described in detail in section [Sampling]. Throughout the 2013 science the electron attenuation length was measured to be 75 cm to 150 cm, corresponding to 70% to 50% charge loss for events originating from the bottom of the active region.

Isotope	Natural Abundance (%)
<sup>124</sup> Xe	0.09
<sup>126</sup> Xe	0.09
<sup>128</sup> Xe	1.92
<sup>129</sup> Xe	26.44
<sup>130</sup> Xe	4.08
<sup>131</sup> Xe	21.18
<sup>132</sup> Xe	26.86
<sup>134</sup> Xe	10.44
<sup>136</sup> Xe	8.87

Table 2.1: Xenon isotopic abundances, from [45]

### 2.2.2 Background Rejection

Xenon has a density of  $\sim 2.9$  g/cm giving it excellent stopping power for shielding against external radioactivity. External radioactivity with energies in the WIMP

search region of interest (below 50 keV) only penetrate millimeters in xenon, being completely absorbed in the outer edges of the detector. Gammas in the MeV range have mean free paths on the order of 3 cm and are likely to be cut by the single scattering requirement . The most troublesome of the gamma backgrounds are from PMT materials containing trace amounts of uranium and thorium located inside the TPC. Figure figure 2.3 shows a simulation of expected gamma background events inside the LUX detector, using the single scatter cut requirement. By cutting out the edge events we can gain at least an additional factor of 1000 background rejection within the fiducial volume (inside the black dashed lines) [5].

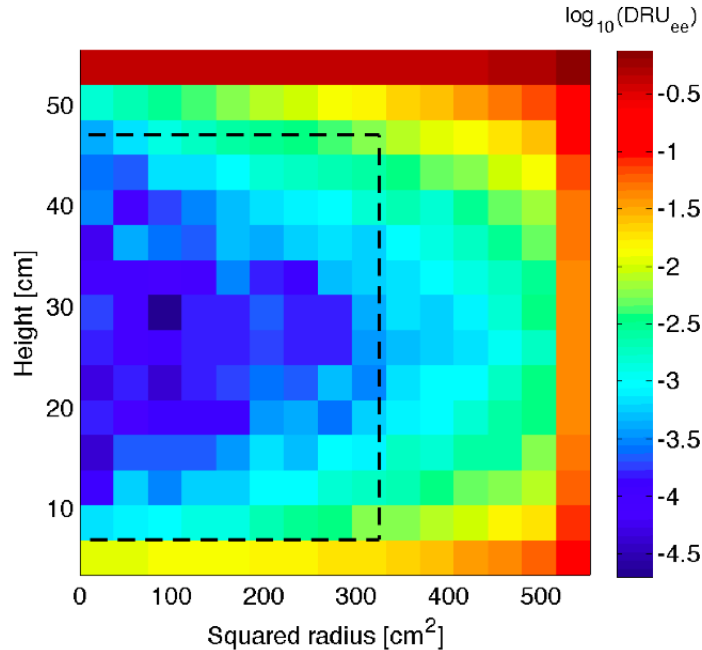


Figure 2.3: Simulation of expected gamma background events inside the LUX detector, using the single scatter cut requirement[5]. There is an additional factor of 1000 background rejection within the fiducial volume where the WIMP search is conducted (inside the black dashed lines) .

Another means for discriminating background events is through measuring the charge to light ratio of each event. WIMPs will produce nuclear recoils whereas gammas and betas interact primarily with atomic electrons, resulting in different charge to light ratios of a given energy deposit. Using AmBe and  $^{252}\text{Cf}$  neutron sources along with a tritium calibration source the NR to ER discrimination factor was measured to be  $99.6 \pm 1$  % at 50% NR acceptance. Meaning that only one in 250 of the residual gamma and beta background events is expected to fake a WIMP signal when cutting out half of the potential nuclear recoil candidates. The ER type and NR type bands are shown in figure 2.4 with the band means as solid lines (Blue and Red, respectively) and the 10-90% CL as dashed lines. The internal tritium calibration source will be discussed in further details in section (Tritium Section).

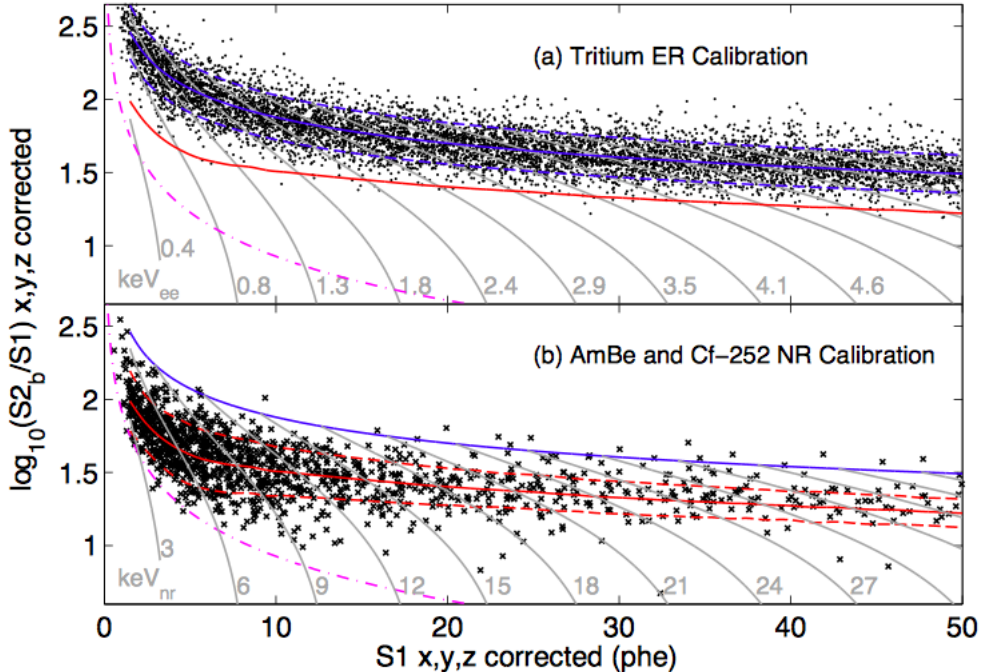


Figure 2.4: The ER type and NR type bands from a) AmBe and  $^{252}\text{Cf}$  (Red) and b) tritium calibration (Blue). The band means are solid lines and the 10-90% CL are shown as dashed lines. The ER to NR discrimination by using the charge to light ratio was measured to  $99.6 \pm 0.1\%$  at 50% NR acceptance.

### 2.2.3 The Drift Field inside the LUX TPC

The LUX TPC contains five wire grids used to control the electric fields inside the detector. The grids and their spacings are shown in figure 2.5, labeled from top to bottom as Top (T), Anode (A), Gate (G), Cathode (C), Bottom (B). The grids T,A,G,C,B are biassed at -1,+3.5,-1.5,-10,-2 (all in kV), respectively. The PMTs are biased to -1.2 kV on average. The field created in the active region between the cathode and gate is also shown in figure 2.5. On average the drift field is 170 V/cm with variation from 140 V/cm to 200 V/cm from cathode to gate. The extraction

region between the anode and gate has a 6 kV/cm field. This extraction field is used to create the secondary scintillation (S2) signal via electroluminescence as the electrons are extracted and accelerated. The top and bottom grids serve to shield the PMTs from the anode and cathode biases.

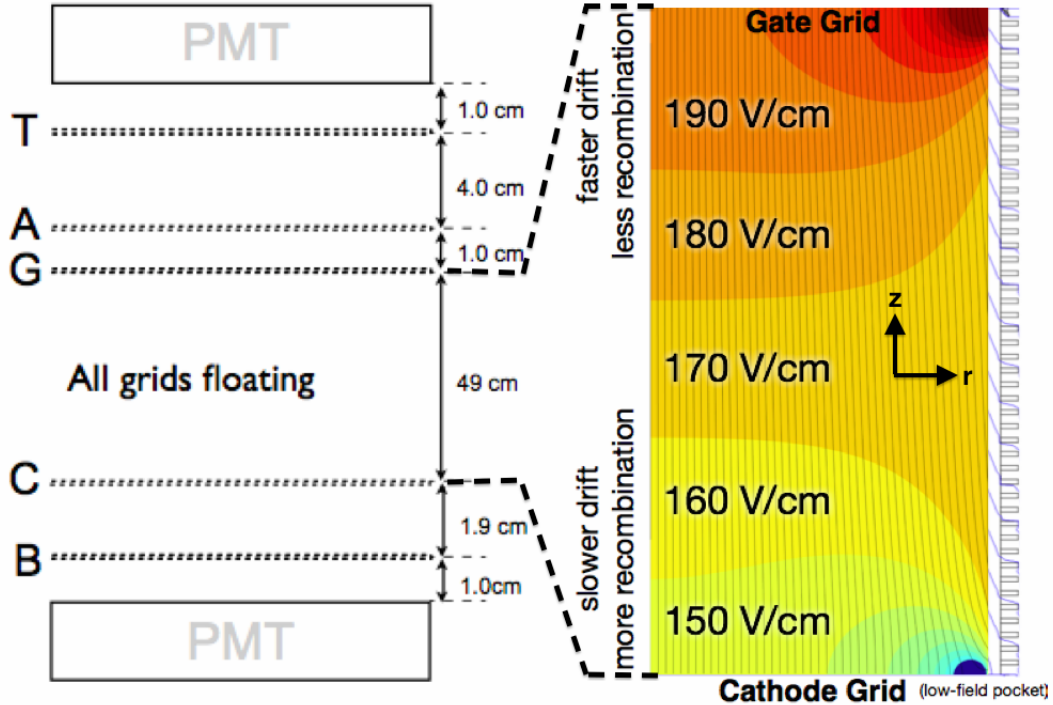


Figure 2.5: Field grids in the LUX detector during the 2013 science run. T,A,G,C,B are biassed to -1,+3.5,-1.5,-10,-2 (all in kV), respectively. The PMTs are biassed to -1.2 kV on average. The figure on the right shows the electric field model in the drift region between the cathode and gate for drift distance  $z$  vs. detector radius  $r$ . On average the drift field is 170 V/cm with variation from 140 V/cm to 200 V/cm from cathode to gate. Electric field model from [6].

## 2.3 Light and Charge Signals in Liquid Xenon

When energy is deposited in the active region of the xenon TPC it is converted to ionization, excitation and heat.

$$\begin{aligned} E &= W(n_i + n_{ex}) + \text{Heat} \\ E &= W(n_\gamma + n_e) + \text{Heat} \end{aligned} \quad (2.1)$$

where  $E$  is the energy of the deposition in keV,  $n_q$  is number of quanta (photons + electrons),  $n_i$ ,  $n_{ex}$ ,  $n_\gamma$  and  $n_e$  are the number of ions, excitons, photons and electrons respectively. The work function ( $W$ ) for xenon has been measured to be  $13.7 \pm 0.2$  [quanta/eV] [46]. The number of photons observed for a given energy deposit arise from the excitons that de-excite and from ions which recombine with freed electrons. The number of electrons corresponding to a given energy deposit is equal to the number of ions that did not recombine with a freed electron.

$$\begin{aligned} n_\gamma &= n_{ex} + n_i r = n_i(r + \alpha) \\ n_e &= n_i(1 - r) \end{aligned} \quad (2.2)$$

Where  $r$  represents the electron-ion recombination probability and  $\alpha$  represents the ratio  $n_{ex}/n_{ion}$ . The model given in equation 2.2 states that for each additional photon produced from recombination a corresponding electron is lost, and visa versa. The value of  $\alpha$  for an ER event is approximately 0.06 and is expected to be independent

of energy [47] [48] [46]. For nuclear recoils  $\alpha$  is approximately 1 [46]. The light and charge production in liquid xenon will be discussed in further detail below. Some useful properties of xenon are listed in table listed in table 2.2.

Parameter	Value	Ref.
Scintillation wavelength	174-178 nm	[49]
W (work function)	$13.7 \pm 0.2$ [eV/quanta]	[46]
Xe <sub>2</sub> <sup>*</sup> singlet lifetime	2.2 ns	[50]
Xe <sub>2</sub> <sup>*</sup> triplet lifetime	27 ns	[50]
Recombination time	45 ns	[51]
Liquid density at boiling point	2.95 g/l	[52]

Table 2.2: Properties of xenon.

### 2.3.1 Electronic Recoils (ER)

For an electronic recoil event the energy lost to heat is only about 5% [53] thus, equation 2.1 is valid for use with electronic recoils, we simply drop the small loss to heat. A schematic of an ER event is shown in figures 2.6 which we will overview. When an incoming beta or gamma interacts with the electron of the xenon atom the energy deposited is converted primarily to ionization, with roughly 6% excitation and  $\sim 5\%$  is lost to heat [48] [53]. Excitons arise from ionized xenon atoms that bond together forming diatomic molecules (Xe<sub>2</sub><sup>\*</sup>). Xenon excitons will de-excite with characteristic time constants of 2.2 and 27 ns for the singlet and triplet state, respectively, producing  $\sim 175$ nm scintillation light. Ion-electron pairs produced via ionization can also recombine, with probability  $r$ , producing additional excitons resulting in the production of additional  $\sim 175$ nm scintillation light. The characteristic recombination time constant is 45 ns [51]. Each initial exciton or recombining ion

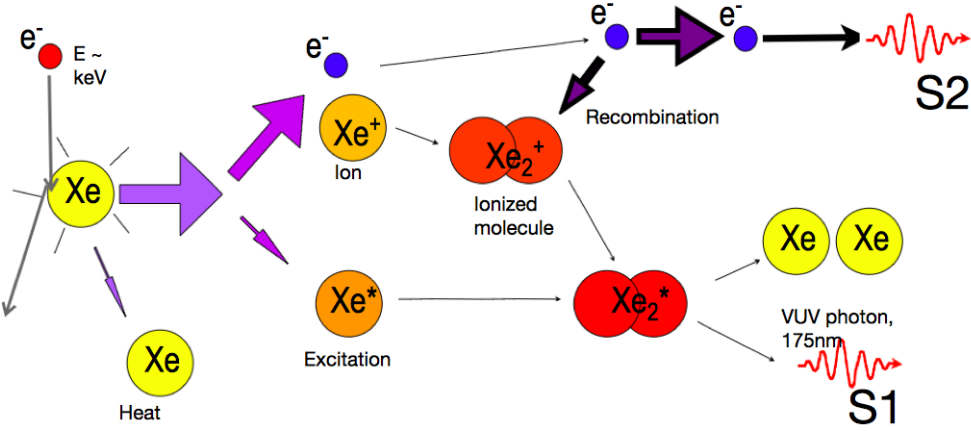


Figure 2.6: An electronic recoil (ER) event in xenon. The energy deposited is converted primarily to ionization and roughly one tenth for excitation. Only several percent is lost to heat. Xenon excitons and recombining electron ion pairs for xenon dimers which de-excite producing very ultra violet (VUV) scintillation light at 175nm producing the primary scintillation signal (S1). Electrons that do not recombine are drifted by an electric field into the gas phase where they are accelerated producing the secondary scintillation (S2) signal.

produces one scintillation photon, as written in equation 2.2. The two paths for photon production overlap in time and sum to produce the primary scintillation signal (S1). The S1 signal is collected by the PMT arrays within 500 ns. Electrons that escape recombination , with probability  $1-r$ , begin to drift upwards under the influence of the electric field between the cathode and gate (shown in 2.5). The electrons eventually reach the liquid-gas interface where they are extracted into the gas. As they accelerate, the extracted electrons produce a larger secondary scintillation signal (S2) that is proportional the the number of electrons extracted. The drift times for the electrons in the 49 cm long active region range from 1 to 324  $\mu\text{s}$  with an average drift velocity of 1.51 mm/ $\mu\text{s}$ . Thus, the S2 signal is well separated from the S1.

### 2.3.2 Nuclear Recoils (NR)

For nuclear recoils the energy lost to heat is more than half the total energy deposition [53]. This energy is lost through elastic collisions with other xenon atoms that fall below the ionization threshold. The energy lost to heat is characterized by an energy dependent Lindhard factor ( $\mathcal{L}$ ) [54], written as:

$$E = \mathcal{L}^{-1}W(n_\gamma + n_e) \quad (2.3)$$

A schematic of a NR event is shown in figure 2.7. The signal production follows the same process as described above for an ER event but with greater amount of energy going towards heat and exciton production.

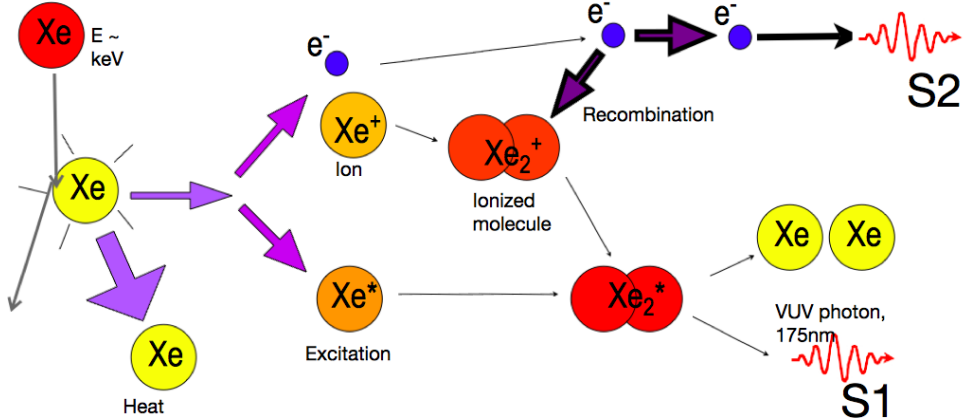


Figure 2.7: A nuclear recoil (NR) event in xenon. The energy deposited goes mainly towards heat (phonons), the remaining energy is split evenly between ionization and excitation. Xenon excitons and recombining electron ion pairs for xenon dimers which de-excite producing very ultra violet (VUV) scintillation light at 175nm producing the primary scintillation signal (S1). Electrons that do not recombine are drifted by an electric field into the gas phase where they are accelerated producing the secondary scintillation (S2) signal.

The additional energy lost to heat leaves less energy available for excitation and

ionization for an NR event. Further, NR events produce roughly equal amounts of ionization and excitation whereas ER events produce mostly ionization [53] [46]. Relative to an ER event, a NR event will have less electron ion pairs leading to a reduction of the S2 signal and enhancement of the S1. Thus, the ratio of S2 to S1 for a NR event is quenched compared to an ER event with an equivalent energy deposition. The quenching of the charge to light ratio is what leads to additional discrimination between nuclear and electronic recoil demonstrated in figure 2.4.

### 2.3.3 Energy and Position Reconstruction

In order to reconstruct the true energy of an event we will need to know its nature, ER or NR. For ER events we work in units of electronic equivalent energy, ( $\text{keV}_{\text{ee}}$ ), using equation 2.1 neglecting the small heat loss. ER calibrations will be discussed in greater detail in section [ER calibration]. For NR events the energy is reconstructed in terms of nuclear recoil equivalent energy ( $\text{keV}_{\text{nr}}$ ), using equation 2.3 with the Lindhard factor measured from calibration data given in [55] [56]. An illustration of an energy deposition in the LUX detector is shown in figure 2.8. The time difference between the S1 and S2 pulse defines the drift time, the drift time gives the measure of the z coordinate (depth). The hit pattern of the S2 signal on the top PMT array measures the x,y coordinates of the event. From the S1 and S2 signals the full x,y,z position and energy deposit of the event can be reconstructed.

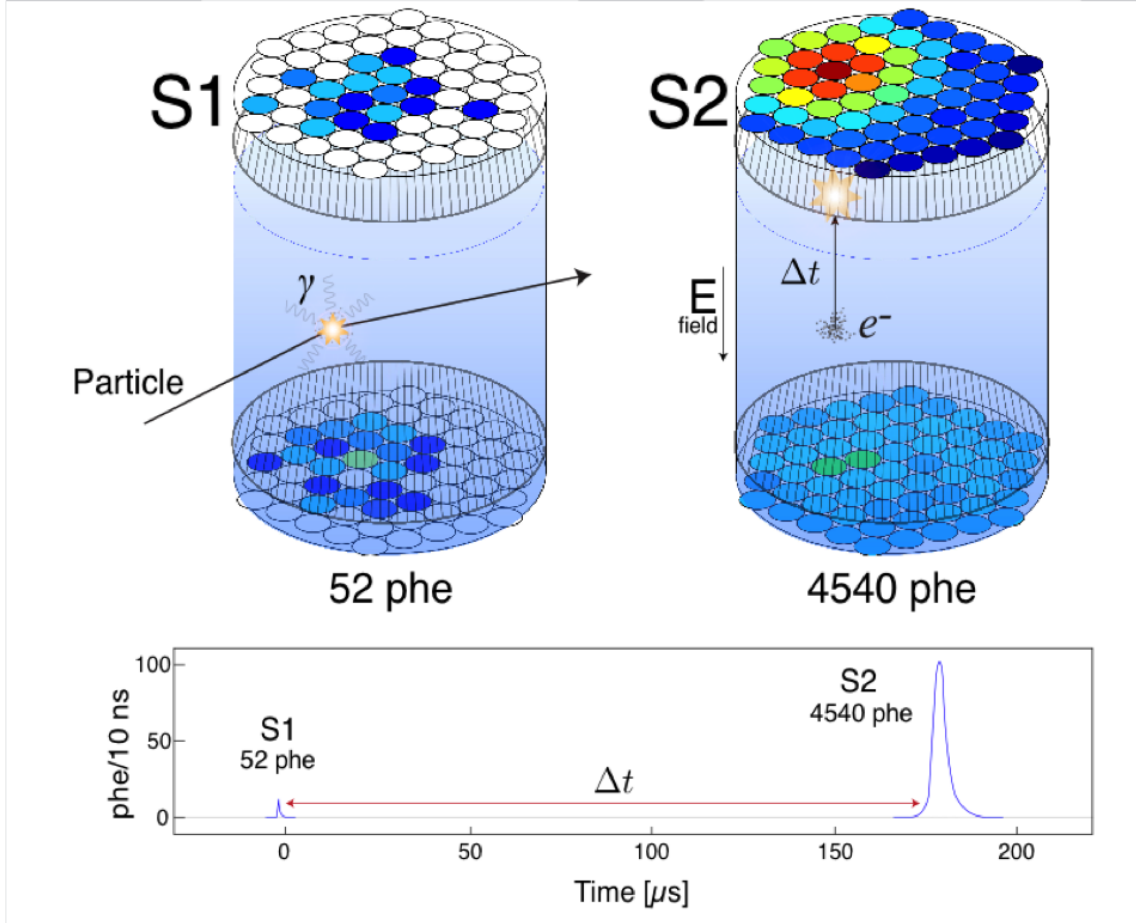


Figure 2.8: Event diagram.

## 2.4 Identifying S1, S2

The primary and secondary scintillation signals can be identified by their unique properties. The S1 signal has a fast rise time and decays on the order of 10s of nanoseconds as the dimers of xenon produced through excitation and recombination de-excite (time constants listed in table 2.2). The S2 signal arrives several  $\mu s$  later with the electron population spread out spatially about its centroid due to diffusion, transverse and radial [57]. The characteristic S2 signal is thus one with a slow rise and corresponding slow fall. It resembles a bell curve, as the diffused electron

population arrives, peaking at the centroid of the distribution. A 2 keV event as seen by all 122 PMT channels is showing in figure 2.9. The S1 pulse is fast and the S2 pulse is much larger with a slower rise-time. The S2 pulse is larger since a single electron creates hundred of photons as it is accelerated in the extraction region.

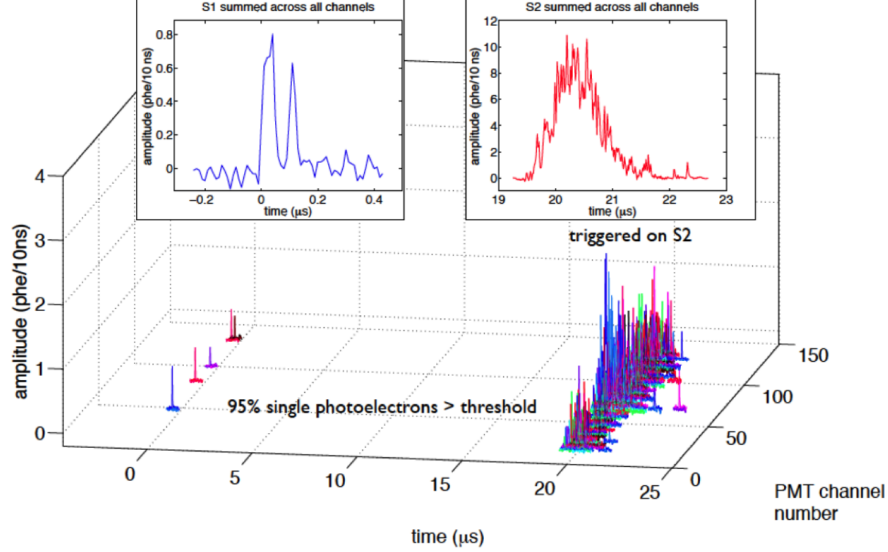


Figure 2.9: 2keV ER event as seen by each PMT channel of the LUX detector. The S1 signal summed across all channels is overlaid on the top left, and the S2 signal summed across all channels is overlaid on the top right.

To identify S1 and S2 populations we define the variable Prompt Fraction as the area covered in the first 10% of the pulse normalized to the total area. The calculation is performed on the summed waveform after a first pass which defines the pulse's start and end timestamp. The separation of population density when plotting the total Pulse Area (measured in detected photo electrons [PE]) vs. Prompt Fraction is shown in figure 2.10, for the case of a  $^{83m}\text{Kr}$  data set (41.5 keV)

and a tritium calibration data set (1-18.5 keV). The population of single electrons, single photons and the S1 S2 pairs associated with  $\gamma$ ,  $\beta$  and  $\alpha$  interactions are well separated and are highlighted as rectangles. The upper left corner is the single photon population, their areas consist of approximately 1 PE, the definition of the PMTs response to a detected photon. The single electron population is labeled SE and peaks at roughly 20 PE with a prompt fraction of -1. For all S1 pulses the prompt fraction is found to be between 1 and 0.3 ( $\log_{10}$  of 0 and -0.5) for the entire range of Pulse Area. The pulse area is a proxy for energy deposit, spanning from 1 keV tritium events to 7 MeV alphas. The populations of S2 from  $^{83m}\text{Kr}$ , tritium,  $\gamma$ ,  $\beta$  and  $\alpha$  are found to have Prompt Fractions more than an order of magnitude smaller than their corresponding S1.

The S1 and S2 signal corresponding to an event are identified using a prompt fraction selection that had been tuned to calibration data. Valid S1 and S2 signals that spill into the single electron and single photon region at low energies can be identified by requiring the pulses be paired. For the WIMP search we define ‘golden’ events consisting of single scatters with a single S1 paired with a subsequent S2 pulse with a timing separation not exceeding the maximum drift time inside the TPC. With the golden requirement each event has a well defined x,y coordinate and z making it possible to correct the signals for geometry and electron attenuation.

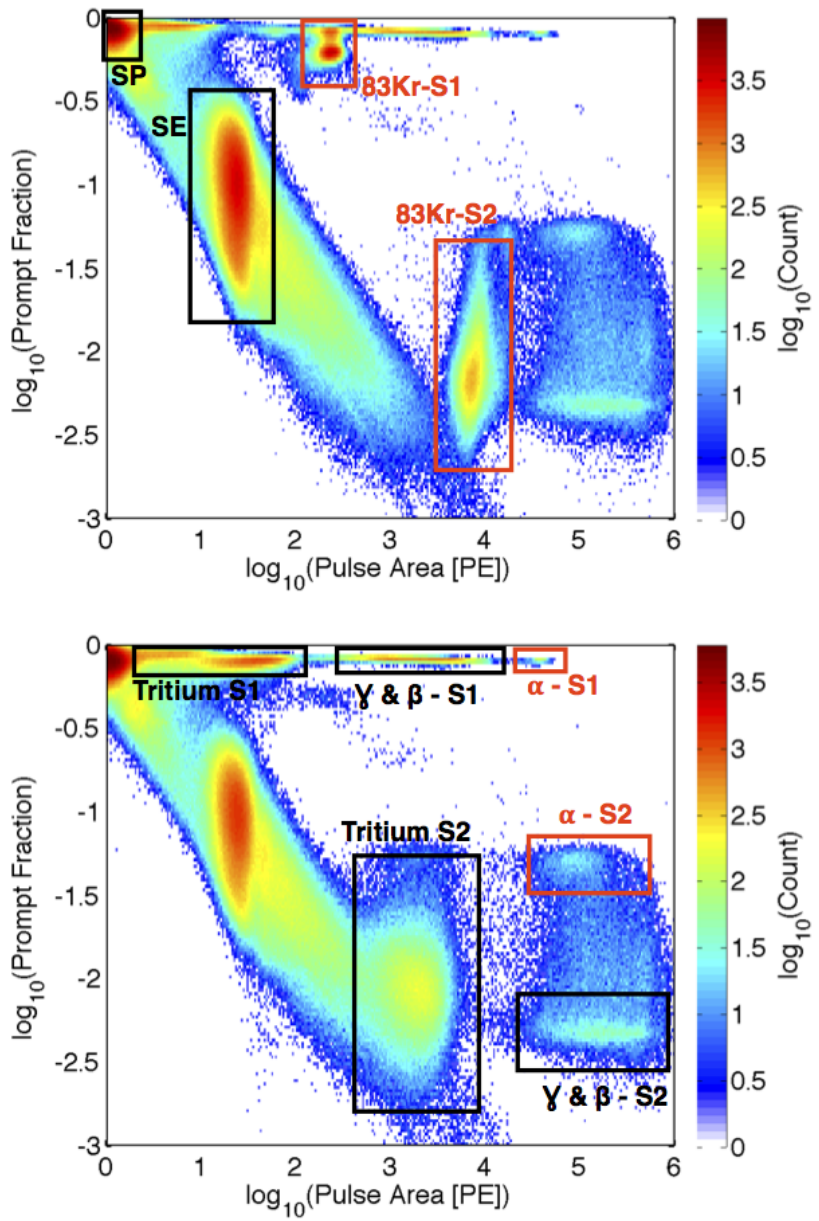


Figure 2.10: Density plot of prompt fraction vs. Pulse Area. Top:  $^{83\text{m}}\text{Kr}$  data set.

Bottom: Tritium data set. Populations of single electrons, single photons and the

S1 S2 pairs associated with  $\gamma$ ,  $\beta$  and  $\alpha$  are highlighted as rectangles.

## 2.5 LUX Science Result (WIMP limit)

The first science run of the LUX detector consisted of 85.3 live days from April 21, 2013 to Aug 8, 2013. A total of 83,673,413 triggers were recorded with 160 remaining as golden after applying quality cuts, listed in table 2.3.

Cut	Events Remaining
all triggers	83, 673, 413
detector stability	82, 918, 902
single scatter	6, 585, 686
S1 energy (2 - 30 phe)	26, 824
S2 energy (200 - 3300 phe)	20, 989
single electron background	19, 796
fiducial volume	160

Table 2.3: Data quality cuts used for the WIMP search results presented in [31].

Detector stability cuts remove the live time in which liquid level, gas pressure or grid voltages were out of normal ranges. The single scatter cut requires a single S1 with a subsequent S2 within a time window of  $324 \mu\text{s}$ , the maximum time required for electrons to traverse the active region. An area cut was also placed on both the S1 and S2 in order to narrow the energy region of interest. The minimum S2 requirement of 200 PE ensures the quality of the x,y position reconstruction, with  $\sim 8$  extracted electrons. An additional cut was placed around time windows with anomalously high single electron rates. All single scatter WIMP search events before applying the fiducial cut are shown in figure 2.11, the vast majority of events occurring at the edges of the detector. The fiducial cut reduces residual radioactivity from the detector surface and PMTs by another two orders of magnitude. The fiducial cut consists of a radial cut at radius less than 18 cm from the detector

center. The z coordinate in drift time is defined to be 0  $\mu\text{s}$  at the liquid surface and 324  $\mu\text{s}$  at the cathode. The fiducial cut in z required that event drift times be between 38 and 305  $\mu\text{s}$ , corresponding to 6 to 46 cm below the liquid surface (drift velocity = 1.51 mm/ $\mu\text{s}$ ). The fiducial cut is shown as the dashed cyan line in figure 2.11.

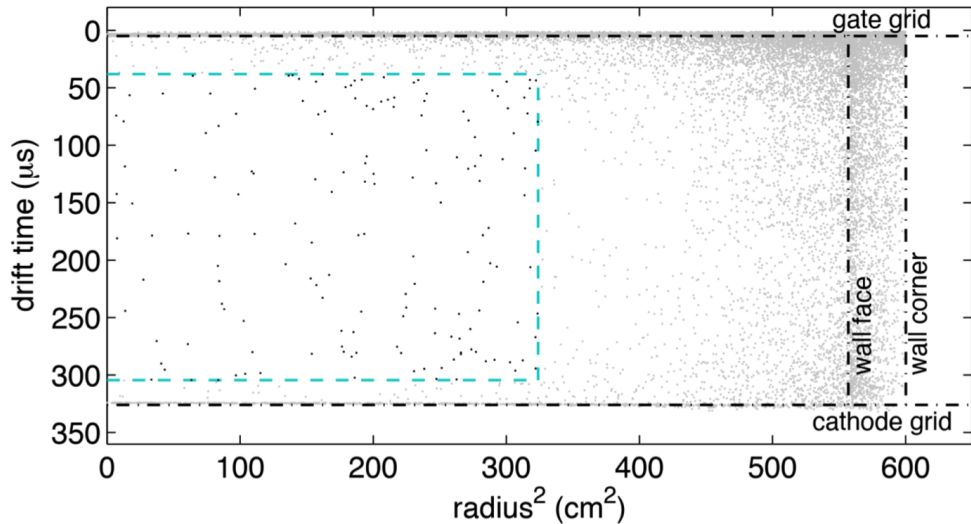


Figure 2.11: All single scatter events seen in the active region of the LUX detector over the course of the first science run passing all cuts listed in table 2.3 excluding the fiducial cut. The dashed cyan box indicates the fiducial volume.

Within the fiducial volume 160 events remain which meet our WIMP search energy requirement. The energy cut is placed in terms of S1 from 2-30 PE. As explained in chapter [Energy Calibrations] this corresponds to roughly 1.0 to 6 keV<sub>ee</sub> or 3 to 25 keV<sub>nr</sub>. We choose to select events based on S1 because it is directly observed, whereas true energy depends on the nature of the event (ER or NR) and must be inferred. The ER and NR discrimination band was measured using

calibration data and shown in figure 2.12. The blue and red bands represent the 10% to 90% confidence bounds of events being ER and NR type, respectively. The ER band was measured using a tritium calibration source ( $\beta^-$ ) and the NR band was measured with neutrons from AmBe and  $^{252}\text{Cf}$  along with NEST simulations [56]. The ER/NR discrimination at 50% NR acceptance was measured to be  $99.6 \pm 0.1$  %. This value serves as a proxy for background events rejection, which is ultimately treated with a profile likelihood method on an event by event basis. Both the S1 and S2 signal have been corrected for spacial dependance which is discussed in further detail in Chapter . Due to cross talk or shorts, two PMTs on the top array and one on the bottom were left unbiassed. In order to avoid misreconstructing events extracted around the unbiased top PMTs only the bottom PMT array was used for the S2 signal ( $S2_b$ ).

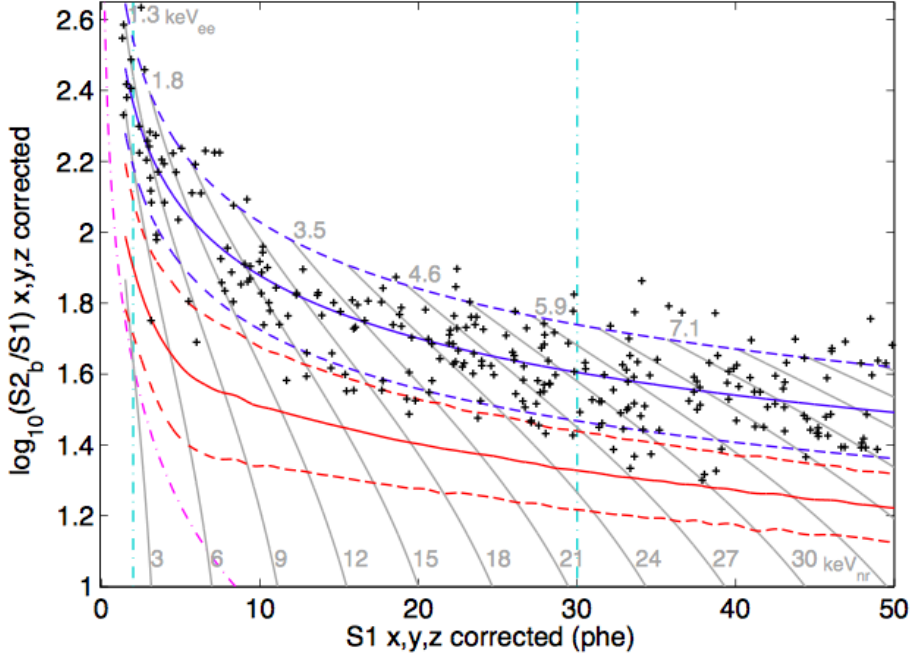


Figure 2.12: The remaining events passing the quality cuts listed in table 2.3. The charge to light ratio ( $S_2/S_1$ ) is plotted vs.  $S_1$  (proportional to energy) to show the separation of ER and NR type events. The 10-90% CF limits of the ER and NR band are plotted as the dashed blue and red curves, respectively. The band means are solid.  $S_{2b}$  stands for the  $S_2$  signal on the bottom PMT array.

All 160 remaining events in the fiducial volume are consistent with being ER type events. The main source of BG events include residual  $^{85}\text{Kr}$ , activated  $^{127}\text{Xe}$  and  $^{214}\text{Pb}$  from  $^{222}\text{Rn}$ , described in further detail in [5]. The residual ER background rate in the WIMP region of interest as found to be  $3.6 \pm 0.3$  mDRU ( $10^{73}$  cnts/keVee/kg/day) with an expectation of  $2.6 \pm 0.2_{\text{stat}} \pm 0.4_{\text{sys}}$  mDRU.

A profile likelihood test is conducted on all WIMP search candidates remaining after the cuts listed in table 2.3. Testing the charge to light ratio ( $S_{2b}/S_1$ ) vs. energy ( $S_1$ ) for likelihood of being an expected ER background. The signal model for the

test is derived from AmBe and  $^{252}\text{Cf}$  neutron calibrations. The background rates input into the profile likelihood were independently measured and modeled with LUXSIM using NEST, described in further detail in [5] [31] [56]. The WIMP signal model was generated using an isothermal halo with a Maxwellian distribution, with a local WIMP density of 0.3 GeV/cm<sup>3</sup> (as discussed in section 1.4). The galactic escape velocity input into the model is 544 km/s (cutting off the high end of WIMP velocity distribution), with an average WIMP velocity of 220 km/s. The earth's seasonal velocity being 245 km/s with respect to the galactic center. The result from the 2013 science run with the LUX detector is consistent with a P value of 0.35 for the background only hypothesis. The 90% upper C.L. cross section for various spin independent masses are shown in figure 2.13. The minimum cross section reported occurs at  $7.6 \times 10^{-46}$  cm<sup>2</sup> for a WIMP mass of 33 GeV/c<sup>2</sup> [31]. The LUX result is a factor of two improvement in WIMP cross section sensitivity over the Xenon100 limit reported in 2012 [32] and is in tension with reported WIMP signal claims from CoGent [38], CDMSLite (Silicone) [58], CRESST II [59] and DAMA/LIBRA [60].

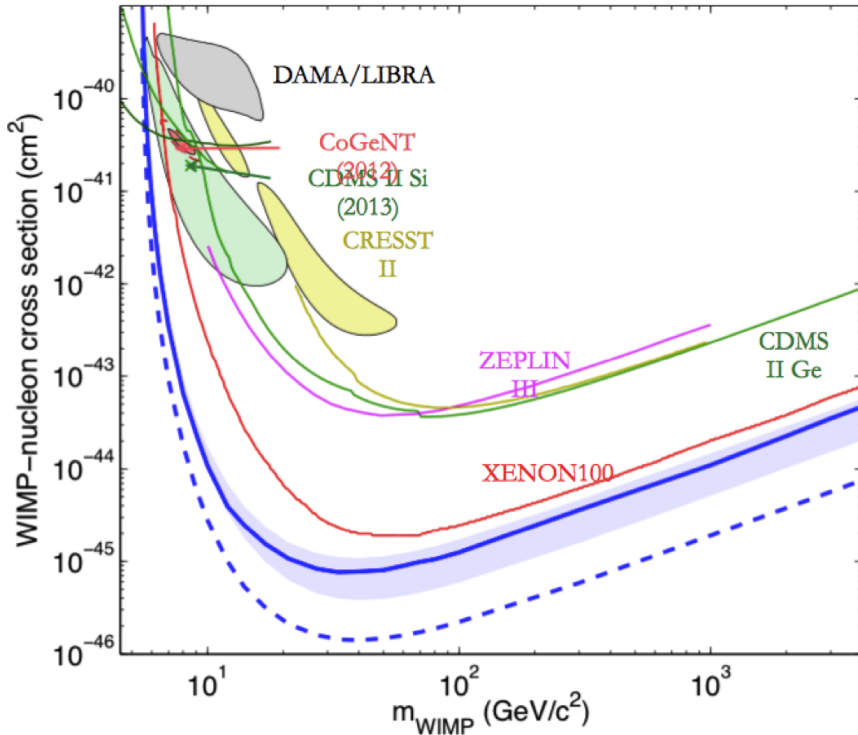


Figure 2.13: LUX detector is consistent with a P value of 0.35 of the background only hypothesis. The 90% upper C.L. cross section for various spin independent masses are shown in figure 2.13 in blue. Also shows are limits from Xenon100 (red), CDMS II (green), ZEPLIN III (magenta), and one sigma signal claimed for DAMA/LIBRA (shaded grey), CDMS II Silicone (shaded green), CRESST II (shaded yellow).

As mentioned above the ER band is measured with a novel tritium calibration source and will be discussed in further detail in Chapter [TritiumSource]. Since the initial science run we have gathered twenty times the tritium statistics to further study the ER band, with 150,000 events in the fiducial volume. We also spent several months deploying a DD neutron generated source to further study the NR band mean. The results from the improved ER and NR calibrations will be reported

in this thesis along with the implications for an improved WIMP limit. An updated profile likelihood reanalysis of the LUX WIMP search result will be submitted for publication in late Fall of 2014.

## Chapter 3: Spacial Dependent Correction of the S1 and S2 Signals

In this chapter we address the spacial dependent corrections applied to the S1 and S2 signal. The S2 position dependent correction is dominated by the z dependent electron attenuation. S2s of equal sizes are exponentially attenuated with increasing depth in the detector. The S1 position dependent correction normalizes for photon detection probability as a function of the event origin given the x,y,z coordinate. Knowing the x,y,z position of each event provides a powerful tool for reducing fluctuations in the signals due to detector geometry. The better we can correct for position dependance of the S1 and S2 signals the smaller the observed fluctuations will be, leading to better ER, NR discrimination and ultimately better signal to background for the WIMP search.

### 3.1 $^{83\text{m}}\text{Kr}$ Calibration

Throughout the science run periodic  $^{83\text{m}}\text{Kr}$  injections were performed to calculate position dependent corrections.  $^{83\text{m}}\text{Kr}$  is produced from the decay  $^{83}\text{Rb}$  with a half life of 86.2 days. The  $^{83}\text{Rb}$  source used is housed in charcoal and plumbed directly into the LUX circulation system. A decay scheme of  $^{83}\text{Rb}$  and  $^{83\text{m}}\text{Kr}$  is shown in figure 3.1.

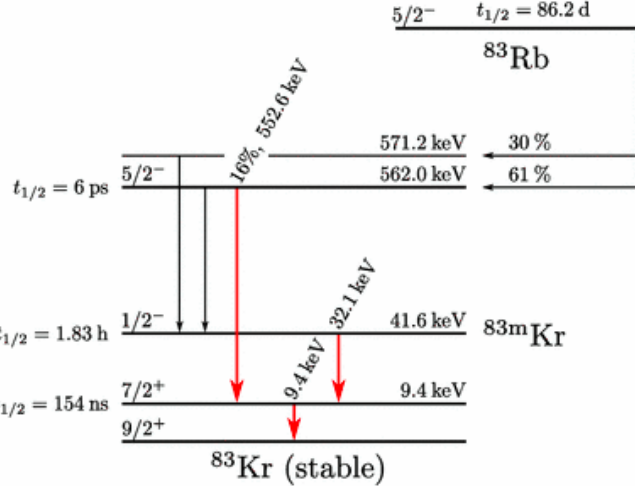
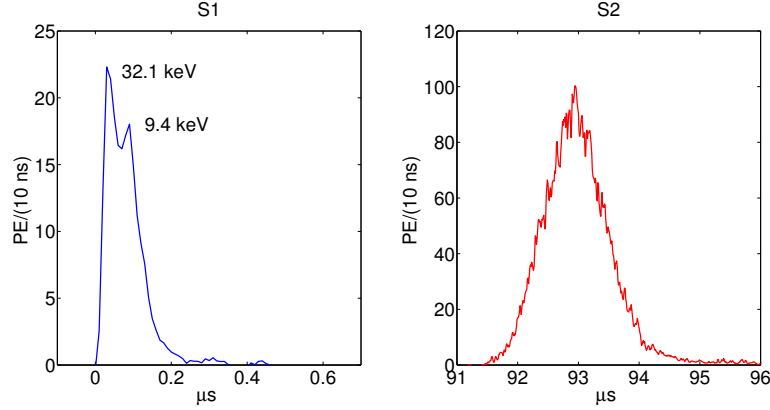
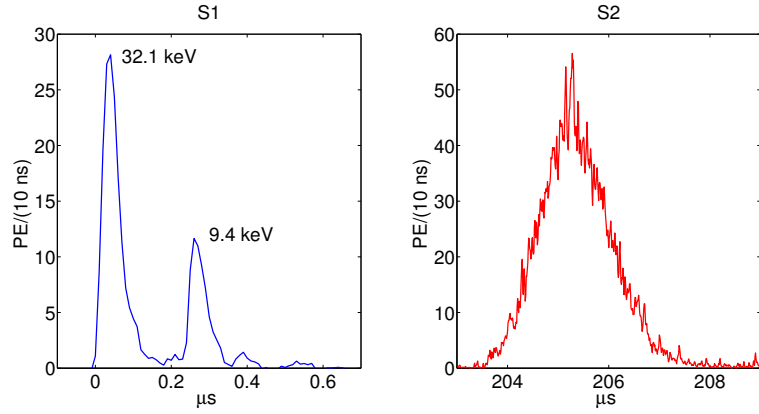


Figure 3.1: A simplified decay diagram of  $^{83}\text{Rb}$  and  $^{83\text{m}}\text{Kr}$ , from [7].

The daughter  $^{83\text{m}}\text{Kr}$  is continually produced in the charcoal housing, having a half-life 1.8 hours.  $^{83\text{m}}\text{Kr}$  decays via an electron capture first emitting a 32.1 keV x-ray followed by a 9.4 keV x-ray with a half life of 154 ns between the two [61] [62]. For the vast majority of the decays the combined S1 pulse corresponding to (41.55 keV) is observed, since the minimum S1 pulse separation in the LUX reconstruction is 1000 ns. Figure 3.2 shows two  $^{83\text{m}}\text{Kr}$  waveforms (S1 and S2) with the the decay of the 32.1 and 9.4 keV x-ray split by 60 and 220 ns, both S1s shown are classified as a single S1 event. The timing separation between the S1 and S2 is used to infer the drift distance to be 14.0 and 40.0 cm below the liquid surface, respectively. The degradation of the S2 signal that originated from deeper in the detector is apparent by comparing the amplitudes of the S2, with roughly 50% charge loss. The S2 pulses are insensitive to the timing separation of the dual decay as electron diffusion smears the pulses two together as the electrons drift through the active region before extraction [57].



(a)  $^{83\text{m}}\text{Kr}$  event with 60 ns timing separation.



(b)  $^{83\text{m}}\text{Kr}$  event with 220 ns timing separation.

Figure 3.2: The S1 and S2 of two  $^{83\text{m}}\text{Kr}$  events. Top Figures (a): Show a  $^{83\text{m}}\text{Kr}$  event in which the two x-rays have overlapped within 60 ns, the S2 arrives about 93  $\mu\text{s}$  later. Bottom Figures (b): Show a  $^{83\text{m}}\text{Kr}$  event in which the two x-rays have overlapped within 220 ns, the S2 arrives about 205  $\mu\text{s}$  later. The LUX pulse finder classifies events within a 1  $\mu\text{s}$  window as a single S1. The S2 pulses are insensitive to the timing separation of the dual decay as electron diffusion smears the pulses two together as the electrons drift.

The  $^{83m}\text{Kr}$  source is introduced when needed into the LUX detector by flushing the charcoal housing with xenon and diverting the flow inline with the main circulation path. The  $^{83m}\text{Kr}$  source and delivery into the xenon detector is described in more detail in [62]. The relatively short half-life of 1.8 hours allows for several injections per week without interrupting WIMP search data taking. Once injected the source is uniformly mixed into the liquid xenon within a matter of minutes and can be used to calculate corrections for the XYZ the response of the detector. Decay of  $^{83m}\text{Kr}$  produces a well defined mono energetic peak as it decays in the xenon (shown in section 4). Tracking the peak vs. x,y,z allows for the detector's spacial dependent response to be gauged over the course of the science run. Figure 3.3 shows the uniform distribution of  $^{83m}\text{Kr}$  events in the LUX detector thirty minutes after the injection.

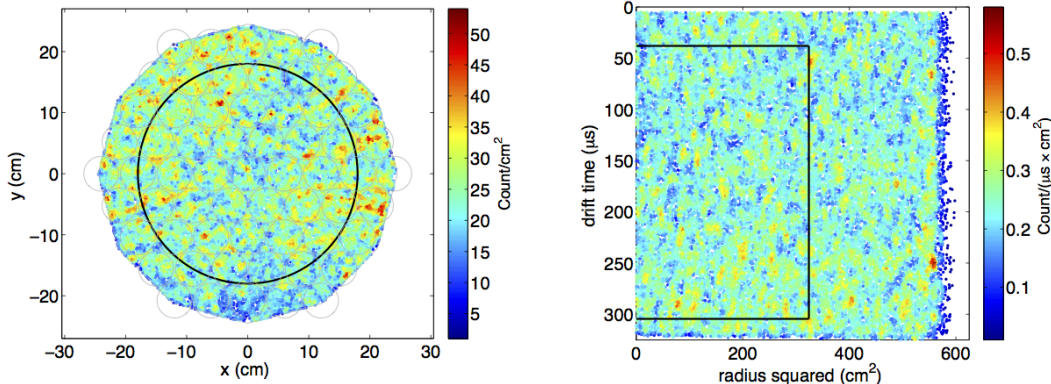


Figure 3.3: Distribution of  $^{83m}\text{Kr}$  events 10 minutes after the injection. The source mixes uniformly throughout the liquid xenon illuminating all regions of the active volume. The solid black lines represent the fiducial volume used for the WIMP search.

### 3.2 S2 Electron Lifetime and x,y Correction

As mentioned previously, the S1 and S2 signals collected on the top and bottom PMT arrays have well defined x,y,z positions computed from the S2 hit pattern (x,y) and the signal separation in time (z). The dominant effect to correct the data for is the free electron lifetime, as charge is drifted from the event site to the extraction region (0-47 cm) electronegative impurities in the liquid latch onto them. These impurities include residual O<sub>2</sub>, H<sub>2</sub>O, N<sub>2</sub> in the xenon (1 ppb O<sub>2</sub> corresponds to a 100  $\mu$ s lifetime [ref]). Throughout the 2013 science run the electron lifetime was measured between 500 to 1000  $\mu$ s, or an attenuation length of 75 to 150 cm with a drift velocity of 1.51mm/ $\mu$ s. The measured electron lifetimes (or attenuation lengths) correspond to between 70% and 50% reduction in S2 signal from the cathode grid, the bottom of the active region.

The electron lifetime is calculated by binning the detector in drift time into 60 slices. In each bin a Gaussian is fit to extract the mean. Once the mean in each slice is calculated, an exponential is fit to the mean S2 response vs. z. The exponential time constant the measure of the characteristic drift time  $\tau$  [ $\mu$ s], shown in figure 3.4. The characteristic attenuation length is  $\lambda = \tau v_{drift}$ , where  $v_{drift}$  is the electron drift velocity. The electron lifetime extraction from a <sup>83</sup>Kr data set is shown in figure 4. For this analysis present S2 response on the bottom PMT array (S2<sub>b</sub>) as it was used for the preliminary WIMP search analysis discussed in ???. Corrections for top only, bottom only, and all PMTs are computed for each <sup>83m</sup>Kr calibration data set.

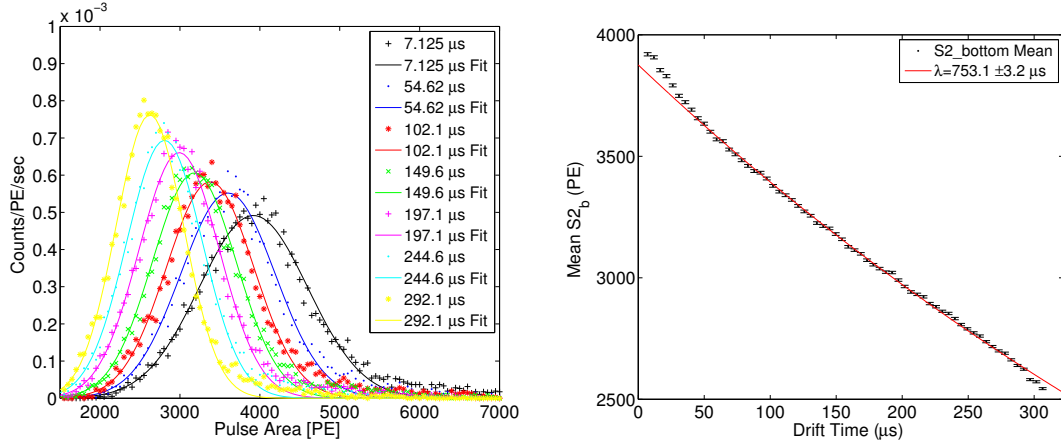


Figure 3.4: Left: Fits to the mean of  $S2_b$  in several  $z$  slices. Right, the exponential fit to the means of  $S2_b$  vs. drift time used to extract electron lifetime  $\lambda$ .

The  $z$  corrected  $S2_b$  from each signal is calculated as follows:

$$S2_{b-z} = S2_b \cdot \exp\left(\frac{\text{drift time}[\mu\text{s}]}{\tau[\mu\text{s}]}\right) \quad (3.1)$$

Where  $S2_{b-z}$  is the  $z$  corrected  $S2_b$  signal and  $\tau$  is the free electron lifetime. After correcting the dominant  $z$  dependent electron attenuation, corrected to 0 drift time, we calculate the normalization factor ( $\mathcal{N}\mathcal{F}$ ) that will be used to correct the  $x,y$  dependence of the  $S2$  signal. The  $S2$  light is emitted when the charge is extracted from the liquid above the gate and is accelerated by a 6 kV potential to the anode, traversing 5mm. Fluctuations in  $x,y$  response to a given number of electrons are caused by non uniformities in the extraction field, tilt in the liquid level, and non uniformities in the anode-gate separation (potentially wire sagging). All these variations lead to additional fluctuations in the  $S2$  signal, by using a the  $^{83m}\text{Kr}$  the response can be corrected as a function of  $x,y$  position. The normalization is calculated by creating a 25x25 grid on the  $x,y$  plane, corresponding to 2[cm] x 2[cm]  $x,y$

bins, for each bin center the average light response is determined by fitting a Gaussian. Figure 3.5 on the left, shows the measured S<sub>2b</sub> response to 1 million <sup>83m</sup>Kr decays normalized to the response at the center, x=y=0, this map represents the inverse of the normalization factor that we call  $\mathcal{N}\mathcal{F}(x, y)$ .  $\mathcal{N}\mathcal{F}$  is then applied to the S<sub>2b</sub> data by using a spline interpolation of the x,y coordinate of each event relative to the bin centers  $\mathcal{N}\mathcal{F}(x, y)$ . Figure 3.5 on the right, shows the S<sub>2b</sub> response after correcting the data relative to the center x=y=0 using  $\mathcal{N}\mathcal{F}(x, y)$ . After applying the x,y correction the fluctuation decrease from 10% to 1% in the inner 18 cm of the detector (the fiducial volume).

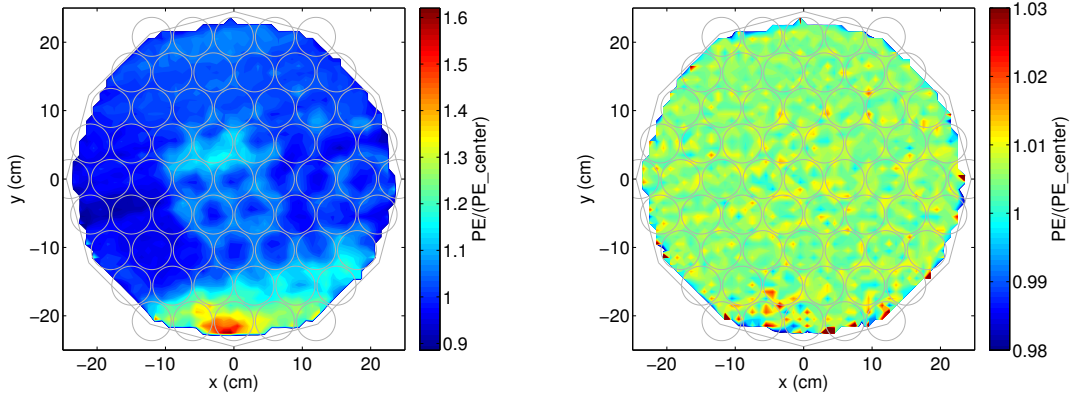


Figure 3.5: Left: Response of S<sub>2b</sub> vs. x,y normalized to the response at the center (x=y=0). Right: Response of S<sub>2b</sub> vs. x,y after correcting the data using  $\mathcal{N}\mathcal{F}_{S_{2b}}$ .

After correcting for z and x,y we can define the position dependent (x,y,z) corrected S<sub>2b</sub> signal, which we will call S<sub>2bc</sub> calculated as follows:

$$S_{2bc} = S_{2-(x,z,y)} = S_{2-z} \cdot \mathcal{N}\mathcal{F}_{S_{2b}}(x, y) \quad (3.2)$$

Where S<sub>2bc</sub> is the x,y,z corrected S<sub>2b</sub> signal and  $\mathcal{N}\mathcal{F}_{S_{2b}}(x, y)$  is the Normalization Factor of the bottom PMT array for S<sub>2s</sub> and is a function of x,y. The

interpolation of the inverse of  $\mathcal{N}\mathcal{F}_{S2_b}(x, y)$  along the x,y grid is plotted in figure 3.5.

After applying the z correction to S2<sub>b</sub> there is an improvement in resolution of 18%, for the case of an 750  $\mu$ s electron lifetime. The correcting in the x,y plane provides an additional 4.9% improvement in resolution to the S2<sub>b</sub> signal. Figure 3.6 shows the improvement in the S2<sub>b</sub> signal after applying the z and x,y correction.

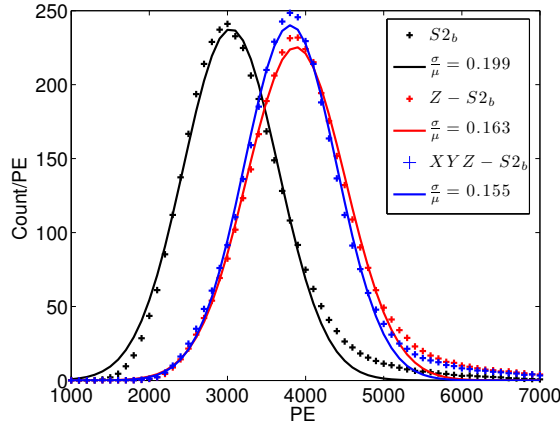


Figure 3.6: Improvement of resolution in S2<sub>b</sub> after applying the z and x,y,z correction.

### 3.3 S1 x,y,z Correction

The S1 light propagates from the interaction sight, unlike the S2, and has about a 30% variation in light collection efficiency between events near the top and bottom of the detector. About 2/3 of the S1 light is collected on the bottom PMT arrays due to total internal reflection at the liquid gas interface, and as events move closer to the bottom PMTs the probability of a photon striking a PMT and producing a photo electron (PE) increases. Other position dependent effects include the photon

absorption length which is negligible at the purities achieved in LUX and teflon reflectivity, about 95%. Any quantum efficiency (QE) variations between the 122 PMTs that are properly normalized by the individual gain corrections are also folded into the S1 position dependent correction, measured from the  $^{83\text{m}}\text{Kr}$  calibrations. To calculate the x,y,z dependent Normalization Factor for S1 ( $\mathcal{N}\mathcal{F}_{\text{S1}}$ ) the detector is divided into a 25x25x16 x,y,z mesh with each voxel having dimensions of 2[cm] x 2[cm] x 20[ $\mu\text{s}$ ]. To achieve sufficient statistics for correcting we require at least 400,000  $^{83\text{m}}\text{Kr}$  events, giving about 40 events per voxel to define the mean. However, we perform monthly high stats calibrations that produce 1 million counts providing precise  $\mathcal{N}\mathcal{F}$  correction maps. Unlike the S2 correction, which is highly dependent on purity, the S1 has been found to be invariant to within a percent over the course of the science run, thus monthly calibrations with high stats are sufficient to provide the position dependent correction.

Figure 3.9 shows the response of the detector to  $^{83\text{m}}\text{Kr}$  normalized to the center of the detector in 16 slices of z, each with a 2[cm] x 2[cm] x,y grid. The plotted maps and normalized to the center of the detector and represent the inverse of the normalization factor ( $\mathcal{N}\mathcal{F}_{\text{S1}}$ ). We choose to normalize the the center of the detector as it represents the overall average light collection efficiency of the detector as this value varies roughly linearly from top to bottom, with lower light collection at the top and higher light collection at the bottom. Though the dominate correction is the z dependance there is also substructure to each z slice in x,y which is illustrated in figure 3.8, where we have normalized each slice to its own center. Plotting in this way it is evident that near the top and bottom there are additional geometric

effects near the edges, whereas in the central z slices the uniformity in x,y is much better due to increased scattering off the teflon.

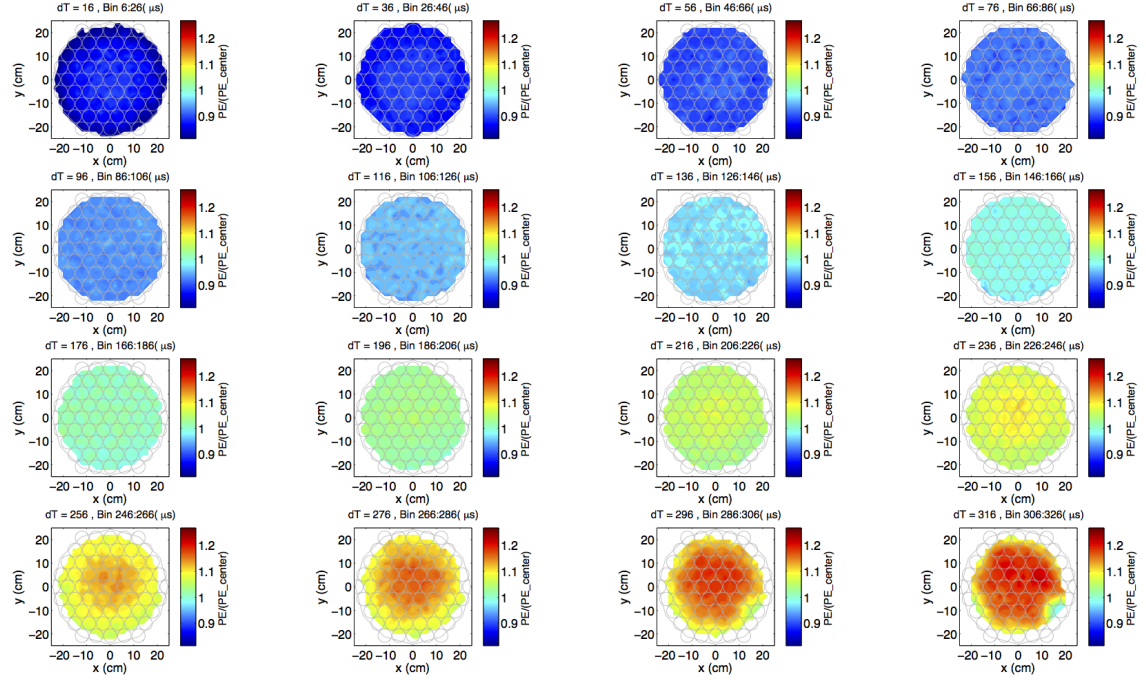


Figure 3.7: S1 x,y,z response normalized to the center of the detector. The interpolated map represents the inverse of the normalization factor  $\mathcal{N}\mathcal{F}$ .

We define the position dependent (x,y,z) corrected S1 signal as  $S1_c$ , normalized to the center of the detector ( $x=y=0$  and  $z=160\mu s$ ) calculated as follows:

$$S1_c = S1_{(x,z,y)} = S1 \cdot \mathcal{N}\mathcal{F}_{S1}(x, y, z) \quad (3.3)$$

Where  $S1_c$  is the x,y,z corrected S1 signal and  $\mathcal{N}\mathcal{F}_{S1}(x, y, z)$  is the Normalization Factor of the sum of all PMTs for S1s and is a function of x,y,z. The interpolation of the inverse of  $\mathcal{N}\mathcal{F}_{S1}(x, y, z)$  along the x,y grid in z slices is plotted in figure 3.9. The normalization factor is applied to the S1 data by using a spline interpolation of the x,y,z coordinate of each event relative to the bin centers

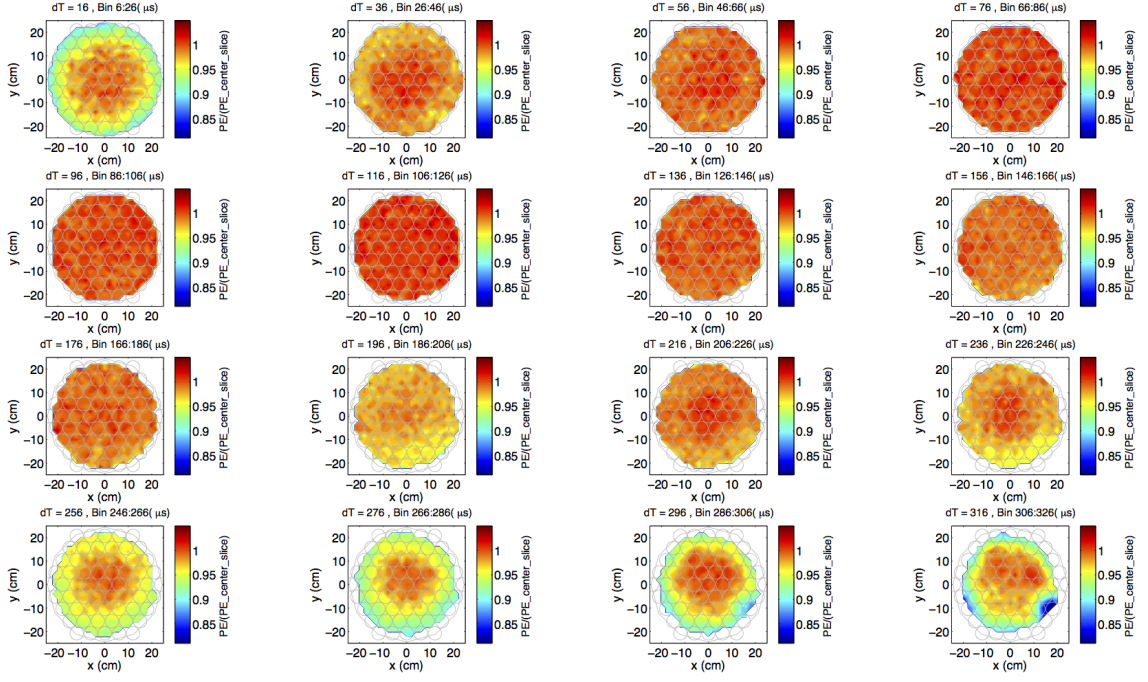


Figure 3.8: S1 x,y,z response normalized to the center of each z slice. There are greater variations near the very top and bottom 4 z slices as the solid angle for light hitting the PMT arrays are increased. For the central slices the x,y response is uniform due to increased scattering off the teflon panels.

$\mathcal{N}\mathcal{F}_{S1}(x, z, y)$ . Figure 3.9 shows the S1 response after correcting the data relative to the center of the detector. After applying the x,y,z correction the position dependent fluctuations decrease to less than 1% in the inner 18 cm of the detector (the fiducial volume), with as much as 3% fluctuations near the top and bottom edges were the interpolation breaks down.

After applying the z correction to S1 there is an improvement in resolution of 31.5%. The correcting in z and the x,y plane provides an additional 2.0% improvement in resolution in S1 over the z only correction. Figure 3.10 shows the improvement in the S1 signal after applying the z and x,y,z correction.

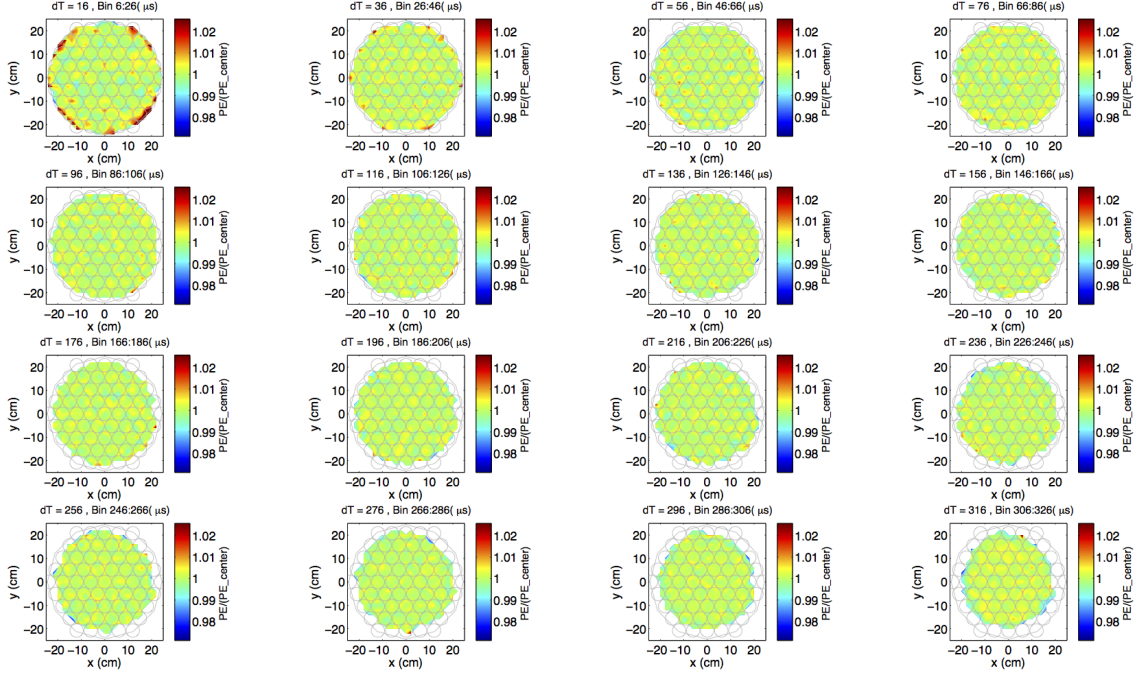


Figure 3.9: S1 x,y,z response normalized to the center of the detector after the data has been corrected and normalized to the detector center. The remaining fluctuations in the fiducial volumes ( $r < 18\text{cm}$ ) are less than 1%, near the top and bottom edges the deviation increases to as much as 3% due to the interpolation of the correction breaking down.

### 3.4 Application to x,y,z Corrections in Data Processing

As mentioned earlier, the purpose of the periodic  $^{83\text{m}}\text{Kr}$  calibrations were to produce position dependent S1 and S2 corrections over the corse of the science run. Before processing the WIMP search data the calibration sets were processed and a MySQL table of electron lifetimes and corrections maps were populated for each date. The electron lifetime applied to each WIMP search data set was a linear interpolation between calibration dates, for the x,y correction the nearest  $\mathcal{N}\mathcal{F}_{\text{S}2}(x, y)$  entry in

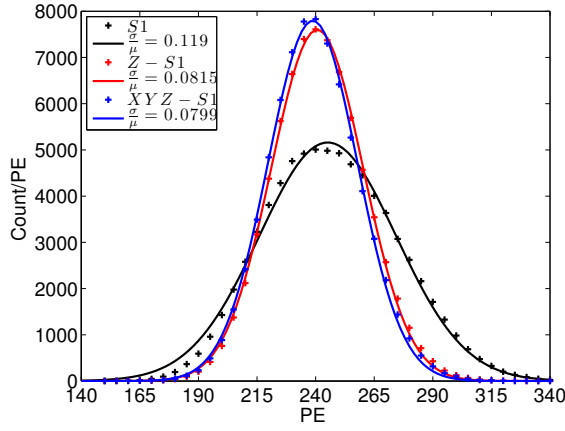


Figure 3.10: Improvement of resolution in S1 after applying the z and x,y,z correction.

time was used. Combined these produced the corrected  $S2_c$  quantity to be used for the WIMP analysis. For the S1 x,y,z corrections the nearest  $\mathcal{N}\mathcal{F}_{S1}(x, y, z)$  entry was used to produce the corrected  $S1_c$  quantity. For both the  $S2_{-x,y}$  and  $S1_{-x,y,z}$  correction the time dependance is assumed to be negligable as these are geometric effects, whereas the electron lifetime varies with purity daily. The electron lifetime and the stability of the z dependent S1 correction over the corse of the first science run is shown in figure 3.11 and 3.12. While the electron lifetime needs frequent monitoring the S1 x,y,z response is fixed over several months of running. For the results discussed in the subsequent sections of the thesis we will only work with the x,y,z corrected S1 and  $S2_b$  pulses defined at  $S1_c$  and  $S2_{bc}$  respectively.

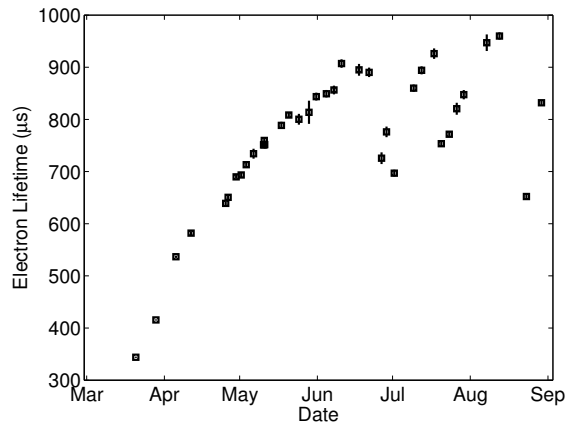


Figure 3.11: Electron lifetime measured using  $^{83m}\text{Kr}$  calibrations over the course of the LUX science run in 2013.

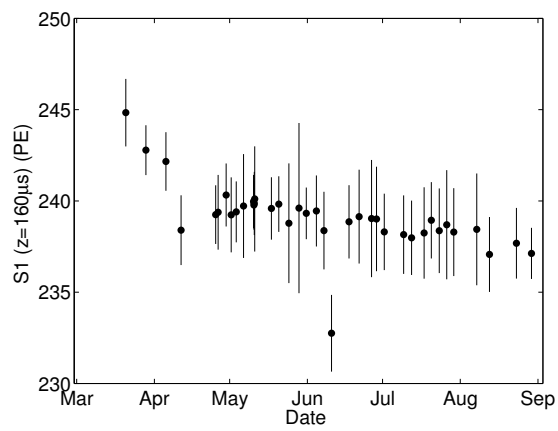


Figure 3.12: Measured response of to light from  $^{83m}\text{Kr}$  calibrations at the center of the LUX detector over the course of the LUX science run in 2013.

## Chapter 4: Energy Scale Calibration

### 4.1 Calibrating the Combined Energy Scale

This section outlines the method used to calibrate the energy scale of the dual phase LUX detector. The idea behind the method is to take calibration data with multiple sources and/or electric fields and combine the measured scintillation signals, primary (S1) and secondary (S2) in order to reconstruct energy. For a given energy deposit in liquid xenon an amount of quanta released is proportional to a work function  $W$ , for nuclear recoils we must also consider heat loss. The quanta created at the interaction site are the results of electron-ion pairs and exitons produced by the recoiling xenon nucleus, equation 4.1. Exitons quickly de-excite and contribute to the primary scintillation signal (S1). Ions that recombine with their electron pairs produce scintillation light (S1), while those electrons that do not recombine are collected several  $\mu\text{s}$  later in the extraction region as the larger secondary scintillation signal S2. There are two knobs to turn that tune the recombination fraction and probe combined energy space over a variety of S1 and S2, we can either change the energy of the source or adjust the drift field. The larger the spread in S1 and S2 the more constrained the combined energy scale will be. Measuring both light and charge allows for a vastly improved resolution compared with only using a

single S1 or S2 only space, since recombination fluctuations cancel out if energy is reconstructed correctly.

$$\begin{aligned} E &= W(n_i + n_{ex}) \\ E &= W(n_\gamma + n_e) \end{aligned} \quad (4.1)$$

Using equation 4.1 and assuming that the heat loss is negligible for electronic recoils (ER) we can reconstruct energy by knowing the work function and the conversion from measured S1(light) and S2(charge) signals to the number of quanta ( $n_\gamma + n_e$ ) liberated by the interaction. We define gain-1 ( $g_1$ ) and gain-2 ( $g_2$ ) as the conversion from initial number of photons and electrons propagated from the interaction site to the observed signal by the PMT arrays as a photo electron (PE), given in equation 4.2. By using multiple mono energetic sources with known energies we can extract a best fit for the value of the gains ( $g_1, g_2$ ) by making a Doke plot [ref]. The mono energetic lines used for the purposes of the calibration are listed in table 4.1. For each calibration point we plot the mean  $S1/E$  vs. mean  $S2/E$  (Equation 4.3) and fit a line, the x and y intercepts (Equation 4.4) yields the value of  $g1/W$  and  $g2/W$  respectively. The value of the work function  $W$  in liquid xenon has been found to be  $0.0137 \pm 0.002$  [quanta/keV] [ref]. The values of  $g1, g2$  are degenerate and highly correlated such that the ratio of  $g1:g2$  is always a constant, a reduction in  $g1$  can be compensated by an increase in  $g2$  and still yield the same number of initial quanta and visa versa. Breaking the degeneracy requires data over a wide range of  $S1$  and  $S2$  values near the intercept of the Doke plot. Due to the

strong correlation in the fit parameters the data is fit by minimizing the likelihood and the errors in intercept and slope are determined using MCMC (Markov Chain Monte Carlo).

$$\begin{aligned}\langle n_\gamma \rangle &= \frac{\langle S1 \rangle}{g_1} \\ \langle n_e \rangle &= \frac{\langle S2 \rangle}{g_2}\end{aligned}\tag{4.2}$$

$$\begin{aligned}S1/E &= \frac{n_\gamma}{(n_\gamma + n_e)} \times \frac{g1}{W} \\ S2/E &= \frac{n_e}{(n_\gamma + n_e)} \times \frac{g2}{W}\end{aligned}\tag{4.3}$$

$$\begin{aligned}1 &= \left(\frac{S1}{E}\right) \left(\frac{W}{g1}\right) + \left(\frac{S2}{E}\right) \left(\frac{W}{g2}\right) \\ \left(\frac{S1}{E}\right) &= \left(\frac{g1}{W}\right) - \left(\frac{S2}{E}\right) \left(\frac{g1}{g2}\right) \\ y = \frac{S1}{E}, x = \frac{S2}{E}, y &= m \cdot x + b \\ g1 &= b \cdot W \\ g2 &= \frac{g1}{m} = \frac{b \cdot W}{m}\end{aligned}\tag{4.4}$$

### 4.1.1 Anti-Correlation Space

The first step in calibrating the energy scale is to plot the observables S1 vs. S2, by doing this the anti correlation between light and charge at a given energy become apparent, figure 4.1. For the data presented here a fiducial cut was placed at a radius of less than 18 [cm] and drift distance between 6 and 46 [cm] which greatly reduces

Source	Energy [keV]	Decay Type
Xe K shell	29.7, 34	X-ray
$^{83m}\text{Kr}$	41.55**	Internal Conversion
$^{131}\text{Xe}$	163.9	Internal Conversion
$^{127}\text{Xe}$	203 or 375	$^{127}\text{I}$ daughter $\gamma$ -emission
	33.8	Kb shell X-ray
	5.3	L shell X-ray
$^{129m}\text{Xe}$	236.1	Internal Conversion
$^{214}\text{Bi}$	609	$\gamma$ -emission
$^{137}\text{Cs}$	661.6	Photo-absorption

Table 4.1: Mono energetic peaks used for g1 g2 calibration. \*\* Kr83 data was taken at 50 and 105 [V/cm] along with the standard field of 180 [V/cm].

the background event rate. To extract g1 g2 we first determine the average values of S1 and S2 at each known energy. Initially loose diagonal cuts are placed by eye on the populations, figure 4.1. Next, using a un-binned maximum likelihood fit the mean and sigma are estimated and then refit using  $\pm 2\sigma$  of the initial distribution to remove tails from backgrounds. With the initial estimate for the mean S1 and S2 response to a given energy the gains g1,g2 are determined. The resulting value of g1 and g2 is found to be  $0.096 \pm 0.009$  and  $5.94 \pm 1.68$  respectively, the fit is shown in figure 4.2. The values of g1 and g2 represent a best fit to the underlying recombination theory where for each additional photon there is a corresponding reduction of one electron and visa versa. The method for extracting the uncertainties using MCMC will be discussed later in section 4.1.3.

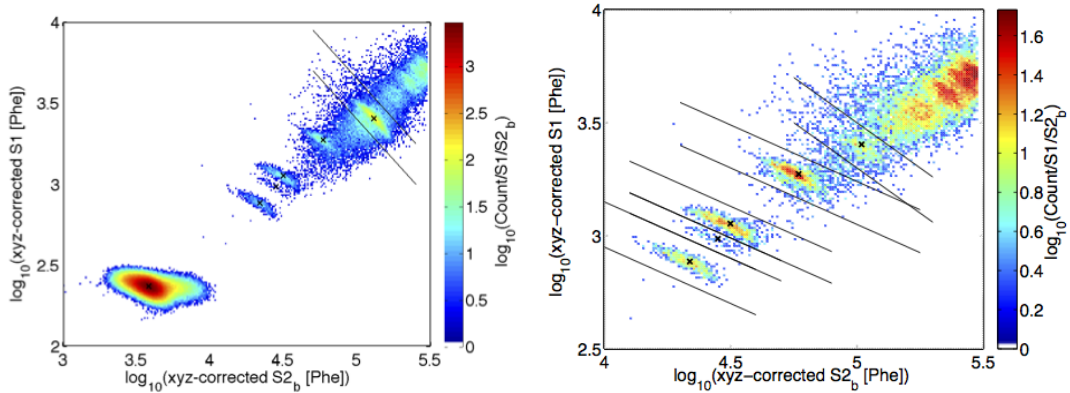


Figure 4.1: LUX data in anti correlation space (S1 vs. S2), the black lines indicate the initial cuts by eye used to isolate populations of constant energy. In both figures diagonals represent lines of constant energy with a slope depending on the local recombination probability. The centroids found by an unbind maximum likelihood analysis are shown as a black X, for sources show in table 4.1.

#### 4.1.2 Refitting in Combined Energy Space

From the first attempt to find  $g_1, g_2$  we see, in figure 4.2, that there are discrepancies between the data and the fit, however this first result is only a crude estimate derived from anti correlation space. Once we have an initial estimate of gains  $g_1, g_2$  a combined energy scale can be constructed with significantly improved resolution over the initial guess, due to the fact that recombination fluctuations are canceled. With the improved resolution the data are fit around the combined energy peaks using an unbinned maximum likelihood fit to a normal distribution, and then the data refitted around  $1.5 \sigma$  of the initial fit. The fits used to extract the means and sigmas of the S1 and S2 signals at a given energy are shown in figures 4.4 and

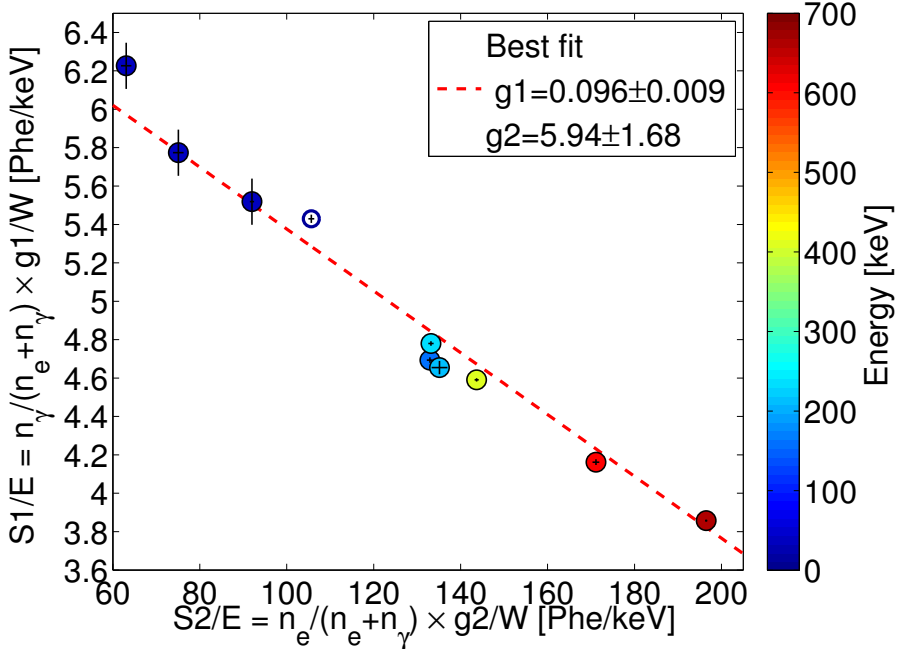


Figure 4.2: Doke plot showing the best fit for the energy calibration parameters  $g_1$  and  $g_2$  using  $S_1$  and  $S_2$  means extracted from anti-correlation space. The first three blue points, from the left, are from  $^{83}\text{Kr}$  calibrations at 50, 105 and 180 V/cm respectively. The open circle was from the K-shell xenon X-ray and was not used for the fit as it's absolute energy and origin from the skin of the detector is uncertain.

4.5. We iterate this technique twice as the convergence is rapid, in this case the initial value of  $g_1$  and  $g_2$  derived from anti-correlation space are already a close approximation to the true value. The resulting value of  $g_1$  and  $g_2$  is found to be  $0.097 \pm 0.008$  and  $5.75 \pm 1.4$  respectively, the fit is shown in figure 4.3. After refitting there is a significant improvement over figure 4.2, especially the xenon activation lines in the center, which is due to better peak finding in combined energy space over anti-correlation space.

$$g1 = 0.097 \pm 0.008 \quad (4.5)$$

$$g2 = 5.75 \pm 1.4$$

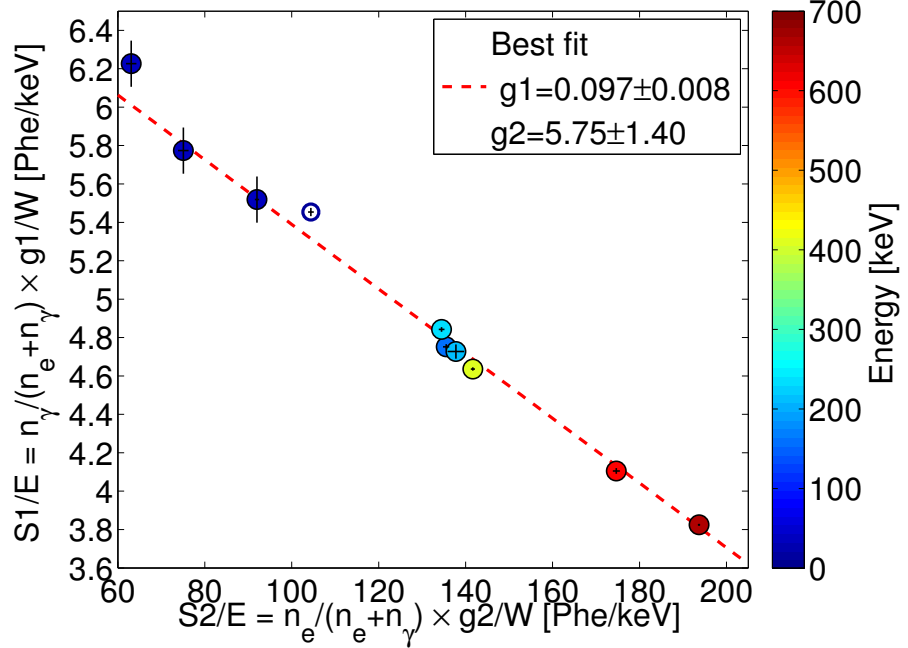


Figure 4.3: Doke plot showing the best fit for the energy calibration parameters  $g_1$  and  $g_2$  using  $S_1$  and  $S_2$  extracted from a combined energy space. The first three blue points, from the left, are from  $^{83}\text{Kr}$  calibrations at 50, 105 and 180 V/cm respectively. The open circle was from the K-shell xenon X-ray and was not used for the fit as it's absolute energy and origin from the skin of the detector is uncertain.

Figure 4.6 is the final Doke plot for multiple peaks the theory describes the data well using the optimal fit for  $g_1$  and  $g_2$ , for each increase in number of photons there is a corresponding decrease in the number of electrons and visa versa. The relatively large error on  $g_2$  is due to the distance of the data points from the x-intercept. As stated before the values of  $g_1$  and  $g_2$  can be locally degenerate as long

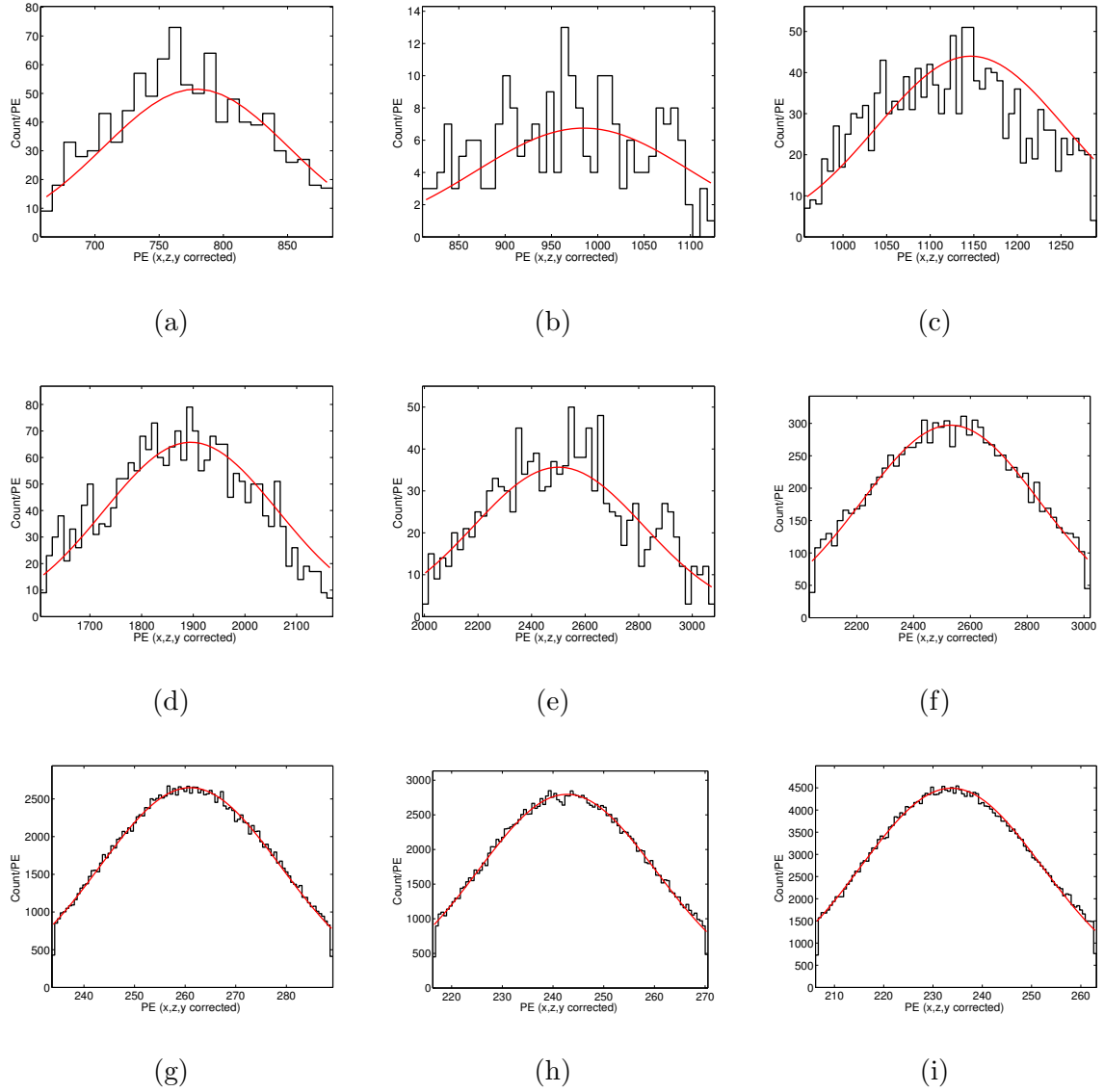


Figure 4.4: S1 fits to sources at nominal field of 180 [V/cm] unless otherwise noted.

Source and energy in keV from top left to bottom right: a)  $^{131}\text{Xe}$ : 163, b)  $^{127}\text{Xe}$ : 207, c)  $^{127}\text{Xe} \& ^{129\text{m}}\text{Xe}$ : 236.8, d)  $^{127}\text{Xe}$ : 410, e)  $^{214}\text{Bi}$ : 609, f)  $^{137}\text{Cs}$ : 661.6, g)  $^{83\text{m}}\text{Kr}$ : 41.5 - at 50 [V/cm], h)  $^{83\text{m}}\text{Kr}$  41.5 - at 105 [V/cm], i)  $^{83\text{m}}\text{Kr}$  41.5 .

as their ratio remains a constant. Thus for future studies it will be important to probe more of the parameter space in order to place a tighter constraint on gains g1 and g2.

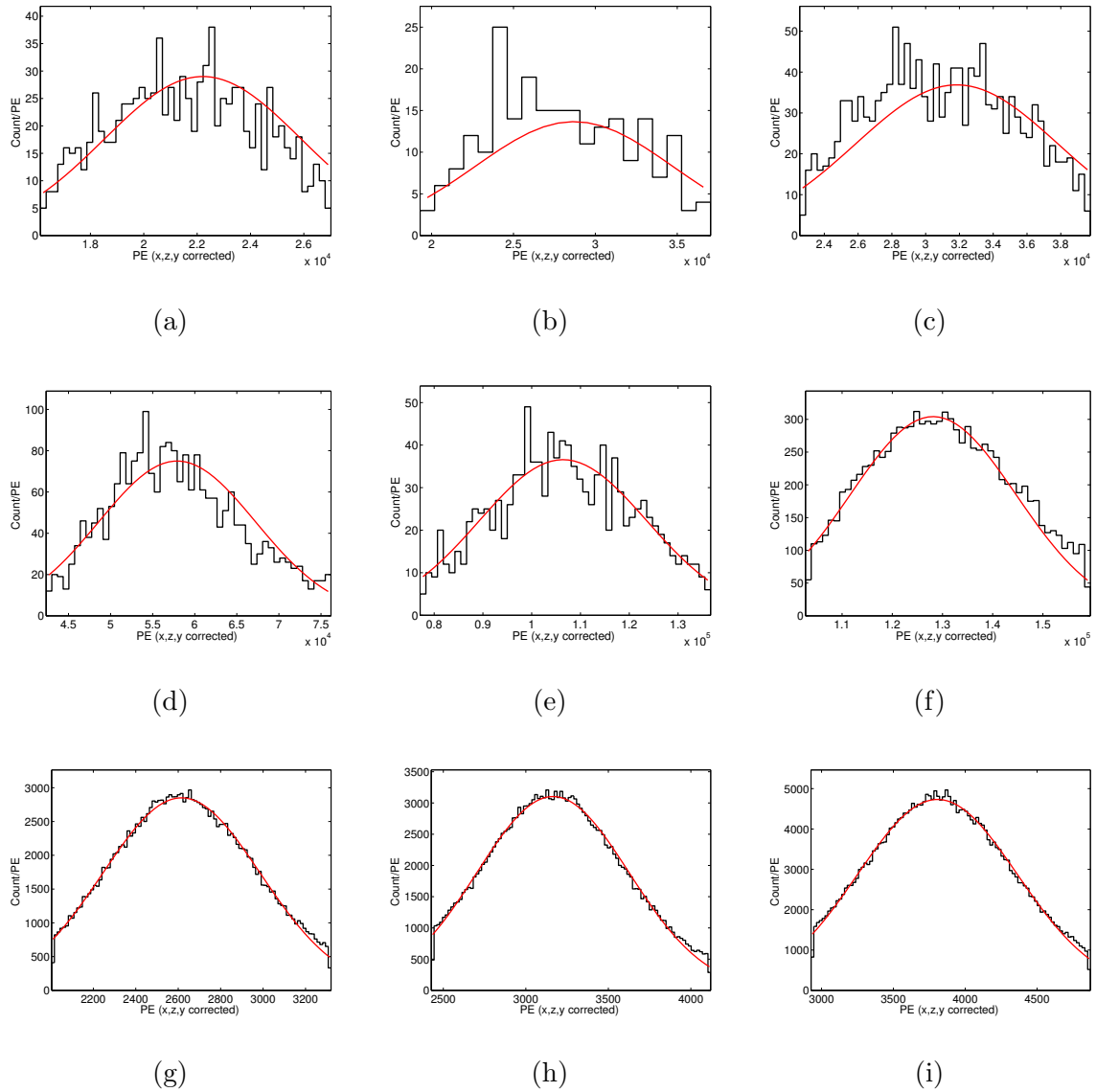


Figure 4.5: S2 fits to sources at nominal field of 180 [V/cm] unless otherwise noted.

Source and energy in keV from top left to bottom right: a)  $^{131}\text{Xe}$ : 163, b)  $^{127}\text{Xe}$ : 207, c)  $^{127}\text{Xe}$  &  $^{129\text{m}}\text{Xe}$ : 236.8, d)  $^{127}\text{Xe}$ : 410, e)  $^{214}\text{Bi}$ : 609, f)  $^{137}\text{Cs}$ : 661.6, g)  $^{83\text{m}}\text{Kr}$ : 41.5 - at 50 [V/cm], h)  $^{83\text{m}}\text{Kr}$  41.5 - at 105 [V/cm], i)  $^{83\text{m}}\text{Kr}$  41.5 .

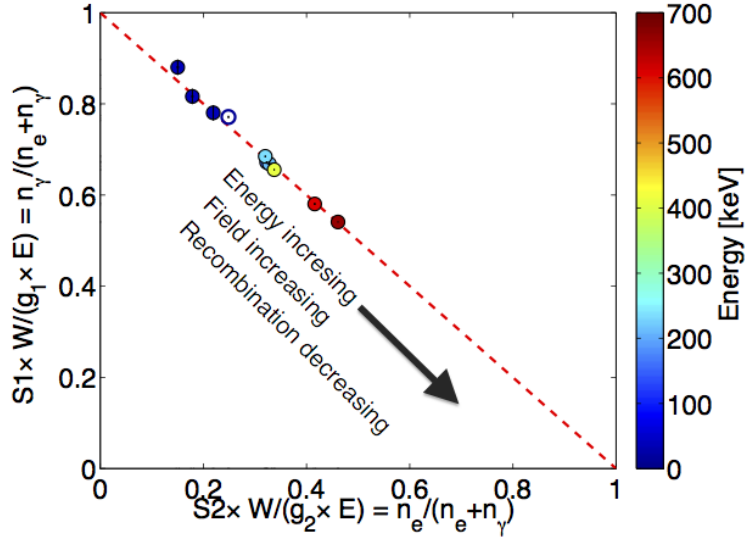


Figure 4.6: Doke plot of the data showing the light yield vs. charge yield. Only solid circles are used for the fit, the open circle is the Xe K shell X-ray from the detector edge.

#### 4.1.3 Finding Errors with MCMC

The error bars reported in this section on  $g_1$  and  $g_2$  are from the error in the slope and intercept of the linear fit in the Doke plot derived using MCMC. For calculating the error in slope and intercept three random walkers were used at each data point and allowed to take 500 steps. The MCMC takes into account the covariance of the parameters, shown in figure 4.7 as a two dimensional Gaussian. There is a strong negative correlation between the slope  $m$  and intercept  $b$  which is the result of the degeneracy between gains  $g_1$  and  $g_2$  used to reconstruct energy by combining the light and charge signal. Thus, the error on  $g_1$  and  $g_2$  is such that for the positive maxima deviation in  $g_1$  we reach the negative maxima of the error on  $g_2$ , and visa

versa. Using standard reduced  $\chi^2$  for fitting and calculating errors in the slope and intercept would be underestimated the true error by a factor of five as it does not account for the degeneracy of the anti-correlated gains.

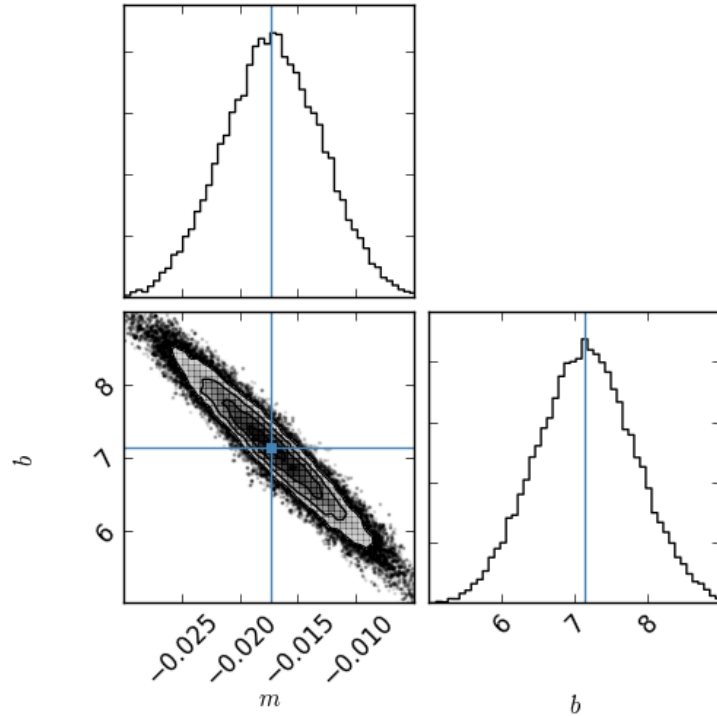


Figure 4.7: MCMC for the linear fit to the Doke plot. There is a strong negative correlation between the slope  $m$  and intercept  $b$  which results from the degeneracy between gains  $g_1$  and  $g_2$ .

#### 4.1.4 Combined Energy Space

With the values of g1 and g2 known the combined energy of events can be reconstructed with a significant improvement over using only the light or charge channel. In combined energy space recombination fluctuations are removed by the anti correlation of light and charge production and any residual smearing is due to intrinsic detector resolution (discussed later in section :). Figure 4.8 shows the energy histograms of the data used for the fits to gains g1 and g2 including the xenon activation lines and the  $^{137}\text{Cs}$  calibration, along with a zoom in of the xenon K shell Xray at 34 keV and a 81 keV gamma from  $^{133}\text{Xe}$ , not used for finding g1,g2. With the energy scale calibrated we can now reconstruct the energy of the events and convert the measured S1 and S2 signals to fundamental quanta using the gains g1,g2 allowing us to untangle instrumental and recombination fluctuations and measure light and charge yields.

#### 4.1.5 Light Collection and Electron extraction

The value of g1 represents the mean efficiency for collecting photons at the center of the LUX detector, the response to S1 light is flat fielded and normalized to the detector center (section Kr calibrations). The measured value of  $g1 = 0.097 \pm 0.008$  implies a 9.7% probability of a photon propagated from the center of the detector striking a PMT and being converting into a photo electron (PE) signal. The value of g2 represents the average number of PE collected for each electron that escaped recombination at the initial interaction site and then drifted,by the electric field,

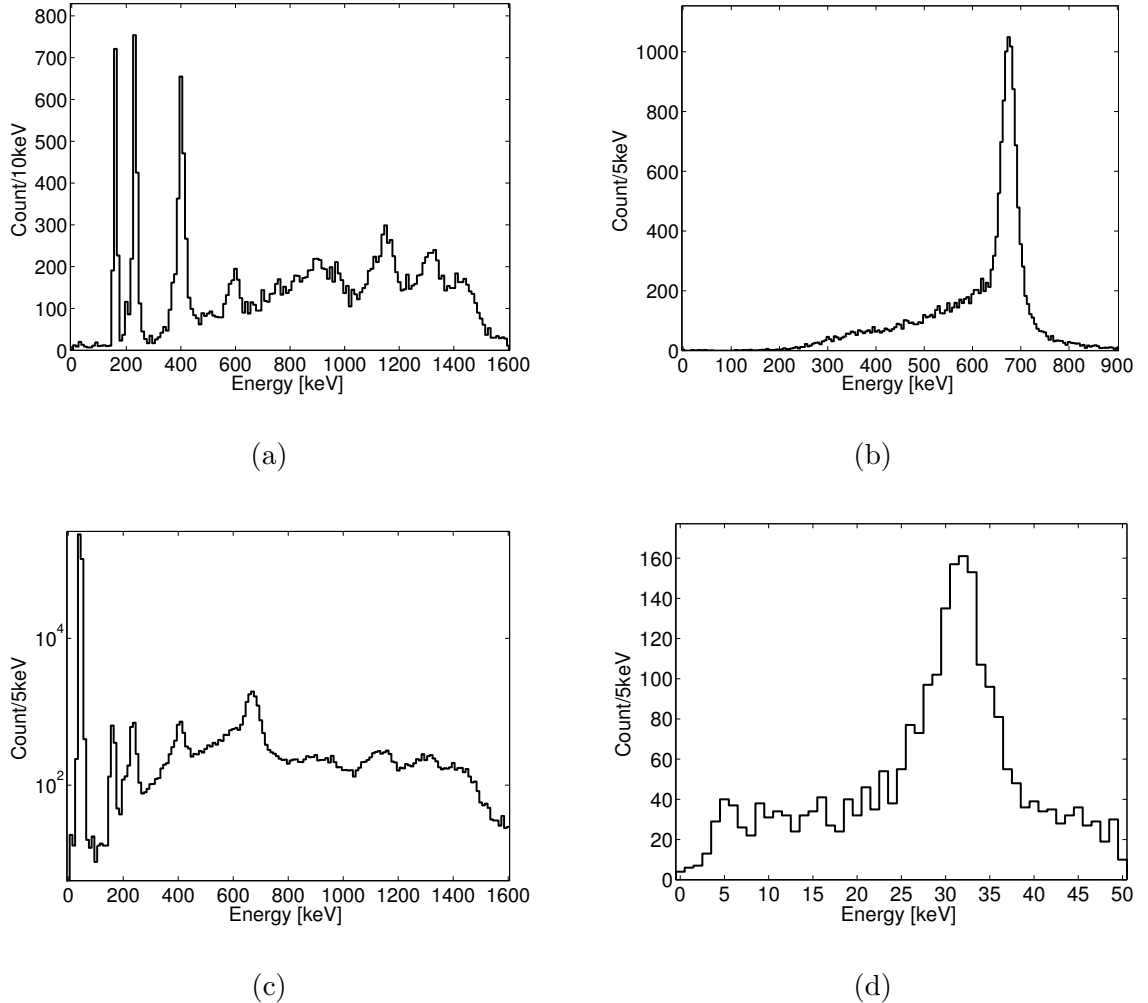


Figure 4.8: Combined energy scale. a) The xenon activation lines from early in the run. b)  $^{137}\text{Cs}$  calibration data. c) All calibration data including the  $^{83\text{m}}\text{Kr}$  calibration. d) Xenon X-ray.

towards liquid-gas interface where it is extracted. The S2 signals are corrected for depth as impurities exponentially attenuate electrons drifting through the xenon (section Kr cal). The value of  $g_2$  can also be thought of as the single electron size in PE, fortunately the LUX detector is low enough in threshold to observe single electrons being extracted from the liquid. Comparing the value of  $g_2$  derived from

the Doke method with the single electron size is a good sanity check on the energy scale calibration. As the electrons are extracted from the liquid they are accelerated by larger field between the gate and anode where they electro-luminesce, a single extracted electron creates tens to hundreds of photons which are collected by both PMT arrays. We can cut on the single electron population (small S2 pulses without an associated S1) and measure the single electron size along with the extraction efficiency efficiency. The extraction efficiency is defined as the probability that an election will be extracted from the liquid into the gas in a region of 3.5 kV between the anode and the gate. For a given event the extraction of electrons is a binomial processes with a rate approaching unity for fields above 5 kV (reference). Figure 4.9, shows the single electron size as measured by the bottom PMT array (used for S2 pulses in the LUX detector to avoid saturation). The population is modeled by a skew Gaussian due to the Poisson nature of measuring only a handful of photo electrons (PE) per extracted electron. The mean of the distribution is found to be 9.7 PE/e<sup>-</sup> with a width of  $\sigma_{SE} = 3.6$  Phe/e<sup>-</sup>. Thus, the extraction efficiency is g2 over the single electron size and is found to be  $(59.3 \pm 14)\%$ , given the extraction field the value is in good agreement with previous measurements in other xenon detectors -[2 refs extraction].

## 4.2 Modeling Intrinsic Detector Resolution

Intrinsic statistical fluctuations in light and charge (S1, S2) collection in the LUX detector lead to a spread in collected quanta. To measure effects from recombination

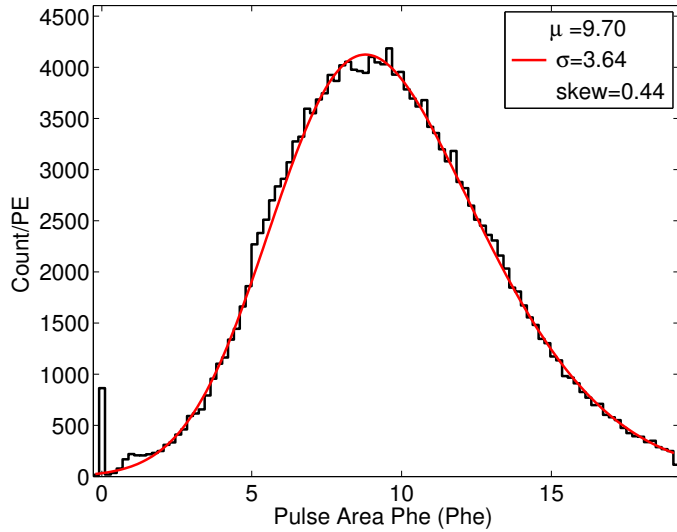


Figure 4.9: Single electron distribution as seen by the bottom PMT array fitted with a skew Gaussian model to account for the underlying Poisson statistics of observing between 9 and 10 photo electrons (PE) for each electron leaving the liquid and entering to the gas phase at a higher field causing electro-luminescence. The  $\mu$  of the fit represents the true mean of the skew Gaussian distribution.

fluctuations and the Fano factor we must first decouple the detector component of resolution. We use the model described in [Dahl's thesis] in which the measured scintillation and ionization signals S1, S2 (measured in Phe) are related to the number of photons and electrons produced for a given energy deposit are proportional to the average S1,S2 signals at a given drift field. The gain g1 represents photon detection efficiency, the probability of a photon from an energy deposit striking a PMT convolved with the quantum efficiency of the PMTs. Gain g2 represents the average S2 signal of a single electron normalized by the average single electron size. Where S2

uses only the bottom PMT array and is corrected for lifetime.

$$\begin{aligned}\langle n_\gamma \rangle &= \frac{\langle S1 \rangle}{g_1} \\ \langle n_e \rangle &= \frac{\langle S2 \rangle}{g_2}\end{aligned}\tag{4.6}$$

The statistical fluctuations for the measured number of quanta in equation 4.6 are from the statistical processes that comprise the measured S1 and S2 signal.

$$\begin{aligned}\sigma_{n_{\gamma_{\text{stat}}}}^2 &= \frac{\sigma_{S1_{\text{stat}}}^2}{g_1^2} \\ \sigma_{n_{e_{\text{stat}}}}^2 &= \frac{\sigma_{S2_{\text{stat}}}^2}{g_2^2}\end{aligned}\tag{4.7}$$

The variance in the number of photons in equation 4.7 can be broken into two parts. First, a binomial variance due to counting a fraction,  $g_1$ , of the initial photons produced.  $\text{Var}_{n_\gamma} = \frac{(1-g_1) \times g_1 \times n_\gamma}{g_1^2}$ . Second, the variance in the response of the PMTs to a single photon.  $\text{Var}_{n_\gamma} = \frac{g_1 \times n_\gamma \times \sigma_{\text{PE}}^2}{g_1^2}$ . Combining the two leads to the result in equation 4.8.

$$\sigma_{n_{\gamma_{\text{stat}}}}^2 = \frac{1 - g_1 + \sigma_{\text{PE}}^2}{g_1} n_\gamma\tag{4.8}$$

The variance in the number of electrons in equation 4.7 is comprised of the following statistical uncertainties. First, a binomial variance due to the extraction efficiency of electrons from the liquid-gas interface.  $\text{Var}_{n_e} = \frac{(1-\text{ext}) \times \text{Ext} \times n_e \times (\text{single}_E)}{g_2^2}$ , Ext is the electron extraction probability and single<sub>E</sub> is the single electron size in PE. Second, the variance in the response of the PMTs to a single electron.  $\text{Var}_{n_e} = \frac{\text{Ext} \times n_e \times \sigma_{\text{SE}}^2}{g_2^2}$ . Finally, the additional variance from electron attenuation is modeled as

a Poisson probability of electron capture in each Z slice of the detector. The variance from each Z slice depends of the average number of electrons that will be attenuated. The probability of attenuation at each slice in drift time T is  $P(T) = 1 - e^{-T/\tau}$ , where  $\tau$  for the data sets to be considered is 1000  $\mu s$ . The drift region considered in the fiducial volume is from 38 to 304.5  $\mu s$ . The average variance from events in the fiducial can be given by equation 4.9.

$$\sigma_{n_{e_{att}}}^2 = n_e \frac{\int_{T_{min}}^{T_{max}} (1 - e^{-T/\tau}) dT}{\int_{T_{min}}^{T_{max}} dT} = 0.155 \times n_e \quad (4.9)$$

Combining the variances leads to the the result for the statistical variance in the observed number of electrons equation 4.10.

$$\sigma_{n_{e_{stat}}}^2 = \frac{\text{Ext} \times \sigma_{SE}^2 + (1 - \text{Ext}) \times g2}{g2^2} n_e + \sigma_{n_{e_{att}}}^2 \quad (4.10)$$

For this analysis we use the following detector gains: 4.11.

$$g_1 = 0.097 \pm 0.008 \text{ [Phe/n}_\gamma\text{]}$$

$$g_2 = SE_b \times Ext = 5.75 \pm 1.4 \text{ [Phe/n}_e\text{]}$$

$$SE_b = 9.70 \pm 0.05 \text{ [Phe/n}_e\text{]}$$

$$\sigma SE_b = 3.64 \text{ [Phe/n}_e\text{]}$$

$$Ext = 0.593 \pm 0.144$$

$$\sigma_{PE} = 0.51 \text{ [Phe/n}_\gamma\text{]}$$

(4.11)

Combining equations 4.8-4.11 we find the intrinsic detector resolution for the average S1 and S2 signals in the LUX detector, equation 4.12. Note, the intrinsic resolution in S2 is subdominant to that of S1, since on average one electron multiplies to about ten photons detected by the bottom PMT array [ref]. Also listed in 4.13, are the instrumental fluctuations with a linear dependance on quanta measured with a global fit to mono energetic sources [next section]. The total variance in the light and charge channels is the linear combination of the statistical and instrumental variance.

$$\begin{aligned} \sigma_{n_{\gamma_{\text{stat}}}} &= 3.46\sqrt{n_\gamma} \\ \sigma_{n_{e_{\text{stat}}}} &= 0.68\sqrt{n_e} \end{aligned} \quad (4.12)$$

$$\begin{aligned}\sigma_{n_{\gamma_{\text{inst}}}} &= \frac{6.4 \pm 1.7}{100} \times n_{\gamma} \\ \sigma_{n_{e_{\text{inst}}}} &= \frac{6.6 \pm 0.9}{100} \times n_e\end{aligned}\quad (4.13)$$

$$\begin{aligned}\sigma_{n_{\gamma_{\text{Det}}}}^2 &= \sigma_{n_{\gamma_{\text{stat}}}}^2 + \sigma_{n_{\gamma_{\text{inst}}}}^2 \\ \sigma_{n_{e_{\text{Det}}}}^2 &= \sigma_{n_{e_{\text{stat}}}}^2 + \sigma_{n_{e_{\text{inst}}}}^2\end{aligned}\quad (4.14)$$

## 4.3 Measuring Recombination Fluctuations

### 4.3.1 Measuring Recombination Fluctuations with Mono-Energetic Sources

To model recombination we start with a basic assumption that for a given energy deposit in liquid xenon the number of quanta produced is equal to the number of exitons and the number of ions. The number of ions created contains a spread given by a Fano factor  $F$ . The value of  $F$  for liquid xenon is small, has a theoretical value of 0.05 [53].

$$\begin{aligned}\frac{E}{W} &= n_q = n_i + n_{ex} \\ \frac{E}{W} &= n_{\gamma} + n_e\end{aligned}\quad (4.15)$$

Where  $E$  is energy in [keV],  $W$  is the work function in [keV/quanta],  $n_q$  is the number of quanta,  $n_i$  is the number of ions and  $n_{ex}$  is the number of exitons. The theoretical value of the number of exitons produced to ions is  $\frac{n_{ex}}{n_i} = \alpha = 0.06$  and

is not expected to change vs. energy [47] [48] [46]. For the subsequent equations in this section we will simplify equations 4.15 to that in 4.16.

$$\alpha = 0.06$$

$$n_i = \frac{E}{W} \frac{1}{(1 + \alpha)} = \frac{n_\gamma + n_e}{(1 + \alpha)} \quad (4.16)$$

$$\sigma_{n_i}^2 = F \times n_i$$

Equation 4.16 gives us a simple model for the number of ions and exitons produced for a given interaction, the only spread in quanta thus far is due to a Fano factor governing the spread in initial quanta produced. We now convert ions and exitons to scintillation and ionization signals that are measured in the LUX detector, S1 and S2 respectively. The number of photons observed for a given energy deposit arise from the exitons that de-excite and from ions which recombine with freed electrons. The number of electrons corresponding to a given energy deposit will be equal to the number of ions that did not recombine with a freed electron.

$$n_\gamma = n_{ex} + n_i \times r = n_i \times (r + \alpha)$$

$$n_e = n_i \times (1 - r) \quad (4.17)$$

$$r = \frac{\frac{n_\gamma}{n_e} - \alpha}{\frac{n_\gamma}{n_e} + 1}$$

Where  $r$  represents the electron-ion recombination probability. A key measurable quantity is the size of recombination probability fluctuation  $\sigma_r$ . Since we measure  $n_\gamma$  and  $n_e$  as S1 and S2 signals and not ions and exitons, an additional variance arises from the ion-electron recombination fluctuations. These recombina-

tion fluctuations are dependent on the  $dE/dx$  of each individual electron produced making them much larger than the spread from the Fano factor. We now combine the uncertainties from the Fano factor, recombination and the statistical uncertainty from detector resolution ( $\sigma_{\text{Det}}$ ) and solve for the observed quantities given in 4.18:

$$\begin{aligned}\sigma_{n_\gamma}^2 &= \sigma_{n_{\text{ex}}}^2 + \sigma_{n_i}^2 r^2 + \sigma_r^2 n_i^2 + \sigma_{n_{\gamma_{\text{Det}}}}^2 = \sigma_{n_{\text{ex}}}^2 + n_i F(r^2) + \sigma_r^2 n_i^2 + \sigma_{n_{\gamma_{\text{Det}}}}^2 \\ \sigma_{n_e}^2 &= \sigma_{n_i}^2 (1 - r)^2 + \sigma_r^2 n_i^2 + \sigma_{n_{e_{\text{Det}}}}^2 = n_i F(1 - r)^2 + \sigma_r^2 n_i^2 + \sigma_{n_{e_{\text{Det}}}}^2\end{aligned}\quad (4.18)$$

For convenience we will work with  $n_i = (n_\gamma + n_e)/(1 + \alpha)$ , this convention is chosen because both the Fano factor and recombination fluctuations act on number of ions and also because the number of ions are linearly related to the initial energy deposit. Using a mono energetic source and combined energy(equation 4.15) we can measure  $\sigma_{n_\gamma}^2$  and  $\sigma_{n_e}^2$  and  $\sigma_E^2$ . Dropping the contribution form the Fano factor and the the number of exitons it can be shown that the value recombination fluctuations  $\sigma_R$  can be determined by rearranging equation 4.18, keeping in ming that  $\sigma E$  contains no recombination fluctuations. Where  $\sigma R$  is in units of quanta,  $\sigma_R = n_i \sigma_r$ .

$$\sigma_R^2 = \frac{1}{2} \left( \sigma_{n_\gamma}^2 + \sigma_{n_e}^2 - \frac{\sigma_E^2}{W^2} \right) \quad (4.19)$$

Where the spread in observed quanta  $\sigma_{n_\gamma}^2$  and  $\sigma_{n_e}^2$  result from a linear combination of the variance from detector resolution and recombination fluctuations.

$$\begin{aligned}\sigma_{n_\gamma}^2 &= \sigma_{n_{\gamma_{\text{Det}}}}^2 + \sigma_R^2 \\ \sigma_{n_e}^2 &= \sigma_{n_{e_{\text{Det}}}}^2 + \sigma_R^2\end{aligned}\quad (4.20)$$

We do not directly observe the fluctuation in number of photons and electrons, instead we measure the fluctuations in the corresponding S1 and S2. The fluctuation in the S1 and S2 signal when divided by the gains g1 g2 represent on average the fluctuation in photons or electrons due to detector resolutions (statistical and instrumental variance) combined with recombination fluctuations. 4.20.

$$\begin{aligned}\sigma_{n_{\gamma\text{Det}}}^2 &= \frac{\sigma_{S1}^2}{g_1^2} - \sigma R^2 \\ \sigma_{n_{e\text{Det}}}^2 &= \frac{\sigma_{S2}^2}{g_2^2} - \sigma R^2\end{aligned}\quad (4.21)$$

Combining equations 4.19 and 4.21 leads to the results in equation 4.22, which is a formula to directly measure recombination fluctuations using a mono energetic source.

$$\sigma_R^2 = \frac{1}{2} \left( \frac{\sigma_{S1}^2}{g_1^2} + \frac{\sigma_{S2}^2}{g_2^2} - \frac{\sigma_E^2}{W^2} \right) \quad (4.22)$$

Equations 4.22 and 4.21 gives us a method to measure recombination fluctuations along with fluctuations in  $n_\gamma$  and  $n_e$  due to intrinsic detector resolution, (will be discussed in the next section). It is important to note that  $\sigma_{n_\gamma}^2$ ,  $\sigma_{n_e}^2$  and  $\sigma_E^2$  are observable quantities when using a mono energetic source. The variance in combined energy does not contain variance from recombination fluctuations as those fluctuation occur along lines of constant energy. Note, we have dropped the contribution from the Fano factor and the spread is exitons as they are much smaller than recombination fluctuations or the variances from measuring light and charge intrinsic to the detector. The observed variance in the light and charge channels

(S1, S2) is the result of two compounded random processes. After the initial charge deposit the number of charge and light quanta undergo recombination fluctuations. Subsequently, as the light or charge is collected in the detector an additional variance from detector resolution occurs. The result is the sum of two random processes thus the variance are added.

### 4.3.2 Results with Mono Energetic Calibration Sources

Using equation 4.22 and 4.21 along with the measurements of g1 g2, we construct a combined energy and deconvolve the recombination fluctuations from variances in the light and charge channel of the detector. The result is shown in figure 4.10, the black white and red lines represent  $\sigma R$ ,  $\sigma n_{\gamma_{\text{Det}}}$ ,  $\sigma n_{e_{\text{Det}}}$ , respectively for sources listed in Table 4.1. A variance with a linear and root term is fit to the data and used to extract instrumental fluctuations and constrain the statistical fluctuations. The linear term corresponds to instrumental fluctuations and the root term corresponds to statistical fluctuations. Instrumental fluctuations go like the signal size and may potentially be due to ripples in the liquid surface caused by xenon bubbles or other systematics that are unaccounted for. The root term should result purely from counting photo electrons, described earlier. We find:

$$\begin{aligned}\sigma_{n_{\gamma_{\text{Det}}}}^2 &= \sigma_{n_{\gamma_{\text{Stat}}}}^2 + \sigma_{n_{\gamma_{\text{Inst}}}}^2 = (0 \pm 10 \cdot \sqrt{n_\gamma})^2 + ((6.4 \pm 1.8)/100 \cdot n_\gamma)^2 \\ \sigma_{n_{e_{\text{Det}}}}^2 &= \sigma_{n_{e_{\text{Stat}}}}^2 + \sigma_{n_{e_{\text{Inst}}}}^2 = (1 \pm 4 \cdot \sqrt{n_e})^2 + ((6.6 \pm 0.6)/100 \cdot n_e)^2 \\ \sigma_R^2 &= ((5.5 \pm 0.5)/100 \cdot n_q)^2\end{aligned}\quad (4.23)$$

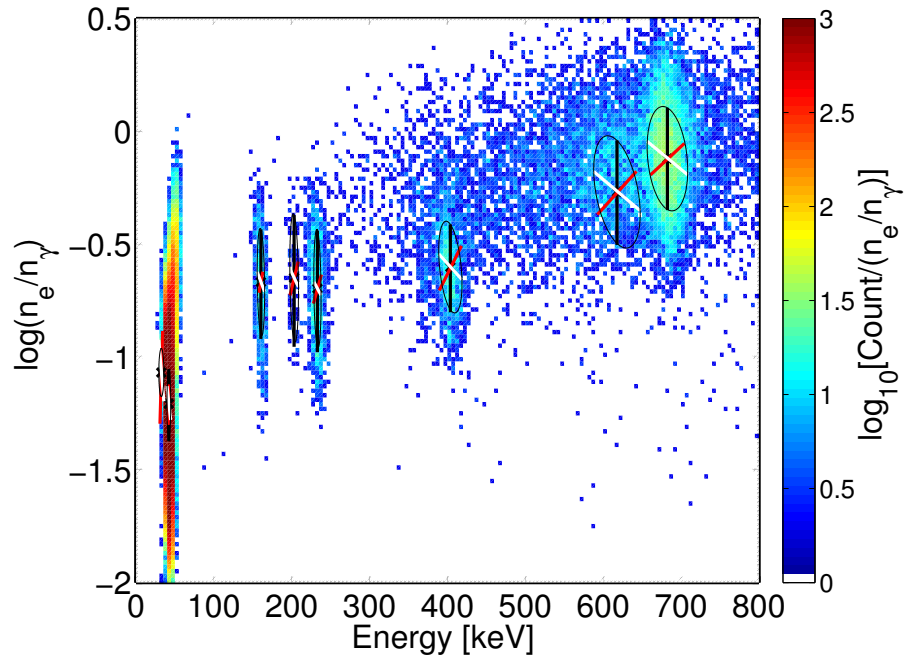


Figure 4.10: Populations of calibration sources in discrimination space  $\log\left(\frac{n_e}{n_\gamma}\right)$  vs. combined energy [keV<sub>ee</sub>]. The ovals represent the combination of  $\sigma R$ ,  $\sigma n_{\gamma\text{Det}}$ ,  $\sigma n_{e\text{Det}}$  in black, white, red respectively.

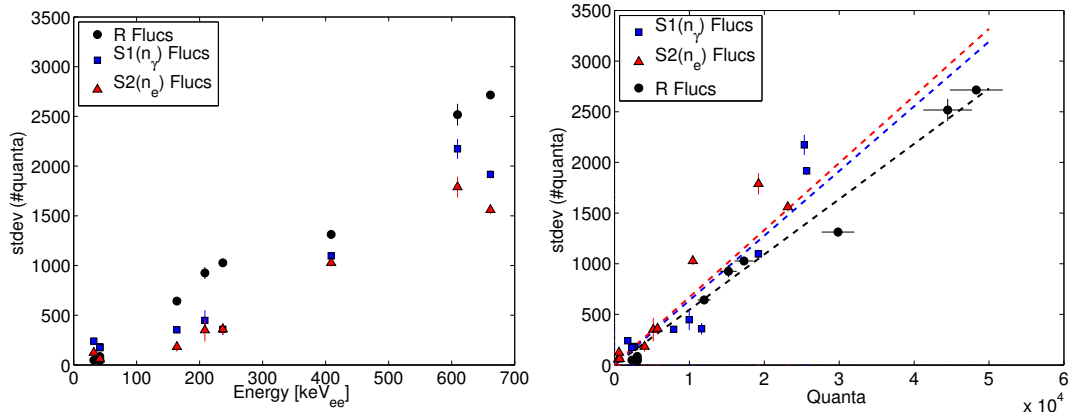


Figure 4.11: Measured values of  $\sigma R$ ,  $\sigma n_{\gamma\text{Det}}$ ,  $\sigma n_{e\text{Det}}$  vs. Energy on the left and vs. Quanta on the right. Measured using sources listed in Table 4.1.

### 4.3.3 Measuring Recombination Fluctuations in Desecrate Energy

#### Bins

The pervious subsection demonstrated the power of using a mono energetic source measure recombination fluctuations, equation 4.19. In this section we present a method to decouple statistical variance from recombination fluctuations when confined to an energy bin of width  $\Delta_E$ . The consideration of desecrate binning is crucial when dealing with a continual energy spectrum. Take the tritium beta spectrum as an example, we lose the ability to independently measure  $\sigma_{n_\gamma}^2$ ,  $\sigma_{n_e}^2$ ,  $\sigma_E^2$  and are only left with a smear of  $n_\gamma$ ,  $n_e$ ,  $E$ . However, there are two key pieces of information still left at our disposal. First, the combined energy can be reconstructed from global fits to  $g1$  and  $g2$ , and even corrected for spectral shape and detector resolution (discussed later in section [link]). Second, we can calculate values of statistical variance for the light and charge channels as a function of energy, described in 4.12, 4.13. It will be shown in this section that having a priori knowledge of  $g1, g2$  and the functional for of the statistical variance from detector resolution will be sufficient to measure recombination fluctuations for a continual energy spectrum binned in energy with width  $\Delta_E$ .

We begin the treatment of binning with the the case of having a finite bin width around the central combined energy of a mono energetic source. First, we quantify the change in the statistical components of equation 4.18 when slicing out a bin in combined energy space. The slice in combined energy is illustrated for a toy model at quanta corresponding to that of the combined 41.6 keV  $^{83}\text{Kr}$  decay

in Figure 4.12. All contribution from recombination fluctuations are included when slicing out a section of combined energy, illustrated in Figure 4.12. However, the slice contains only a reduced statistical component from both the light and charge signals, and in the limit that  $\Delta E$  goes to zero the statistical component of light and charge converge to a value defined as  $\chi_{\text{stat}}$  (where  $\chi$  is the measured  $\sigma$  in a bin of combined energy). To solve for the value of  $\chi_{\text{stat}}$  we first calculate the slope induced by statistical variance in the number of photons vs. quanta and the complementary slope of electrons vs. quanta, defined as  $M$  and  $1-M$  respectively. The value of  $M$  depends on the magnitude of the statistical variances and is given in equation 4.24. The sum of the two slopes must equal one as the sum of photons and electors make up combined energy.

$$M = \tan(\theta_{n_{\gamma_{\text{Det}}}}) = \frac{\sigma_{n_{\gamma_{\text{Det}}}}^2}{\sigma_{n_{\gamma_{\text{Det}}}}^2 + \sigma_{n_{e_{\text{Det}}}}^2} \quad (4.24)$$

$$1 - M = \tan(\theta_{n_{e_{\text{Det}}}}) = \frac{\sigma_{n_{e_{\text{Det}}}}^2}{\sigma_{n_{\gamma_{\text{Det}}}}^2 + \sigma_{n_{e_{\text{Det}}}}^2}$$

With the slope between combined energy and  $\sigma_{n_{\gamma_{\text{Det}}}}$  and between energy and  $\sigma_{n_{e_{\text{Det}}}}$  defined in equation 4.24 the value of the shared statistical uncertainty in combined energy space can be determined. We first treat the case of  $\Delta E = 0$  in equation 4.25 which is also valid when the centroid of light yield and charge yield has been subtracted (discussed later).

$$\chi_{\text{Det}}^2 = M^2 \sigma_{n_{e_{\text{Det}}}}^2 + (1 - M)^2 \sigma_{n_{\gamma_{\text{Det}}}}^2 \quad (4.25)$$

The variable  $\chi$  is used to represent the observed  $\sigma$  when dealing in bins of

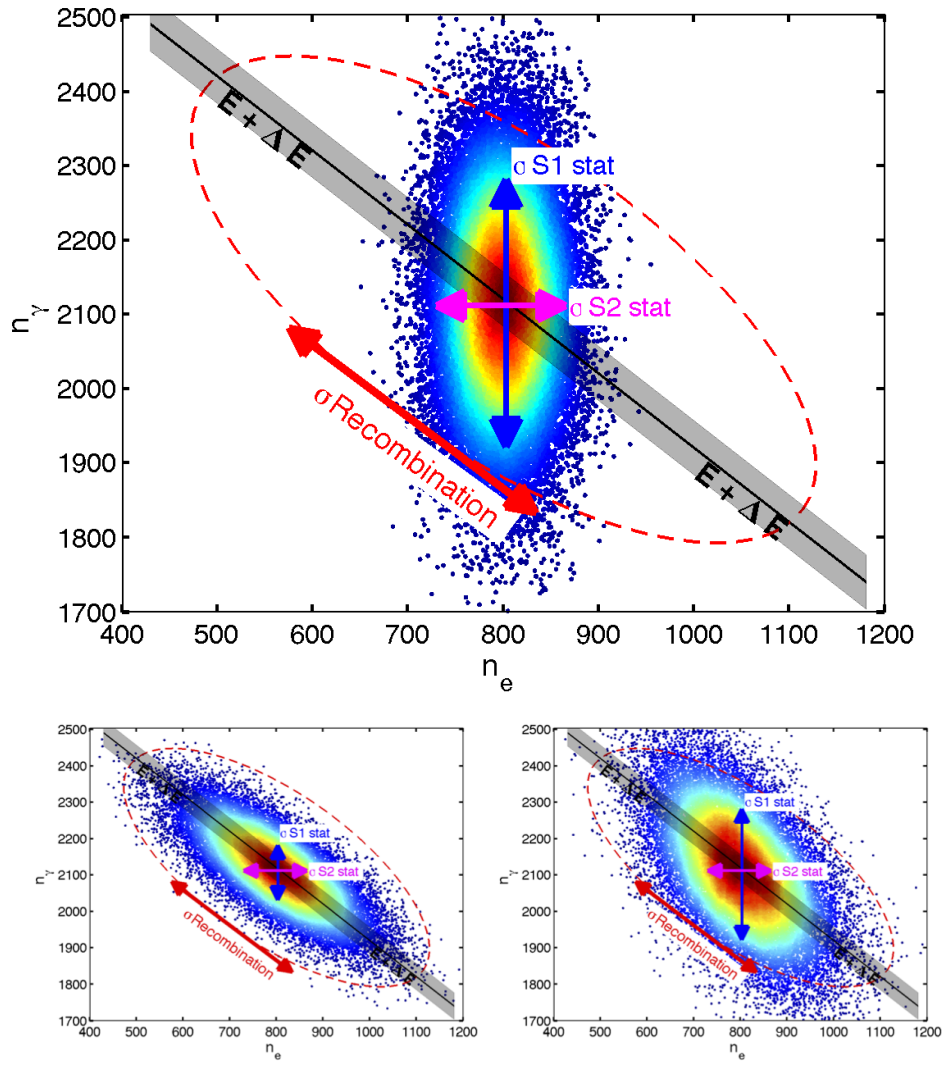


Figure 4.12: Top: Illustration of statistical variance, recombination fluctuations are set to 0. The spread in number of photons moves vertically and the spread in number of electrons moves horizontally. In black, a line of constant energy along the mean of combined energy with a width  $\Delta E$ . Bottom left: Dominated by recombination fluctuations which move  $45^\circ$  to statistical variances. Bottom Right: Typical values for recombination and S1, S2 Stat for Kr<sup>83</sup>.

combined energy. Let's briefly consider the implication of equation 4.25. For the case of  $\sigma_{n_{e\text{Det}}}^2 = \sigma_{n_{\gamma\text{Det}}}^2$ ,  $M=0.5$ , resulting in  $\sigma_{n_{e\text{Det}}}^2 = \sigma_{n_{\gamma\text{Det}}}^2 = \chi_{\text{Det}}^2$ . This case can be thought of as sweeping out equal variance from the statistical population which would for a circle as illustrated in Figure 4.12. For the case of  $\sigma_{n_{e\text{Det}}}^2 \neq \sigma_{n_{\gamma\text{Det}}}^2$  the observed statistical variance in a slice of combined energy will become less than the variance of the best channel. Specifically for the LUX detector the implication of equation 4.25 is that the statistical variance measured in a slice of combined energy will collapse to less than that of the S2 statistical uncertainty, as bin width  $\Delta_E$  goes to zero.

To complete the treatment of binned energy in this section we now add the final piece to the observed statistical variance, the contribution from the bin width  $\Delta_E$ . The residual variance arises from rotating the population of 2D gaussian about the bin center, the rotation having a slope of  $M$  or  $(1-M)$  as given in equation 4.24. Note, the residual term from the slope can also be removed by centroid subtraction of the photons and electrons vs. energy as discussed later in section 4.3.7, in that case we are only left with  $\chi_{\text{Det}}^2$  shared between the two channels.

$$\begin{aligned}\chi_{n_{\gamma\text{Det}}}^2 &= \chi_{\text{Det}}^2 + \frac{(MW\Delta_E)^2}{12} \\ \chi_{n_{e\text{Det}}}^2 &= \chi_{\text{Det}}^2 + \frac{((1-M)W\Delta_E)^2}{12}\end{aligned}\quad (4.26)$$

Were  $\chi^2$  is defined in 4.25,  $M$  is given in equation 4.24,  $W$  is the work function in [quanta/keV],  $\Delta_E$  is a bin of energy [keV], the normalization of 12 arrises from the second moment of a rotated line about its center. The total observed variance,

$\chi^2$ , in the number of photons and electrons considering a bin of combined energy can now be determined transforming equation 4.18 to 4.27.

$$\begin{aligned}\chi_{n_\gamma}^2 &= \sigma_{n_{ex}}^2 + n_i F(r)^2 + \sigma_r^2 n_i^2 + \chi_{n_{\gamma_{Det}}}^2 \\ \chi_{n_e}^2 &= n_i F(1-r)^2 + \sigma_r^2 n_i^2 + \chi_{n_{e_{Det}}}^2\end{aligned}\quad (4.27)$$

In equation 4.27 we have defined the observed standard deviation in units of quanta  $\chi$  for  $n_\gamma, n_e$  when working with bins of combined energy. In the limit that  $F$ ,  $\sigma_{n_{ex}}^2$  and  $\Delta_E$  go to zero the observed variance in number of photons and electrons ( $\chi_{n_\gamma}$  and  $\chi_{n_e}$ ) are related to the size of recombination fluctuations in a given combined energy bin, equation 4.28. Where  $\sigma_R$  is in units of quanta,  $\sigma_R = n_i \sigma_r$ .

$$\begin{aligned}\sigma_{R_\gamma}^2 &= \chi_{n_\gamma}^2 - \chi_{n_{\gamma_{Det}}}^2 \\ \sigma_{R_e}^2 &= \chi_{n_e}^2 - \chi_{n_{e_{Det}}}^2\end{aligned}\quad (4.28)$$

We have arrived at the conclusion of this section, armed with equation 4.28 we now have two methods for determining the size of recombination fluctuations,  $\sigma_R^2$  where the subscript  $\gamma$  or  $e$  is used to represent the channel of quanta used for the calculation. Either the observed variance in the light and charge channel can be used to measure the size of recombination fluctuation in a bin of energy. Any asymmetry between the two methods has implications which are discussed in the following subsection.

#### 4.3.4 Measuring the Fano Factor in Bins of Energy

There are three terms in equation 4.27 that give rise to an asymmetry between the observed variance  $\sigma_{R_\gamma}^2$  and  $\sigma_{R_e}^2$ . The small difference in variance from the slope can be solved for exactly leaving just the Fano factor  $F$  and  $\sigma_{n_{ex}}^2$ . By taking the difference of variance in the two channels component of recombination variance drops out leaving only the Fano factor and the variance in number of exitons, given in equation 4.27.

$$\sigma_{R_\gamma}^2 - \sigma_{R_e}^2 = \sigma_{n_{ex}}^2 + n_i F(2r - 1) \quad (4.29)$$

$F$  is the Fano factor, equation 4.16,  $\sigma_{n_{ex}}^2$  is the variance of the number of exitons produced and  $r$  is the recombination fraction, equation 4.17. Consider the case such that variance in the number of exitons  $\sigma_{n_{ex}}^2$  is much less than the contribution from the Fano factor. In such a regime we can solve for the Fano factor, potentially energy dependent, from equations 4.29.

$$F(E) = \frac{\sigma_{R_\gamma}^2 - \sigma_{R_e}^2}{n_i(2r - 1)} \begin{cases} r \neq \frac{1}{2} \end{cases} \quad (4.30)$$

There is an underlying subtlety to equation 4.30. Remarkably, in the limit that  $\Delta_E$  goes to zero the Fano factor can be extracted with minimal knowledge of intrinsic detector statistical variance. Further, when the statistical variance of S1 and S2 are identical the value of  $M$  (equation ??) will be 0.5. In that special case no knowledge of the statistical variance is needed to measure the Fano factor.

When  $r = \frac{1}{2}$  the coefficient in front of the Fano factor becomes zero in equation

4.29. At this value an equal contribution from the Fano factor goes into the variance  $\chi^2$  of photons and electrons, allowing for the smaller value of  $\sigma_{\text{ex}}^2$  to be extracted.

$$\sigma_{n_{\text{ex}}}^2 = \sigma_{R_\gamma}^2 - \sigma_{R_e}^2 \left\{ r = \frac{1}{2} || \sigma_{n_{\text{ex}}}^2 >> n_i F(2r - 1) \right. \quad (4.31)$$

Equation 4.31 is also valid in the case that  $\sigma_{n_{\text{ex}}}^2$  is much larger than the contribution from the Fano factor. This happens to be true when dealing with the time dependent light yield of  $^{83m}\text{Kr}$ , this topic will be explored in the next section.

### 4.3.5 Application to $^{83}\text{Kr}$

Using the high stats Kr83 calibration data we can validate the method for working in a bin of energy since the exact solution for recombination and detector fluctuations can be measured, as outlined in section 4.3.1 and 4.3.3. Once the fluctuations from detector resolution are measured in the light and charge channel (S1 and S2 signals), the asymmetry between the two channels can be used to calculate the Fano factor (equation 4.27). The asymmetry in fluctuations in the light and charge channel arises from the Fano factor acting on ion production which is later amplified through the recombination fraction, as long as the recombination fraction does not equal 0.5. For the case of the  $^{83m}\text{Kr}$  calibration the recombination fraction was 0.772 resulting in recombination fluctuations of 3 to 4 more quanta in the light channel as compared to the charge channel, see table 4.4. Though the additional recombination fluctuation is small having ample statistics the Fano factor can be constrained. The errors in the measurement were derived from simulated Kr data sets of 400,000 events

with the Fano factor turned off, using 100 trials. First, recombination fluctuations were turned off and only fluctuations from detector resolution as calculated in section 4.3.1 were used, see Table 4.2. It was found that the error of the difference in recombination fluctuation from the light and charge channel ( $\sigma_{R_\gamma}^2$  and  $\sigma_{R_e}^2$ ) along with the error in ion production and recombination fraction were enough to constrain the Fano factor to 0.001-0.003. Next, the value of recombination was set slightly higher than the actual value of 82 to 100 quanta and the trials were repeated, see table 4.3. With the addition of recombination fluctuations to detector resolution fluctuations the error on measuring the Fano factor grew to 0.002-0.009, with smaller bin sizes ( $\Delta E$  around the center leading to the smallest error as seen from equation 4.26).

The results of the high stats calibration data are shown in table 4.4, containing 400k events in the fiducial volume of the detector. Using equation 4.28 we find good agreement between the method described in equation 4.19 and the recombination fluctuation calculated from the charge channel ( $\sigma_{R_\gamma}$  and  $\sigma_{R_e}$ ). The accuracy helps us build confidence that the statistical components of the detector are modeled well enough to measure recombination fluctuation to within 3%. Further, the ability to see the asymmetry in recombination fluctuations between the light and charge channel demonstrates the power of using binned combined energy (section 4.3.3). Any observed difference between the two channels can only be from either the Fano factor or spread in exiton production, but we assume the fluctuations in exiton production are much less than fluctuations in ion production. The Fano factor is derived from equations 4.30 and the uncertainty was determined from simulations.

$\Delta_E$ [keV]	Count	$\sigma(\sigma_{R_\gamma}^2)$	$\sigma(\sigma_{R_e}^2)$	$\sigma(\sigma_{R_\gamma}^2 - \sigma_{R_e}^2)$	$\sigma F$
0.025	1528	77.8	77.9	1.3	0.0008
0.05	3063	54.4	54.6	1.8	0.0012
0.1	6128	36.4	36.6	2.6	0.0016
0.2	12242	23.7	23.8	3.7	0.0023
0.25	15290	22.9	22.9	4.0	0.0026
0.5	30528	17.5	17.5	5.2	0.0033

Table 4.2: Values for the standard deviation of the observed value of  $\sigma_R^2$  from  $n_\gamma$  and  $n_e$  along with the standard deviation of the difference, for a simulated  $^{83m}\text{Kr}$  decay with recombination set to zero. Note, since the two methods for determining  $\sigma_R^2$  are correlated the standard deviation of the measured difference is small leading to an improved error when calculating the Fano factor or  $\sigma_{n_{ex}}^2$ .

The total fluctuation as number of quanta is listed in the rightmost column. The Fano factor manifests itself as an asymmetry between fluctuations in the light and charge channel as given in equation 4.27, the recombination fraction was found to be  $r = 0.772$  and the average number of ions produced per decay was  $n_i = 2900$ . Having demonstrated the method for a mono energetic calibration source the next step will be to apply the method on the continuous beta spectrum of the tritium data.

$\Delta_E$ [keV]	Count	$\sigma(\sigma_{R_\gamma}^2)$	$\sigma(\sigma_{R_e}^2)$	$\sigma(\sigma_{R_\gamma}^2 - \sigma_{R_e}^2)$	$\sigma F$
0.025	1523	498	498	3.2	0.0020
0.05	3056	347	347	4.1	0.0026
0.1	6118	237	237	5.3	0.0033
0.2	12225	171	171	8.6	0.0054
0.25	15285	149	148	9.5	0.0060
0.5	30514	101	99.4	14.3	0.0090

Table 4.3: Values for the standard deviation of the observed value of  $\sigma_R^2$  from  $n_\gamma$  and  $n_e$  along with the standard deviation of the difference, for a simulated  $^{83m}\text{Kr}$  decay with recombination set to 100 quanta. Note, since the two methods for determining  $\sigma_R^2$  are correlated the standard deviation of the measured difference is small leading to an improved error when calculating the Fano factor or  $\sigma_{n_{ex}}^2$ .

#### 4.3.6 Application to Tritium Data (any continuus spectrum)

Adapting the equation of the previous section to continuous energy spectra requires that the centriod of a continue spectrum be subtracted off so that the variance from the light yield or charge yield vs. energy is removed. ...

After applying the Smearing Model of Section 4 we apply the method described in this section to extract recombination fluctuations form the tritium data.

In this subsection we test method outlined in section 4.3.3 for dealing in bins of combined energy specifically applied to the tritium beta spectrum, but the method

$\sigma_R$ 4.19 (Quanta)	$\Delta_E$ (keV)	Count	$\sigma_{R_\gamma} = \sqrt{\chi_{n_\gamma}^2 - \chi_{n_{\gamma\text{Det}}}^2}$ (Quanta)	$\sigma_{R_e} = \sqrt{\chi_{n_e}^2 - \chi_{n_{e\text{Det}}}^2}$ (Quanta)	$F = \frac{\sigma_{R_\gamma}^2 - \sigma_{R_e}^2}{n_i(2r-1)}$ (Quanta)	$\sqrt{Fn_i}$ (Quanta)
82.4 ± 4.0	0.025	1518	87.2 ± 2.9	87.1 ± 2.9	0.010 ± 0.002	5.8 ± 0.5
	0.05	3124	85.0 ± 2.0	84.9 ± 2.0	0.005 ± 0.003	3.8 ± 1.1
	0.1	6269	87.8 ± 1.3	87.6 ± 1.3	0.023 ± 0.003	8.1 ± 0.5
	0.2	12508	90.0 ± 1.0	89.7 ± 1.0	0.021 ± 0.005	7.8 ± 0.9
	0.25	15557	88.5 ± 0.8	88.3 ± 0.8	0.013 ± 0.006	6.1 ± 1.3
	0.5	30826	87.0 ± 0.6	86.7 ± 0.6	0.027 ± 0.009	8.8 ± 2.2

Table 4.4: Values for the standard deviation of the observed value of  $\sigma_R^2$  from  $n_\gamma$  and  $n_e$  along with the standard deviation of the difference, for a  $^{83m}\text{Kr}$  data set with 400k events in the fiducial volume. The Fano factor is derived from equations 4.30 and the uncertainty was determined from simulations. The total fluctuation as number of quanta is listed in the rightmost column. The Fano factor manifests itself as an asymmetry between fluctuations in the light and charge channel as given in equation 4.27, with a recombination fraction of 0.772 and  $n_i = 2900$ .

outlined can be used for any continue spectrum. To first order the treatment of the continuous spectrum is identical to that outlined for the mono energetic source as outlined previously in subsection 4.3.3. Figure 4.13 illustrates a tritium beta spectrum convolved with detector resolution similar to that measured for the LUX detector, the figure is analogous to Figure 4.12. As the bin size around a value of combined energy is squeezed to zero the statistical variance in the number of photons and electrons converge, the value is given by equation 4.26. Whereas, regardless of

bin size recombination fluctuations remain since they move along lines of constant energy. In order to adapt the methodology developed for a mono energetic source to a continuous energy spectra requires that the centriod of the light and charge yield be subtracted off. The slope in the light and charge channels from the fundamental yield induce a further variance on top of  $\chi_{\text{Det}}$  from the population in an energy bin being tilted as demonstrated in figure 4.14. For the purposes of this study, we find it sufficient to fit a quadratic form to the centroid of the entire population and subtract off the local slope from the measured variance. An analogous methods for centriod subtraction to extract recombination fluctuations are described in detail in [Patrick's Thesis].

#### 4.3.7 Centriod Subtraction

For the case of a continuous source we expand upon the result from section 4.3.3 where the additional variance from detector resolution was calculated per energy bin as  $\chi_{n_{\gamma_{\text{Det}}}}^2$  and  $\chi_{n_{e_{\text{Det}}}}^2$ . When dealing with a continuous source we must subtract off the centroid of the number of photons and electron vs. energy to remove additional variance induced by the slope. What results is a common variance from detector resolution shared by both the charge and light channel in each bin of energy, defined as  $\chi_{\text{Det}}^2 = \chi_{n_{\gamma_{\text{Det}}}}^2 = \chi_{n_{e_{\text{Det}}}}^2$ , equation 4.32. The value of  $\chi_{\text{Det}}^2$  is derived in 4.33 for a small variation in  $n_e$  around combined energy, and is identical to that found for the case of the mono energetic source in equation 4.25. This is analogous to saying that the centriod subtraction is removing the additional variance from the slope of

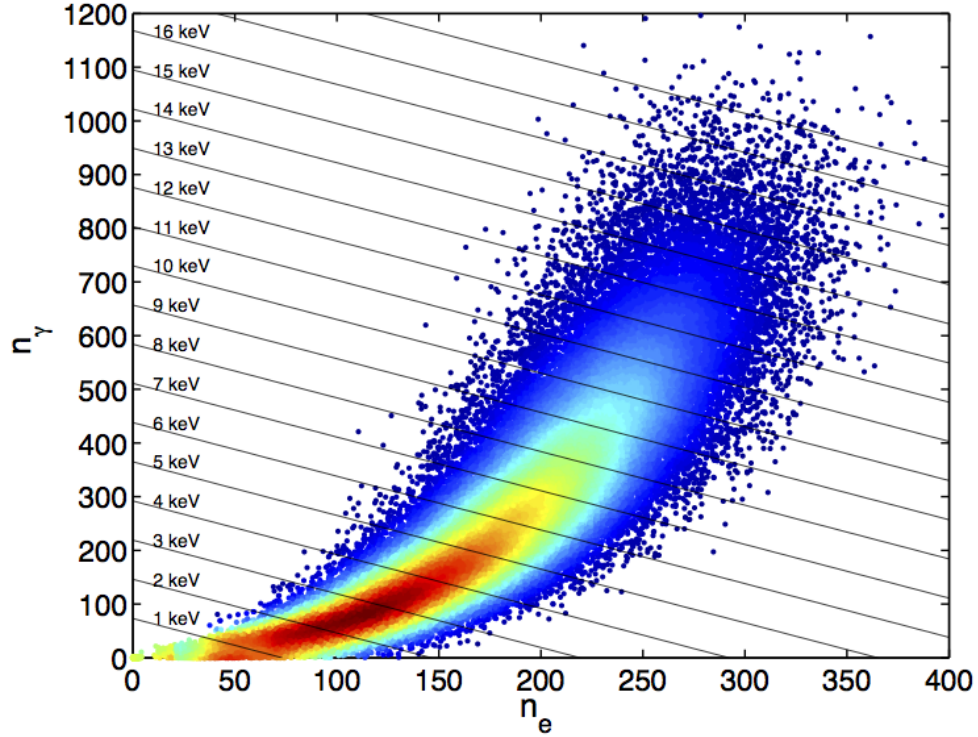


Figure 4.13: Illustration of statistical variance for the tritium beta spectrum, recombination fluctuations are set to 0. This plot is analogous to Figure 4.12 which illustrates the case for the mono energetic  $^{83m}\text{Kr}$  decay. Recombination fluctuation move along lines of constant energy, S1 statistical fluctuation move vertically and S2 statistical fluctuations move horizontally.

light field and charge yield. The local slope of  $n_e$  with respect to quanta ( $n_\gamma + n_e$ ) is  $(1-M)$ , given in 4.24. To demonstrate the effectiveness of the method we use the measured detector resolution along with a test recombination fluctuation and simulate a tritium spectrum. The result of extracting recombination is shown in figure 4.15 for various energy bin widths. As long as the recombination is greater than  $\chi_{\text{Det}}$ , which is being added in quadrature, the value of recombination can be determined to good precision using the method. The small deviation around the

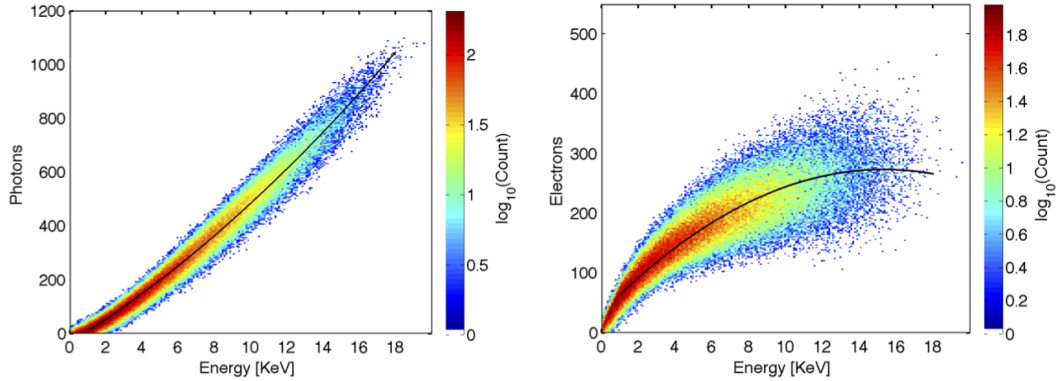


Figure 4.14: Light yield (left) and Charge yield (right) of a simulated tritium spectrum, with the fit to the centroid show in black. The variance in number of photon and electrons per energy bin is used to extract recombination fluctuations.

first and last bins is due to the spectral shape, a correction for spectral shape will be discussed in the next section and will improve the measurement of  $\sigma_R$ . The analytic solution for extracting recombination given in equation 4.32 is sufficient to first order, we ignore second order corrections in this analysis. After correcting observables for the tritium beta spectral shape we will be ready to use the tools of this section to decouple detector resolution and measure recombination fluctuations from the tritium data

$$\begin{aligned}\sigma_{R_\gamma}^2 &= \chi_{n_\gamma}^2 - \chi_{\text{Det}}^2 \\ \sigma_{R_e}^2 &= \chi_{n_e}^2 - \chi_{\text{Det}}^2\end{aligned}\tag{4.32}$$

$$\begin{aligned}
\delta[\Delta n_e] &= \delta[n_e] - \delta \left[ \langle n_e \rangle_{n_e + n_\gamma} \right] \\
&= \frac{\overset{1}{dn_e}}{\cancel{dn_e}} \delta[n_e] + \frac{\overset{0}{dn_e}}{\cancel{dn_\gamma}} \delta[n_\gamma] - \delta \left[ \langle n_e \rangle_{n_e + n_\gamma} \right] \\
&= \delta[n_e] - \frac{d \langle n_e \rangle}{d(n_e + n_\gamma)} \frac{d(n_e + n_\gamma)}{dn_e} \delta[n_e] - \frac{d \langle n_e \rangle}{d(n_e + n_\gamma)} \frac{d(n_e + n_\gamma)}{dn_\gamma} \delta[n_\gamma] \\
\delta[\Delta n_e] &= \delta[n_e] - (\delta[n_\gamma] + \delta[n_e]) \frac{d \langle n_e + n_\gamma \rangle}{d(n_e + n_\gamma)}
\end{aligned}$$

$$\delta[\Delta n_e] = (M)\delta[n_e] - (1-M)\delta[n_\gamma]$$

$$\chi^2_{Det} = Var(\Delta n_e) = (M)^2 \delta^2[n_e] + (1-M)^2 \delta^2[n_\gamma] - 2M(1-M) \underbrace{\delta[n_e] \delta[n_\gamma]}_0$$

(4.33)

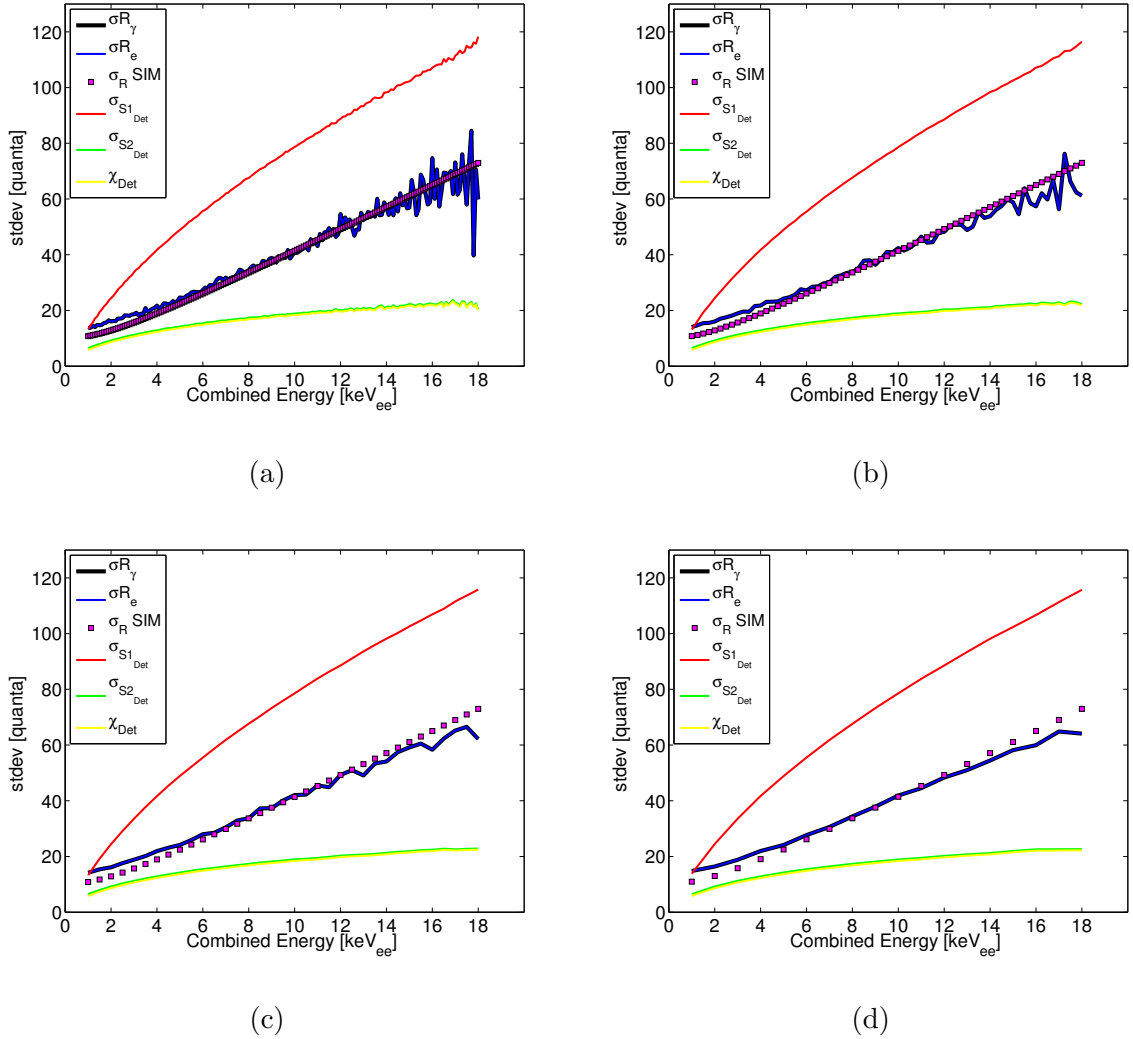


Figure 4.15: Simulated tritium spectrum with the detector resolution of the LUX detector,  $\sigma_{S1_{\text{Det}}}$  and  $\sigma_{S2_{\text{Det}}}$ , and an arbitrary recombination fluctuation  $\sigma_R$  (magenta). After centroid subtraction we apply the methodology described in the previous section to extract  $\sigma_R$  (black and blue) through the light and charge channel using our knowledge of detector resolution per each energy bin  $\chi_{\text{Det}}$  (green),  $S1_{\text{Det}}$  (red) and  $S2_{\text{Det}}$  (yellow). The plots show cases for various bin widths in [KeV]: a)  $\Delta E = 0.1$  b)  $\Delta E = 0.25$  c)  $\Delta E = 0.5$  d)  $\Delta E = 1$ .

## 4.4 Correcting the Tritium Spectral Shape for Finite Resolution

The goal of the following two sections is to extract light yield, charge yield and recombination fluctuations from the tritium spectrum using the methods described in section 4.3.3. The first step is to use the NEST model in an attempt to undue the effect of the tritium spectral shape and finite detector resolution, described in this section. We find that the light yield and charge yields extracted from the data deviate too much to apply the correction factor. Since the correction is found to be small we can proceed to extract new LY, QY and  $\sigma R$  from the tritium data without correction building a model that better reproduces the data than the NEST model (which has yet to be vetted at our electric field and energy). We then take that improved model and apply the correction.

The distribution of tritium events convolved with the detector's finite resolution for S1 (scintillation) and S2 (ionization) causes the observed mean to shift from the actual mean. The shift is non trivial and depends on the spectral shape and the functional form resolution over a range of energies. A large negative derivative of the spectral shape will tend to pull the observed spectrum to lower values, and the functional form of the resolution will also shift the spectrum. Figure 4.16 and equations 4.35,4.38 demonstrate a simple model to solve for the relation between observed mean and actual mean. Take for example a linearly declining distribution, starting with infinite detector resolution we set up bins of width  $\Delta x$ . To account for finite energy resolution we distribute the counts in each rectangular bin into Gaussians centered at  $\mu_i$ , with a spread of  $\sigma_i$ , and normalized to the area of the bin

$N_i \times \Delta x$  with amplitude  $c_i$ . Each rectangular bin(i) can be written as a Gaussian  $G(i)$ :

$$c_i = \frac{N_i \times \Delta x}{\sigma_i \sqrt{2\pi}}$$

$$G_i(x) = c_i \times \exp\left(\frac{-(x - \mu_i)^2}{2\sigma_i^2}\right)$$

(4.34)

Where  $N_i$  is the count in the  $i^{\text{th}}$  bin,  $\Delta x$  is the bin width,  $\mu_i$  is the bin center and  $\sigma_i$  is the resolution at the  $i^{\text{th}}$  bin. Figure 4.16 show the application of equation 4.34 to a linear energy distribution with a  $\sqrt{E}$  dependent  $\sigma$ . The observed distribution is the sum of the Gaussians, shown in red.

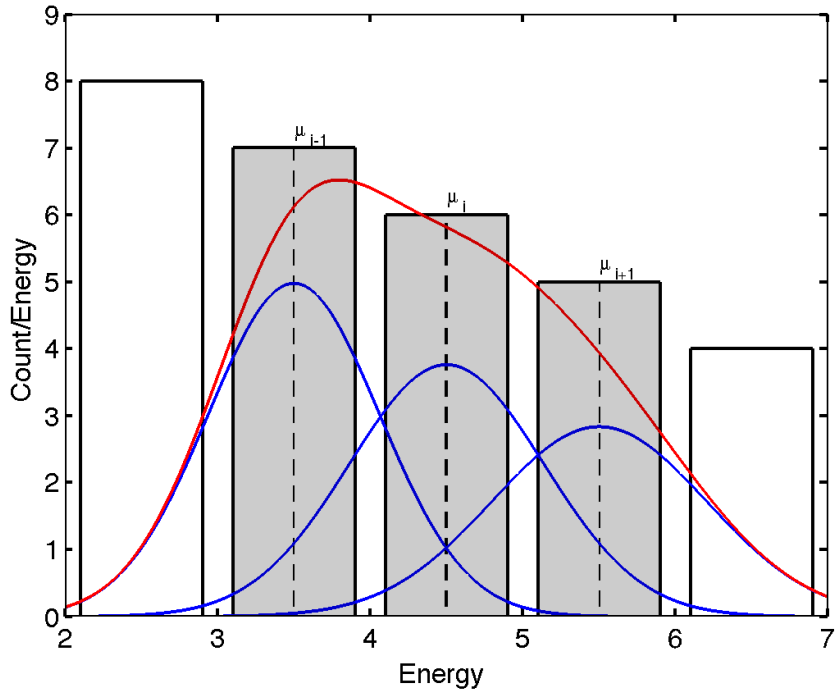


Figure 4.16

#### 4.4.1 Calculating the Observed Energy

After modeling the finite resolution with Gaussians the mean observed at each bin can be calculated from the overlap of all bins weighted by the corresponding means. We can write the observed mean in the  $i^{\text{th}}$  bin,  $\nu_i$ , in terms of the bin centers  $\mu$  and overlapping areas of all bins using equation 4.34:

$$\nu_i = \frac{\sum_{j=1}^n \mu_j \int_{\mu_i - \frac{\Delta x}{2}}^{\mu_i + \frac{\Delta x}{2}} G_j(x) dx}{\sum_{j=1}^n \int_{\mu_i - \frac{\Delta x}{2}}^{\mu_i + \frac{\Delta x}{2}} G_j(x) dx} \quad (4.35)$$

Equation 4.35 can be solved in terms of error function and complimentary error function, first we will generalize a formula to solve for the overlapping area from the  $j^{\text{th}}$  bin into the  $i^{\text{th}}$  bin.

$$A_{i,j} = \int_{\mu_i - \frac{\Delta x}{2}}^{\mu_i + \frac{\Delta x}{2}} G_j(x) dx = \begin{cases} c_i \operatorname{erf}\left(\frac{\Delta x}{\sigma_i \sqrt{2}}\right), & j = i \\ \frac{c_j}{2} \operatorname{erfc}\left(\frac{|\mu_j - \mu_i| - \frac{\Delta x}{2}}{\sigma_j \sqrt{2}}\right) - \frac{c_j}{2} \operatorname{erfc}\left(\frac{|\mu_j - \mu_i| + \frac{\Delta x}{2}}{\sigma_j \sqrt{2}}\right), & j \neq i \end{cases} \quad (4.36)$$

As  $\mu$  approaches zero the Gaussian distribution of equation 4.34 begins to spill over into negative values, which in some cases may be unphysical. For instance, the Gaussian assumption leads to negative photons. We can chose to ignore this area or make the distribution more Poisson like by bouncing the Gaussian back at  $\mu = 0$ .

The formula for accounting for the area of the reflected Gaussian is described in 4.37.

Ultimately this assumption has little impact on the S1 and S2 analysis because the threshold cut off well before the zero interface is reached, but it does make the distributions more Poisson like near the zeroth bins. Equation 4.37 is the same as 4.36 with the bin center  $\mu_i$  mapped to  $-\mu_i$ .

$$B_{i,j} = \frac{c_j}{2} \operatorname{erfc} \left( \frac{|\mu_j + \mu_i| - \frac{\Delta x}{2}}{\sigma_j \sqrt{2}} \right) - \frac{c_j}{2} \operatorname{erfc} \left( \frac{|\mu_j + \mu_i| + \frac{\Delta x}{2}}{\sigma_j \sqrt{2}} \right) \quad (4.37)$$

The error function and complementary error function are defined in equation 4.38 and the coefficient  $c_i$  is defined in equation 4.34.

$$\begin{aligned} \operatorname{erf}(x) &= \frac{2}{\sqrt{\pi}} \times \int_0^x \exp(-t^2) \\ \operatorname{erfc}(x) &= \frac{2}{\sqrt{\pi}} \times \int_x^\infty \exp(-t^2) = 1 - \operatorname{erf}(x) \end{aligned} \quad (4.38)$$

Finally, we solve for the observed mean in the  $i^{th}$  bin by summing all the Gaussian overlaps  $A_{i,j} + B_{i,j}$  (equations 4.36,4.37), weighting the overlapping area from each bin by the corresponding bin center  $\mu_j$ . The result is shown in equation 4.39 and is equivalent to equation 4.35 when the area from the reflected Gaussian

is not considered,  $B_{i,j}=0$ .

$$\nu_i = \frac{\sum_{j=1}^n \mu_j \cdot (A_{i,j} + B_{i,j})}{\sum_{j=1}^n (A_{i,j} + B_{i,j})} \quad (4.39)$$

#### 4.4.2 Smearing a Toy Spectrum

To demonstrate the application of equation 4.39 we use it to smear a toy linearly decaying spectrum. By modifying the dependence of  $\sigma_i$  on  $\mu_i$  we can better understand the effects of the spectral shape and the functional form of the resolution.

Figure 4.17 shows the effect of the finite resolution on a linearly decaying spectral shape. Using a constant resolution  $\sigma$  the observed mean, when accounting for finite resolution, shifts down due to the spectral shape. In the case with  $\sigma_i \sim \sqrt{\mu_i}$  the observed mean at first shifts higher as the increasing width at higher value bin centers, even with lower counts, out weighs the lower bin centers with higher counts and narrower widths. In both cases as the bin centers approach zero the observed mean shifts higher due to an imposed threshold at zero, here Poisson statistics take over and the Gaussian characterization leads to a loss of events below zero. Thus, for the sake of the toy model in figure 4.17 we only characterize the relation between the real mean and the observed mean from the second bin center. It is also worth mentioning that for the case of having a varying resolution in figure 4.17 the shift in spectral shape seems minor, yet there is a significant 20% deviation in the observed mean of the last bin.

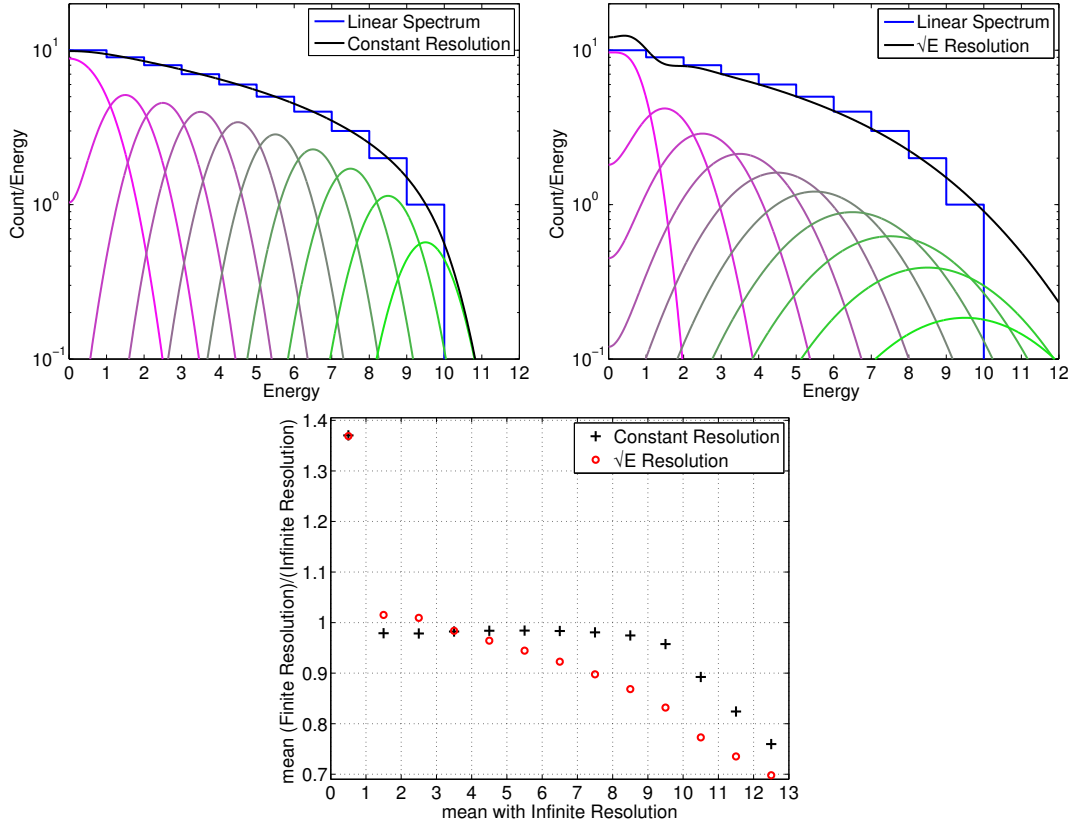


Figure 4.17: Top Left: A linearly decaying spectrum, in blue. The black curve represents the sum of the Gaussians assuming a constant resolution. Top Right: A linearly decaying spectrum, in blue. The black curve represents the sum of the Gaussians with a  $\sqrt{E}$  dependent resolution. Bottom: The observed mean, with finite resolution, compared to the real mean with infinite resolution. The black points are for the case with linear resolution and the red points represent the case with  $\sqrt{E}$  dependent resolution.

## 4.5 Measuring LY, QY and Recombination, Uncorrected for Spectral shape

### 4.5.1 Tritium S1 Mean and NEST

The correction for the mean of the measured light yield, S1 [Phe], for tritium beta decay can be solved for using equation 4.39. Starting with a simulated S1 tritium spectrum with infinite resolution and applying equations 4.34-4.39 one can attain the mapping of measured mean to true mean. The resolution of S1 was determined from statistical and instrumental fluctuations and is given in equation 4.12 and 4.13. The use of Gaussian error down to low S1 is an acceptable approximation since underlying distribution actually consists of the number of photons,  $n_\gamma = \frac{S1}{g1}$ . With  $g1=0.097$  there are still 20 photons near the S1 threshold of 2 [Phe], thus the Gaussian model is still a close approximation of the underlying Poisson distribution. We will use the Gaussian approximation as it makes the application of equations 4.34-4.39 much simpler. The variance in S1 is the result of recombination fluctuations, statistical fluctuations and instrumental fluctuations at a given energy. The functional form of all three have been previously measured and can be extrapolated for use with the tritium spectrum. The first step is to use the expected light yields from NEST along with the measured smearing from recombination and detector resolution to extract a correction factor for the observed S1 signal. Having a priori knowledge of light yields will allow for the spectral shape to be corrected or can at least be used to approximate an error when we go to extract the light yield and recombination

fluctuations from the tritium beta spectrum.

$$\sigma_{S1}^2 = g_1^2(\sigma_{n_{\gamma_{stat}}}^2 + \sigma_{n_{\gamma_{inst}}}^2 + \sigma_R^2) \quad (4.40)$$

Figure 4.18 shows the application of smearing from equation 4.40 applied to the expected S1 tritium spectrum from NEST overlaid with the data. The mapping for converting the observed S1 to the real S1 is shown in figure 4.18. To calculate the correction we start with the NEST light yield, apply the measured  $g_1$ , convolve it with a tritium beta spectrum and add in our first approximation of recombination fluctuations measured in equation 4.23, given infinite detector resolution this is the spectrum the LUX detector would observe in S1 space. Knowing the dependance of detector resolution vs. the number of photons of a given event (equation 4.14) we can apply the model as outlined in 4.4 and calculate the shift from observed mean photons to real mean photons.

#### 4.5.2 Tritium S2 Mean and NEST

The correction for the mean of the measured charge yield, S2 [Phe], for tritium beta decay can be solved for using equation 4.39. Starting with a simulated S2 tritium spectrum with infinite resolution and applying equations 4.34-4.39 one can attain the mapping of measured mean to true mean. The resolution of S2 was determined from statistical and instrumental fluctuations and is given in equation 4.12 and 4.13. The use of Gaussian error down to low S2 is an acceptable approximation since the S2 spectrum ends at 300 [Phe],  $n_e = \frac{S2}{g_2^2}$ . With  $g_2=5.75$  there are still 50 electrons near

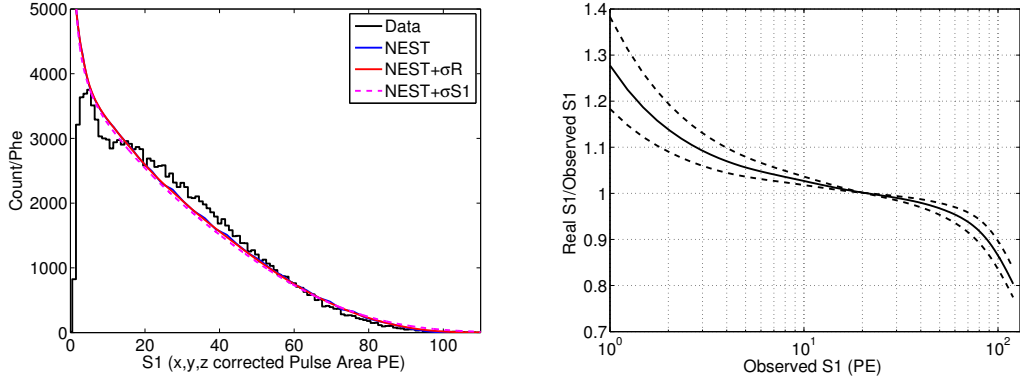


Figure 4.18: Left: In Black S1 tritium spectrum extracted from the data. In blue, The NEST light yield curve. In red, the NEST light yield curve with recombination fluctuations. Dashed magenta is NEST light yield with smearing from equations 4.40. Right: The ratio of the real mean to the observed mean vs. the observed mean for a tritium photon spectrum. Note the S1 threshold at about 3 Phe in S1.

end of the tritium spectrum, thus the Gaussian model is still a close approximation of the underlying Poisson distribution. We will use the Gaussian approximation as it makes the application of equations 4.34-4.39 much simpler. As in the case of the light yield, the variance in S2 is the result of recombination fluctuations, statistical fluctuations and instrumental fluctuations at a given energy. The functional form of all three have been previously measured and can be extrapolated for use with the tritium spectrum. We first use the expected charge yields from NEST along with the measured smearing from recombination and detector resolution to extract a correction factor for the observed S2 signal. Having a priori knowledge of light yields will allow for the spectral shape to be corrected or can at least be used to approximate an error when we go to extract the charge yield and recombination

fluctuations from the tritium beta spectrum.

$$\sigma_{S2}^2 = g_2^2(\sigma_{n_{e_{stat}}}^2 + \sigma_{n_{e_{inst}}}^2 + \sigma_R^2) \quad (4.41)$$

Figure 4.19 shows the application of smearing from equation 4.41 applied to the S2 tritium spectrum expected from NEST overlaid with the data. As with the S1 spectrum the correction is calculated using NEST for charge yield with the measured  $g_2$  applied, convolve it with a tritium beta spectrum and using our first approximation of recombination fluctuations measured in equation 4.23, given infinite detector resolution this is the spectrum the LUX detector would observe in S2 space. Having calculated the dependance of detector resolution vs. the number of photons of a given event (equation 4.14) we can apply the smearing as outlined in 4.4 and calculate the shift from observed mean photons to real mean photons. From the S2 spectrum, which is more peaked than the S1, we see the 20% discrepancy with the NEST charge yield model but it may also be an indication of the error in  $g_1$  and  $g_2$ .

### 4.5.3 Tritium Energy Spectrum

The mapping of the observed energy to real energy was determined using a full simulation of tritium beta decay. The accuracy of the smearing model described in equations 4.34-4.39 can be tested by comparing it against the energy observed after a full NEST simulation. The energy depends on both S1 and S2 thus, mapping observed energy to true energy my be non trivial. Again, we start with a sim-

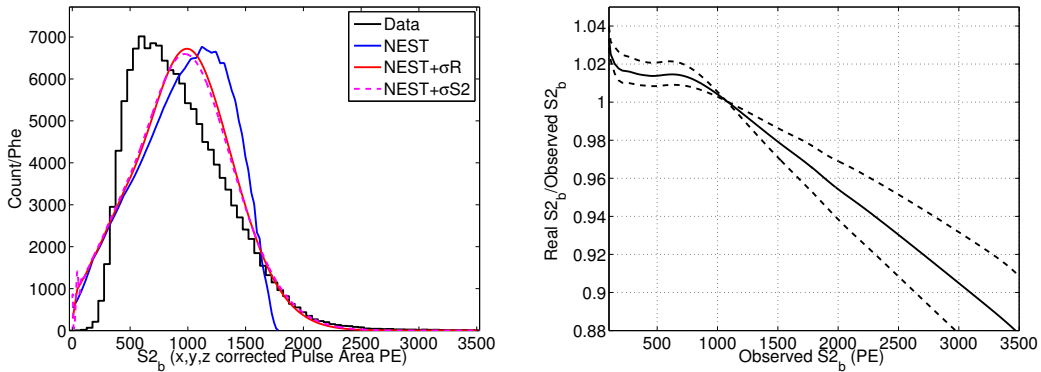


Figure 4.19: Left: In Black S2 tritium spectrum extracted from the data. In blue, The NEST light yield curve. In red, the NEST light yield curve with recombination fluctuations. Dashed magenta is NEST light yield with smearing from equations 4.41. Right: The ratio of the real mean to the observed mean vs. the observed mean for a tritium photon spectrum. Note the S2 threshold at about 400 Phe in S2.

ulated tritium energy spectrum with infinite resolution and apply the empirically determined resolution in equation 4.47, measured with  $^{127}\text{Xe}$  X-rays and  $^{83\text{m}}\text{Kr}$  calibrations. Figure 4.20 shows the comparison of smearing model vs true energy along with the smearing after running full photon and electron propagation in LUXSIM vs the true energy. The smearing form the model described in equations 4.34-4.39 is almost identical to the output of LUXSIM. The energy spectrum flares out at low energy, is pulled in from 5-10 [keV] and again flares out slightly above 15 [keV]. It is important to note that the change in the spectral shape is hardly noticeable, as was the case with S1 and somewhat with S2. Figure 4.21 shows the results for mapping observed energy to real energy using both smearing methods. The two methods show good agreement down to the threshold of 1.5 [keV], the agreement

with simulation is always within 1%. Below 2 [keV] the model predicts the ratio of true energy to observed energy to rise as there are greater number of events at higher energy spilling over to lower energy, the simulation however does not show this behavior leading to a 5% discrepancy in the 1 [keV] bin. We take the difference between the smearing model and LUXSIM as a systematic uncertainty.

Using equation 4.30, 4.6 and 4.42 we solve for the the spread in E as a function energy 4.47.  $a_\gamma$  and  $a_e$  are the coefficients in front of the root n term on the  $n_\gamma$  and  $n_e$  statistical variance .  $W=73 \left[ \frac{N_{\text{quanta}}}{\text{keV}} \right]$ .

$$E = \frac{1}{W} (n_\gamma + n_{e^-}) \quad (4.42)$$

$$\sigma E^2 = \frac{1}{W^2} (\sigma n_\gamma^2 + \sigma n_{e^-}^2) \quad (4.43)$$

$$\sigma E^2 = \frac{1}{W^2} (a_\gamma^2 n_\gamma + a_e^2 n_{e^-}) \quad (4.44)$$

$$\sigma E^2 = \frac{(a_\gamma + a_e)^2}{W} \frac{(n_\gamma + n_{e^-})}{W} \quad (4.45)$$

$$\sigma E^2 = \frac{(a_\gamma + a_e)^2}{W} E \quad (4.46)$$

$$\sigma E = \frac{(a_\gamma + a_e)}{\sqrt{W}} \sqrt{E} \quad (4.47)$$

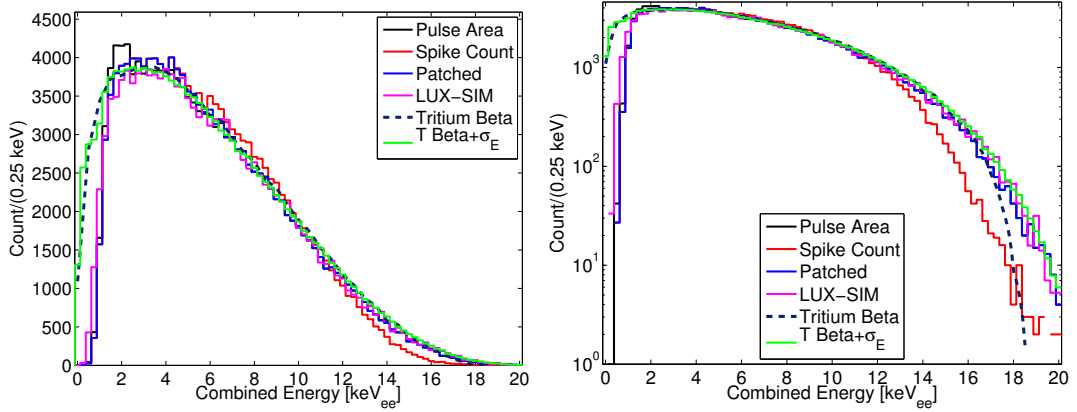


Figure 4.20: The tritium energy spectrum reconstructed from the data using both Pulse Area and Spike count for S1. Along with LUX SIM, the true tritium beta spectrum and a tritium spectrum smeared with detector resolution.

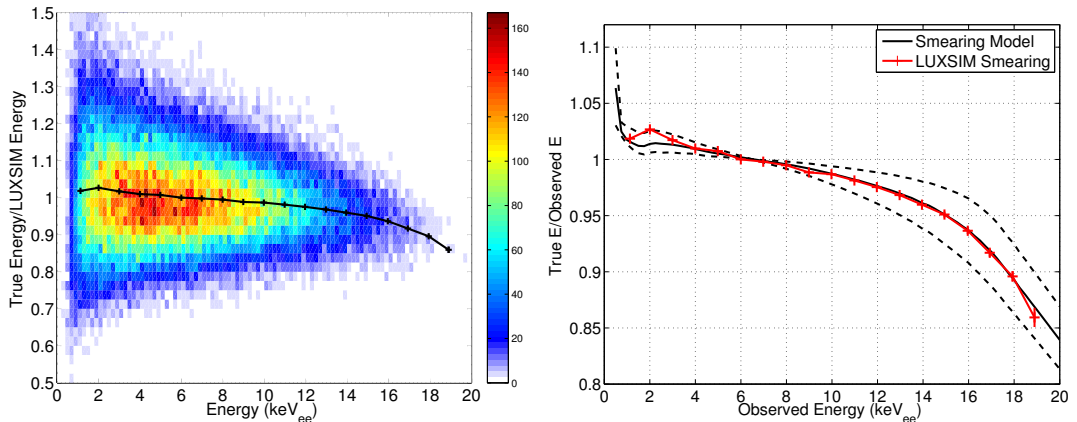


Figure 4.21: Left, mapping from real Monte Carlo energy to observed energy after applying a finite resolution using LUXSIM. Right, comparing the correction determined from the Monte Carlo (Red) to the detector smearing model (black) given in equation 4.47. The dashed lines represent the uncertainty in the measured value of  $F(E)$ . The agreement is within errors from 1 to 18 keVee. The Energy threshold is near 1.0 keVee.

#### 4.5.4 LY, QY, $\sigma$ R Result

The S1 and S2 spectral shape is not a good match with the light yield model from NEST, thus applying a correction to the observed means using NEST is not prudent. Fortunately, we see that both in the S1 and S2 region of interest were the majority of the tritium events occur the spectral shape correction is less than 10%. Further, the reconstructed energy, uncorrected for spectral shape, is go to within 10% as well. Knowing this we can move forward with extracting a more accurate light yield and recombination fluctuation accepting the small error in order to create a more accurate model than NEST to which then we can apply the spectral shape correction.

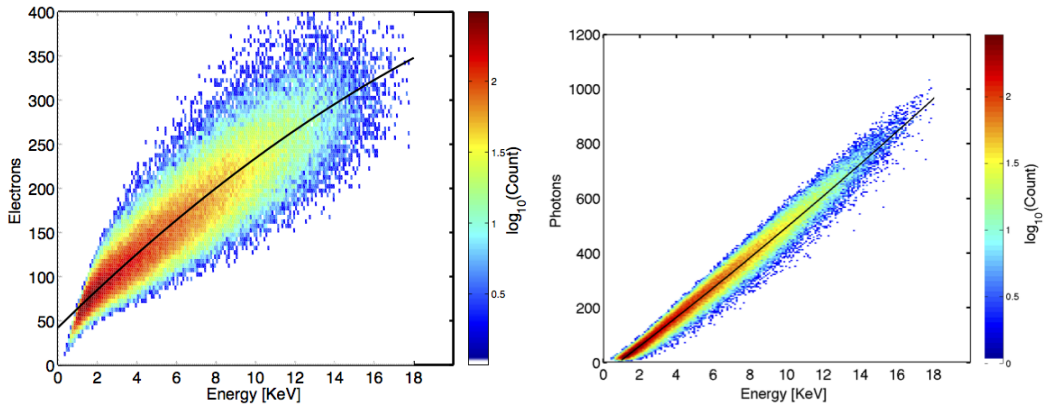


Figure 4.22: Number of photons (left) and electrons (right) vs. energy from tritium data without spectral shape correction. The spread in quanta per energy bin is used to measure recombination fluctuations.

Having extracted light yield (Photons/keV) and charge yield (electrons/keV) we compare the initial result from the tritium data to NEST, and is shown in figure 4.24. The disagreement between the data and the NEST yields was expected since previously the S1 and S2 tritium spectrum did not line up, in the previous section. Though the means do not match the measured light yield is within 1 sigma considering the large error in gains g1 and g2.

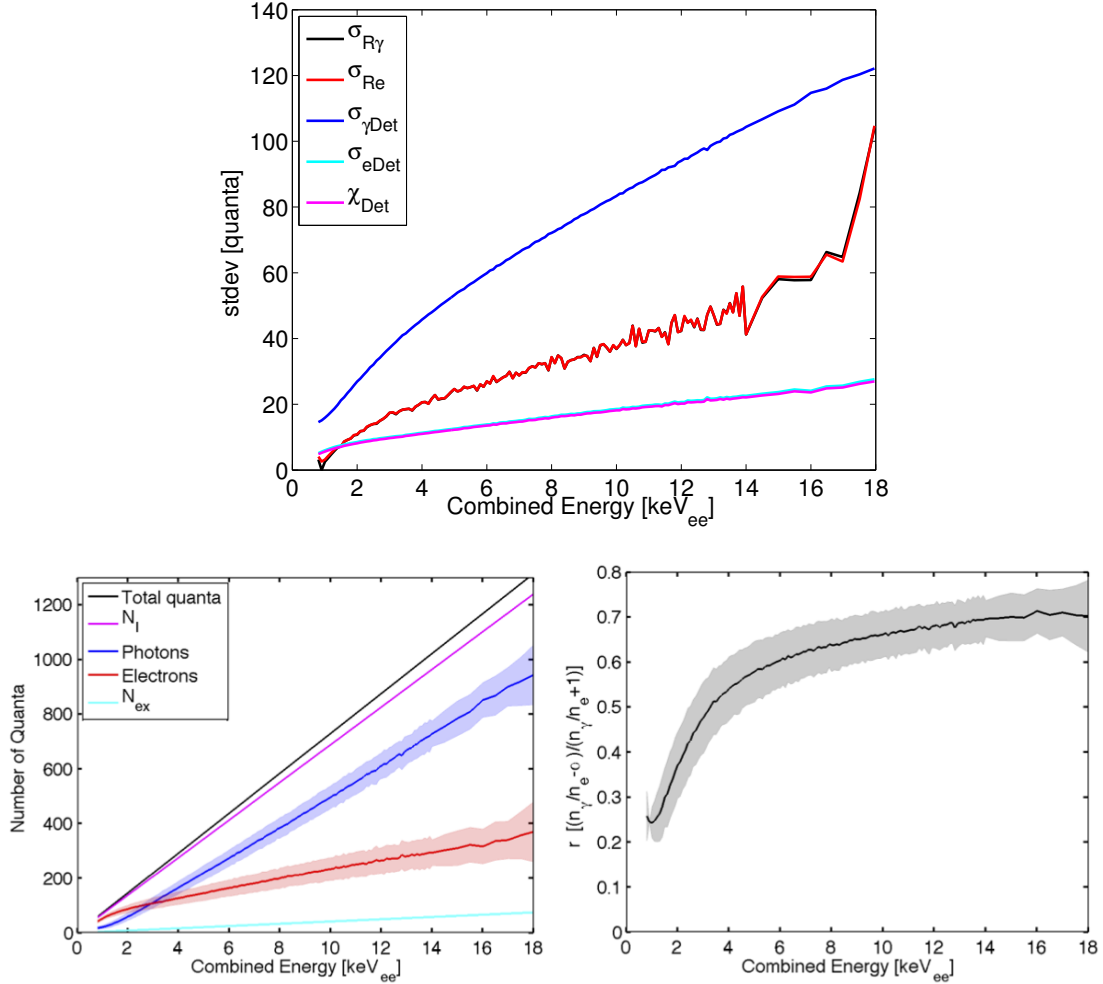


Figure 4.23: Top: Extracted recombination fluctuation from the tritium data from fluctuations in photons and electrons (Black and Red receptively). Bottom right: mean number of quanta in photons, electrons, ions, exitons vs. energy [keV] for the tritium calibrations. Bottom left: Recombination fraction and the one sigma (shaded) vs. energy [keV].

## 4.6 Measuring LY, QY, Recombination, Corrected for Spectral shape

In the previous section we determined that the NEST model was not sufficient to produce a spectral shape correction for the tritium data. However, it was shown

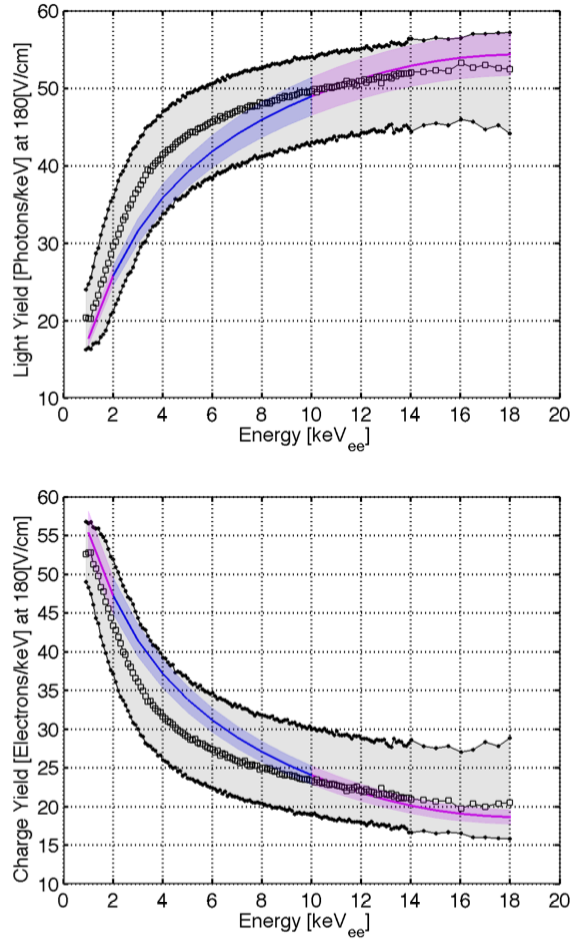


Figure 4.24: Light yield and charge yield from tritium data without spectral shape correction at 180 [V/cm] in black, the shaded region represents the one sigma uncertainty on g1 and g2. The NEST yield prediction and it's corresponding 1 sigma is shaded in blue. NEST interpolation is shown in magenta to energies where the model is not vetted.

that and spectral shape correction is sufficiently small (less than 10%) to extract light yield, charge yield and recombination from the tritium spectrum, using this information the model was improved and new simulations were produced. In this section we will take the information gathered in the previous section and apply

the known detector resolution in order to create a spectral shape correction for the tritium S1 and S2. Having an improved model for NEST we can even determine the efficiency for detecting tritium S1, S2 and the energy threshold, since the tritium spectrum still provides events well below the expected energy threshold of around 1.5 keV<sub>ee</sub>.

#### 4.6.1 Tritium S1 Correction

Figure 4.25 shows the application of smearing from equation 4.40 applied to the light yield extracted from the uncorrected tritium data with the data. The mapping for converting the observed S1 to the real S1 is shown in the figure. To calculate the correction we start with the extracted light yield, apply the measured g1, convolve it with a tritium beta spectrum and add in our first approximation of recombination fluctuations measured in equation 4.23, given infinite detector resolution this is the spectrum the LUX detector would observe in S1 space. Knowing the dependance of detector resolution vs. the number of photons of a given event (equation 4.14) we can apply the model as outlined in 4.4 and calculate the shift from observed mean photons to real mean photons.

#### 4.6.2 Tritium S2 Correction

Figure 4.25 shows the application of smearing from equation 4.41 applied to the charge yield extracted from the uncorrected tritium data with the data. The mapping for converting the observed S2 to the real S2 is shown in the figure. To cal-

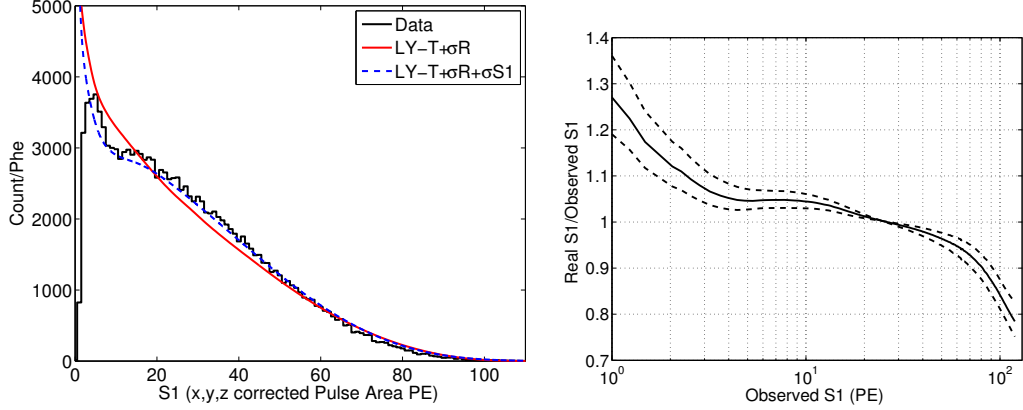


Figure 4.25: Left: In Black, tritium data. In red, the spectrum after applying measured recombination fluctuations. In dashed blue is after applying recombination and finite detector resolution of equation. Left: Mapping of the observed mean, with finite resolution, to the mean with infinite resolution for a tritium photon spectrum. Bottom Right: The ratio of the real mean to the observed mean vs. the observed mean for a tritium photon spectrum. Note the S1 threshold at about 3 Phe in S1.

culate the correction we start with the extracted light yield, apply the measured g<sup>2</sup>, convolve it with a tritium beta spectrum and add in our first approximation of recombination fluctuations measured in equation 4.23, given infinite detector resolution this is the spectrum the LUX detector would observe in S1 space. Knowing the dependance of detector resolution vs. the number of electrons of a given event (equation 4.14) we can apply the model as outlined in 4.4 and calculate the shift from observed mean photons to real mean photons.

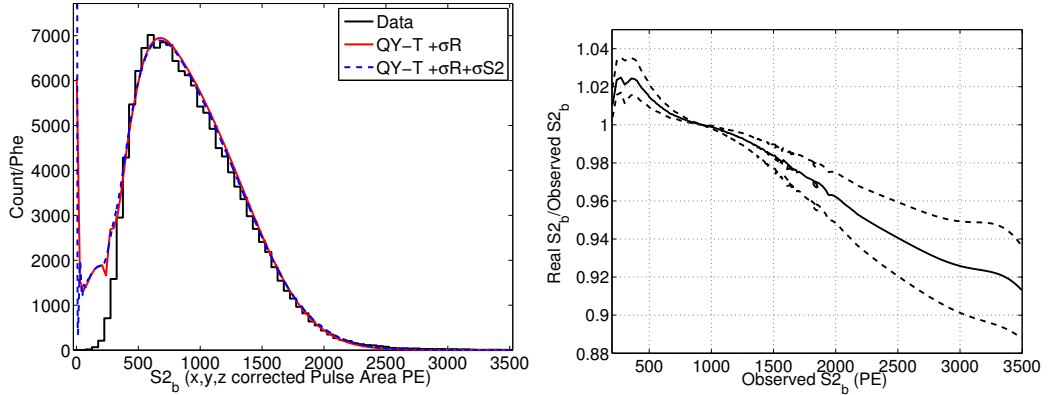


Figure 4.26: Left: In Black, tritium data. In red, the spectrum after applying measured recombination fluctuations. In dashed blue is after applying recombination and finite detector resolution of equation. Left: Mapping of the observed mean, with finite resolution, to the mean with infinite resolution for a tritium photon spectrum. Bottom Right: The ratio of the real mean to the observed mean vs. the observed mean for a tritium photon spectrum. Note the S2 threshold at about 400 Phe.

## 4.7 Thresholds

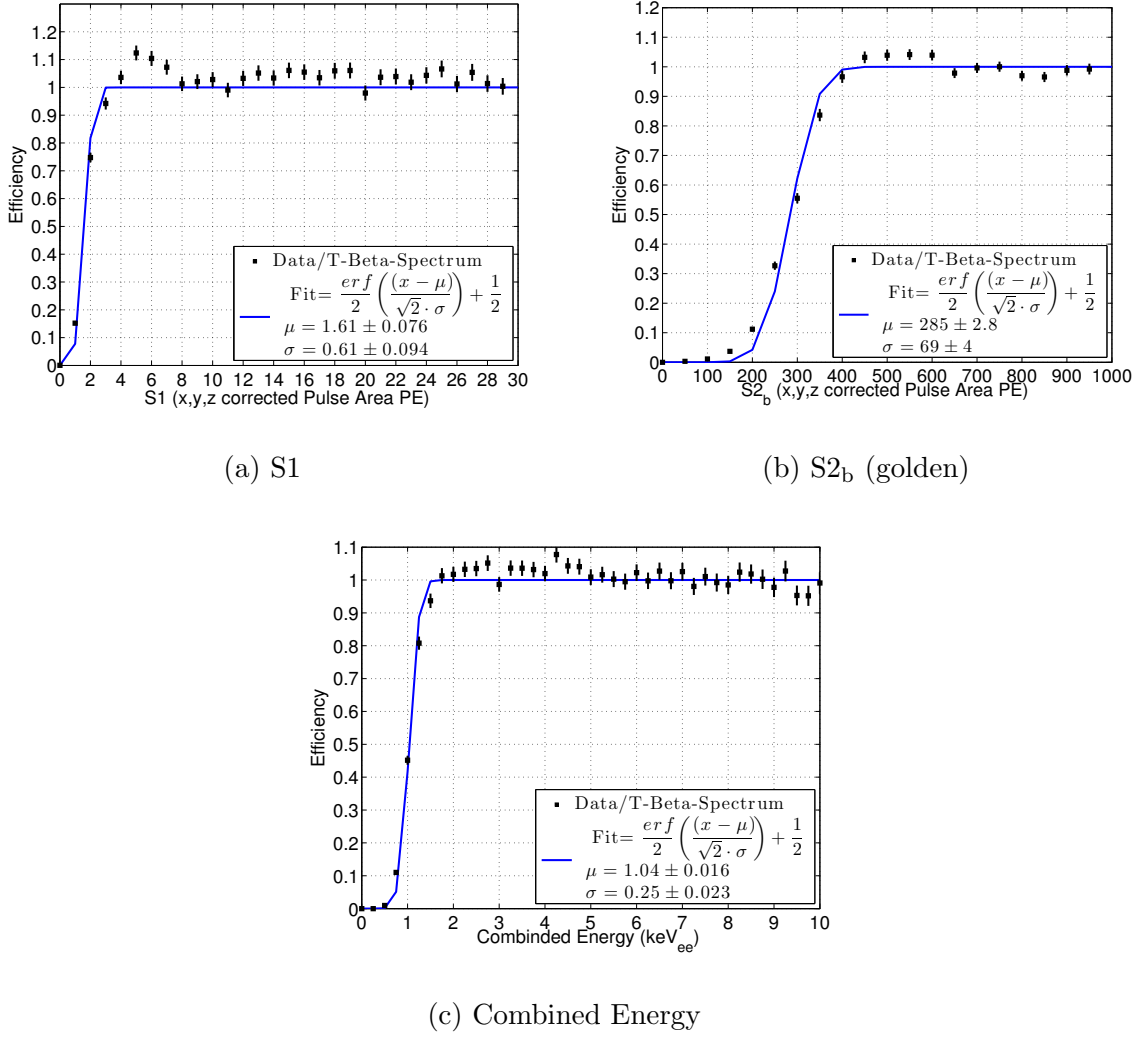


Figure 4.27: Threshold calculated from difference of simulated Tritium S1, S2 and energy spectra. a) S1 b) S2<sub>b</sub>, c) E .

## 4.8 Ionization and Scintillation Yield and Recombination After Correction

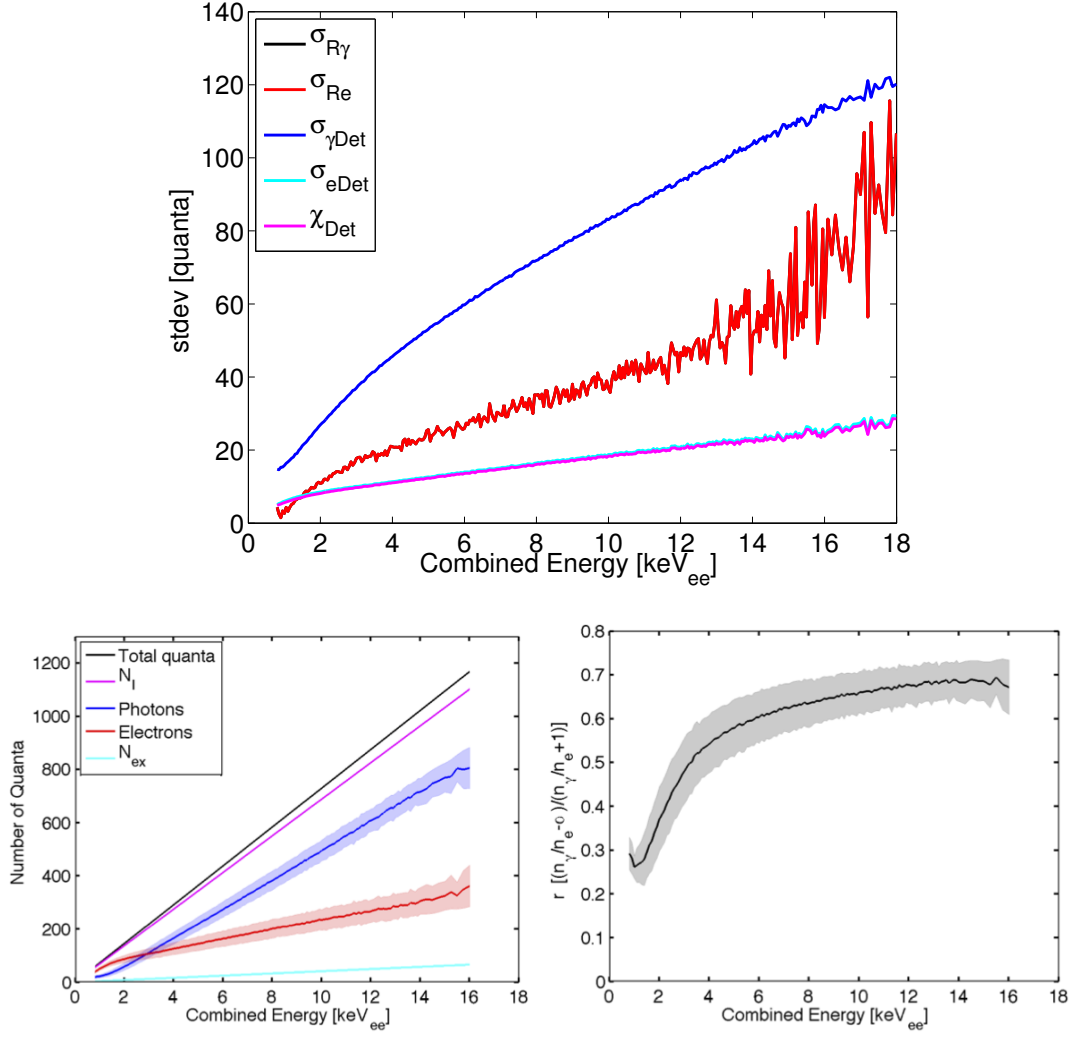


Figure 4.28: After spectral shape correction. Top: Extracted recombination fluctuation from the tritium data from fluctuations in photons and electrons (Black and Red receptively). Bottom right: mean number of quanta in photons, electrons, ions, exitons vs. energy [keV] for the tritium calibrations. Bottom left: Recombination fraction and the one sigma (shaded) vs. energy [keV].

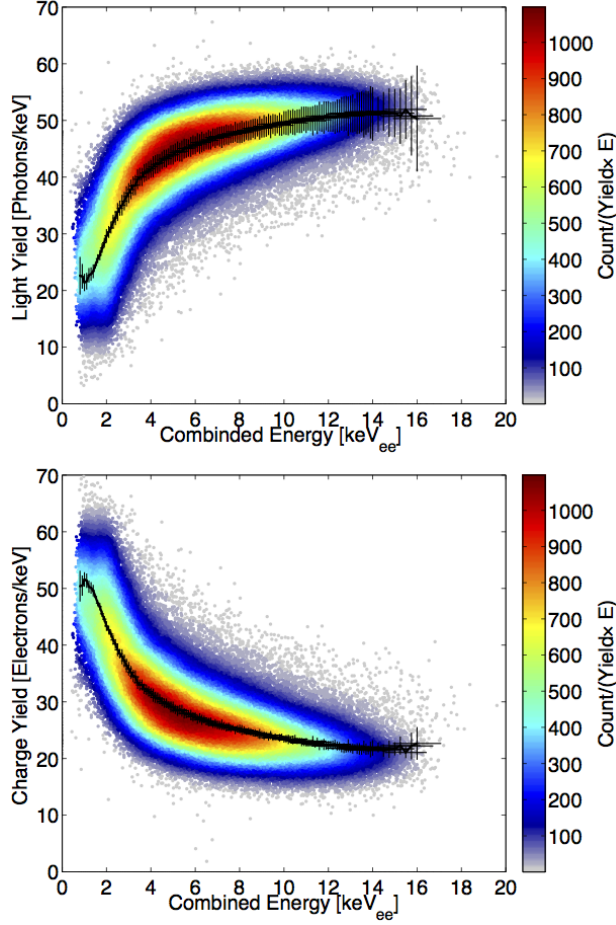


Figure 4.29: Extracting LY and QY from data corrected for spectral shape.

#### 4.9 The Standard Candle. Light Yield from $^{83m}\text{Kr}$

Quenching of scintillation yield vs. field has been typically defined relative to 32.1 keV decay of  $^{83m}\text{Kr}$  at zero field [63],[64].  $^{83m}\text{Kr}$  first emits a 32.1 [keV] gamma followed by a 9.4 [keV] with a half life of 154 [ns] between the two (refs). The combined signal (41.6 [keV]) is found by the pulse finder in the majority of cases, using the standard WIMP search pulse gap setting of 500 ns. However, the combined signal is not useful as a standard calibration since the light yield from the second 9.4 keV decay depends strongly on decay time separation. The second 9.4 keV decay

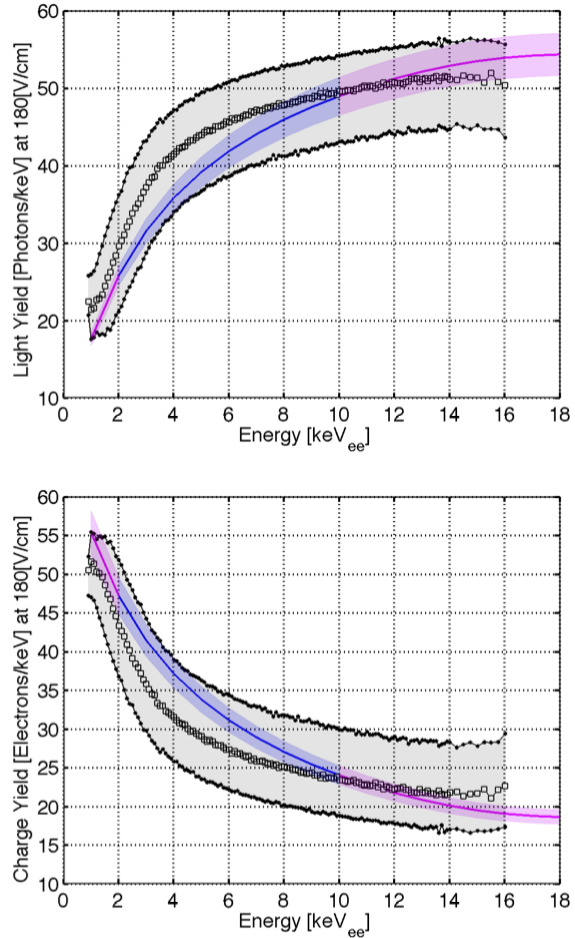


Figure 4.30: LY and QY from tritium data corrected for spectral shape along with the 1 sigma band of g1/g2. The blue and magenta curve are NEST extrapolation and interpolation, respectively.

is effected by the presence of exitons from the initial 32.1 [keV] decay. See figure [ show LUX result]

Fortunately, the first 32.1 keV appears to have no time dependance as it decays in ‘relaxed’ xenon without the presence of additional exitons [63]. For purposes of light yield normalization at zero field the 32.1 keV gamma serves as a good low energy standard candle for xenon detectors.

There were two data sets in late 2013 that contain  $^{83m}\text{Kr}$  decays at zero field. Since the S2 (charge) signal is unavailable the top-bottom asymmetry,  $\frac{\text{top-bottom}}{\text{top+bottom}}$ , is used to define the Z coordinate for position dependent corrections. The XY correction is subdominant to the Z dependent correction for light yield. Figure [] shows the linear mapping from top-bottom asymmetry to detector depth (Z). With the Z correction applied the average pulse area (Phe) normalized to the detector center (241.6 mm below the gate grid) is found to be  $267.4 \pm^{\text{stat}} 1.5 \pm^{\text{sys}} 5$ . See Figure 4.31.

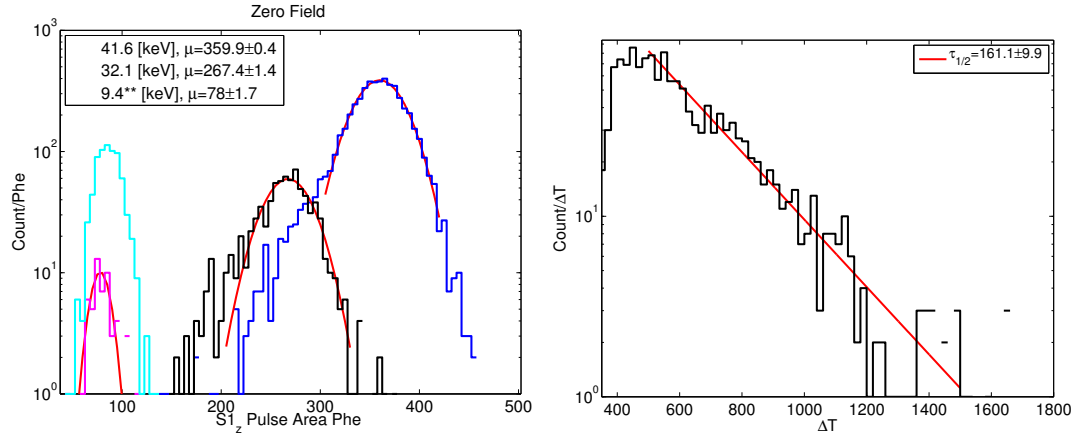


Figure 4.31: Left:  $^{83m}\text{Kr}$  peaks at zero field. \*\* The 9.4 keV peak is fit only for events with a decay time separation greater than 1000 [ns]. Right: shows the timing separation between the 32.1 and 9.4 [keV] decays plotted above.

### 4.9.1 Field dependence of light yield from the 32.1 keV gamma of

$^{83m}\text{Kr}$

Charge separation increases with drift field leading to less recombination for light production, causing scintillation yield to be quenched. See table 4.5 for a list of the measured scintillation of the 32.1 keV gamma from  $^{83m}\text{Kr}$ , also includes the NEST predictions.

Field [V/cm]	S1[Phe]	Photons[ $n_\gamma$ ]	Yield [ $n_\gamma/\text{keV}$ ]	NEST [ $n_\gamma/\text{keV}$ ]
0	$267.4 \pm 6.5$	$1980 \pm 40.7$	$61.7 \pm 1.27$	$64.2 \pm 2.6$
51	$246.7 \pm 1.2$	$1827.4 \pm 8.9$	$56.9 \pm 0.28$	$60.8 \pm 2.5$
105	$233.6 \pm 1.4$	$1730.4 \pm 10.4$	$53.9 \pm 0.32$	$58.3 \pm 2.3$
182	$212.3 \pm 1.3$	$1572.6 \pm 9.6$	$49.0 \pm 0.30$	$54.9 \pm 2.1$

Table 4.5: Field dependance of the light yield form the 32.1 keV decay of  $^{83m}\text{Kr}$ . The fields are calculated using a two dimensional model and not accounting potential charge accumulation on inner teflon panels.

## Bibliography

- [1] M. Weber and W. de Boer. Determination of the local dark matter density in our Galaxy. *AAP*, 509:A25, jan 2010. doi:10.1051/0004-6361/200913381.
- [2] Anse Slosar, et al. Measurement of Baryon Acoustic Oscillations in the Lyman-alpha Forest Fluctuations in BOSS Data Release 9. *JCAP*, 1304:026, 2013. doi:10.1088/1475-7516/2013/04/026.
- [3] J.D. Lewin and P.F. Smith. Review of mathematics, numerical factors, and corrections for dark matter experiments based on elastic nuclear recoil. *Astropart.Phys.*, 6:87–112, 1996. doi:10.1016/S0927-6505(96)00047-3.
- [4] Richard H. Helm. Inelastic and elastic scattering of 187-mev electrons from selected even-even nuclei. *Phys. Rev.*, 104:1466–1475, Dec 1956. doi:10.1103/PhysRev.104.1466.
- [5] D. S. Akerib, et al. Radiogenic and muon-induced backgrounds in the LUX dark matter detector. *Astroparticle Physics*, 62:33–46, March 2015. doi:10.1016/j.astropartphys.2014.07.009.
- [6] Scott Hertel. private communication, 2014.
- [7] M. Arenz and R. Vianden. 83mkr, a potentially powerful pac probe. *Hyperfine Interactions*, 222(1-3):73–76, 2013. ISSN 0304-3843. doi:10.1007/s10751-012-0723-3.
- [8] J. H. Oort. The force exerted by the stellar system in the direction perpendicular to the galactic plane and some related problems. *BAIN*, 6:249, August 1932.
- [9] F. Zwicky. On the Masses of Nebulae and of Clusters of Nebulae. *API*, 86:217, October 1937. doi:10.1086/143864.

- [10] K. G. Begeman, A. H. Broeils, and R. H. Sanders. Extended rotation curves of spiral galaxies: dark haloes and modified dynamics. *Monthly Notices of the Royal Astronomical Society*, 249(3):523–537, 1991. doi:10.1093/mnras/249.3.523.
- [11] Robert H. Brandenberger. Formation of structure in the universe. 1995.
- [12] Ryan Cooke, Max Pettini, Regina A. Jorgenson, Michael T. Murphy, and Charles C. Steidel. Precision measures of the primordial abundance of deuterium. 2013.
- [13] P.A.R. Ade et al. Planck 2013 results. XVI. Cosmological parameters. *Astrophys. Astrophys.*, 2014. doi:10.1051/0004-6361/201321591.
- [14] D. J. Fixsen. The Temperature of the Cosmic Microwave Background. *APJ*, 707:916–920, December 2009. doi:10.1088/0004-637X/707/2/916.
- [15] P.A.R. Ade et al. Planck 2013 results. I. Overview of products and scientific results. 2013. doi:10.1051/0004-6361/201321529.
- [16] Daniel J. Eisenstein, Hee-jong Seo, and 1 White, Martin J. On the Robustness of the Acoustic Scale in the Low-Redshift Clustering of Matter. *Astrophys.J.*, 664:660–674, 2007. doi:10.1086/518755.
- [17] W. J. Percival, et al. Baryon acoustic oscillations in the Sloan Digital Sky Survey Data Release 7 galaxy sample. *mnras*, 401:2148–2168, February 2010. doi:10.1111/j.1365-2966.2009.15812.x.
- [18] Maxim Markevitch. Chandra observation of the most interesting cluster in the universe. 2005.
- [19] Douglas Clowe, et al. A direct empirical proof of the existence of dark matter. *Astrophys.J.*, 648:L109–L113, 2006. doi:10.1086/508162.
- [20] Peter J. Kernan and Lawrence M. Krauss. Refined big bang nucleosynthesis constraints on Omega (baryon) and N (neutrino). *Phys.Rev.Lett.*, 72:3309–3312, 1994. doi:10.1103/PhysRevLett.72.3309.
- [21] Q.R. Ahmad et al. Direct evidence for neutrino flavor transformation from neutral current interactions in the Sudbury Neutrino Observatory. *Phys.Rev.Lett.*, 89:011301, 2002. doi:10.1103/PhysRevLett.89.011301.
- [22] George R. Blumenthal, S.M. Faber, Joel R. Primack, and Martin J. Rees. Formation of Galaxies and Large Scale Structure with Cold Dark Matter. *Nature*, 311:517–525, 1984. doi:10.1038/311517a0.
- [23] Masahiro Kawasaki and Kazunori Nakayama. Axions: Theory and Cosmological Role. *Ann.Rev.Nucl.Part.Sci.*, 63:69–95, 2013. doi:10.1146/annurev-nucl-102212-170536.

- [24] C.A. Baker, et al. An Improved experimental limit on the electric dipole moment of the neutron. *Phys.Rev.Lett.*, 97:131801, 2006. doi:10.1103/PhysRevLett.97.131801.
- [25] R. D. Peccei and Helen R. Quinn. CP. *Phys. Rev. Lett.*, 38:1440–1443, Jun 1977. doi:10.1103/PhysRevLett.38.1440.
- [26] R. D. Peccei and Helen R. Quinn. Constraints imposed by CP conservation in the presence of pseudoparticles. *Phys. Rev. D*, 16:1791–1797, Sep 1977. doi: 10.1103/PhysRevD.16.1791.
- [27] E. Arik et al. Probing eV-scale axions with CAST. *JCAP*, 0902:008, 2009. doi:10.1088/1475-7516/2009/02/008.
- [28] S. J. Asztalos, et al. SQUID-Based Microwave Cavity Search for Dark-Matter Axions. *Physical Review Letters*, 104(4):041301, January 2010. doi:10.1103/PhysRevLett.104.041301.
- [29] Gerard Jungman, Marc Kamionkowski, and Kim Griest. Supersymmetric dark matter. *Phys.Rept.*, 267:195–373, 1996. doi:10.1016/0370-1573(95)00058-5.
- [30] Andriy Kurylov and Marc Kamionkowski. Generalized analysis of weakly interacting massive particle searches. *Phys.Rev.*, D69:063503, 2004. doi: 10.1103/PhysRevD.69.063503.
- [31] S. Akerib, D. et al. First results from the lux dark matter experiment at the sanford underground research facility. *Phys. Rev. Lett.*, 112:091303, Mar 2014. doi:10.1103/PhysRevLett.112.091303.
- [32] E. Aprile, et al. Dark Matter Results from 225 Live Days of XENON100 Data. *Physical Review Letters*, 109(18):181301, November 2012. doi:10.1103/PhysRevLett.109.181301.
- [33] Mengjiao Xiao et al. First dark matter search results from the PandaX-I experiment. 2014.
- [34] K. Abe, et al. Light WIMP search in XMASS. *Physics Letters B*, 719:78–82, February 2013. doi:10.1016/j.physletb.2013.01.001.
- [35] A. Wright. The DarkSide Program at LNGS. In S. Giani and et al., editors, *Astroparticle, Particle, Space Physics and Detectors For Physics Applications - Proceedings of the 13th ICATPP Conference. Edited by Giani Simone et al. Published by World Scientific Publishing Co. Pte. Ltd., 2012. ISBN #9789814405072, pp. 414-420, pages 414–420*. August 2012. doi: 10.1142/9789814405072\_0061.
- [36] A. Hime. The MiniCLEAN Dark Matter Experiment. *ArXiv e-prints*, October 2011.

- [37] CDMS II Collaboration, et al. Dark Matter Search Results from the CDMS II Experiment. *Science*, 327:1619–, March 2010. doi:10.1126/science.1186112.
- [38] C. E. Aalseth, et al. CoGeNT: A search for low-mass dark matter using p-type point contact germanium detectors. *prd*, 88(1):012002, July 2013. doi: 10.1103/PhysRevD.88.012002.
- [39] S. Archambault et al. Constraints on Low-Mass WIMP Interactions on  $^{19}F$  from PICASSO. *Phys.Lett.*, B711:153–161, 2012. doi:10.1016/j.physletb.2012.03.078.
- [40] E. Behnke, et al. First dark matter search results from a 4-kg  $\text{CF}_3\text{I}$  bubble chamber operated in a deep underground site. *prd*, 86(5):052001, September 2012. doi:10.1103/PhysRevD.86.052001.
- [41] E. Aprile and T. Doke. Liquid xenon detectors for particle physics and astrophysics. *Rev. Mod. Phys.*, 82:2053–2097, Jul 2010. doi:10.1103/RevModPhys.82.2053.
- [42] Attila Dobi, et al. Detection of krypton in xenon for dark matter applications. *Nucl.Instrum.Meth.*, A665:1–6, 2011. doi:10.1016/j.nima.2011.11.043.
- [43] A.I. Bolozdynya, P.P. Brusov, T. Shutt, C.E. Dahl, and J. Kwong. A chromatographic system for removal of radioactive  $^{85}\text{Kr}$  from xenon. *Nuclear Instruments and Methods in Physics Research Section A: Accelerators, Spectrometers, Detectors and Associated Equipment*, 579(1):50 – 53, 2007. ISSN 0168-9002. doi: DOI:10.1016/j.nima.2007.04.011. Proceedings of the 11th Symposium on Radiation Measurements and Applications.
- [44] K. Abe, et al. Distillation of liquid xenon to remove krypton. *Astroparticle Physics*, 31(4):290 – 296, 2009. ISSN 0927-6505. doi:DOI:10.1016/j.astropartphys.2009.02.006.
- [45] John R de Laeter, et al. Atomic weights of the elements. review 2000 (iupac technical report). *Pure and Applied Chemistry*, 75(6):683–800, 2003.
- [46] C. E. Dahl. *Ph.D. Thesis*. Ph.D. thesis, Princeton University, 2009.
- [47] M. Miyajima, et al. Average energy expended per ion pair in liquid argon. *Phys. Rev. A*, 9:1438–1443, Mar 1974. doi:10.1103/PhysRevA.9.1438.
- [48] T. Takahashi, et al. Average energy expended per ion pair in liquid xenon. *Phys. Rev. A*, 12:1771–1775, Nov 1975. doi:10.1103/PhysRevA.12.1771.
- [49] T. Doke and K. Masuda. Present status of liquid rare gas scintillation detectors and their new application to gamma-ray calorimeters. *Nucl.Instrum.Meth.*, A420:62–80, 1999. doi:10.1016/S0168-9002(98)00933-4.
- [50] S Kubota, M Hishida, and J Raun. Evidence for a triplet state of the self-trapped exciton states in liquid argon, krypton and xenon. *Journal of Physics C: Solid State Physics*, 11(12):2645, 1978.

- [51] Akira Hitachi, et al. Effect of ionization density on the time dependence of luminescence from liquid argon and xenon. *Phys.Rev.*, B27:5279–5285, 1983. doi:10.1103/PhysRevB.27.5279.
- [52] David P. Lide, editor. *CRC Handbook of Chemistry and Physics*. CRC PRESS, 81 edition, 2000.
- [53] T. Doke, A. Hitachi, S. Kubota, A. Nakamoto, and T. Takahashi. Estimation of Fano factors in liquid argon, krypton, xenon and xenon-doped liquid argon. *Nucl.Instrum.Meth.*, 134:353–357, 1976. doi:10.1016/0029-554X(76)90292-5.
- [54] Jens Lindhard, V Nielsen, M Scharff, and PV Thomsen. *Integral equations governing radiation effects*. Munksgaard i komm., 1963.
- [55] M. Szydagis, et al. NEST: A Comprehensive Model for Scintillation Yield in Liquid Xenon. *ArXiv e-prints*, June 2011.
- [56] Matthew Szydagis, Adalyn Fyhrie, Daniel Thorngren, and Mani Tripathi. Enhancement of NEST Capabilities for Simulating Low-Energy Recoils in Liquid Xenon. *JINST*, 8:C10003, 2013. doi:10.1088/1748-0221/8/10/C10003.
- [57] W. . Chen, et al. Measurement of the transverse diffusion coefficient of charge in liquid xenon. *ArXiv e-prints*, September 2011.
- [58] R. Agnese et al. Search for Low-Mass Weakly Interacting Massive Particles Using Voltage-Assisted Calorimetric Ionization Detection in the SuperCDMS Experiment. *Phys.Rev.Lett.*, 112(4):041302, 2014. doi:10.1103/PhysRevLett.112.041302.
- [59] G. Angloher, et al. Results from 730 kgdays of the cresst-ii dark matter search. *The European Physical Journal C*, 72(4):1971, 2012. ISSN 1434-6044. doi:10.1140/epjc/s10052-012-1971-8.
- [60] R. Bernabei, et al. Final model independent result of DAMA/LIBRA-phase1. *European Physical Journal C*, 73:2648, December 2013. doi:10.1140/epjc/s10052-013-2648-7.
- [61] V. Eckardt, et al. Calibration of the STAR forward time projection chamber with krypton-83m. 2001.
- [62] L.W. Kastens, S. Bedikian, S.B. Cahn, A. Manzur, and D.N. McKinsey. A 83Krm Source for Use in Low-background Liquid Xenon Time Projection Chambers. *JINST*, 5:P05006, 2010. doi:10.1088/1748-0221/5/05/P05006.
- [63] E. Aprile, et al. Measurement of the scintillation yield of low-energy electrons in liquid xenon. *Phys. Rev. D*, 86:112004, Dec 2012. doi:10.1103/PhysRevD.86.112004.
- [64] L. Baudis, et al. Response of liquid xenon to compton electrons down to 1.5 kev. *Phys. Rev. D*, 87:115015, Jun 2013. doi:10.1103/PhysRevD.87.115015.